Large Eddy Simulation of Turbulent Reacting Flows With Radiative Heat Transfer

Dem Fachbereich Maschinenbau
an der Technischen Universität Darmstadt
zur
Erlangung des Grades eines Doktor-Ingenieurs (Dr.-Ing.)
genehmigte

D i s s e r t a t i o n

vorgelegt von

Flavia Cavalcanti Miranda, M. Sc.

aus Piracanjuba, Brasilien

Berichterstatter:	Prof. Dr.-Ing. Johannes Janicka
Mitberichterstatter:	Prof. Pedro J. Coelho
Tag der Einreichung:	10.04.2018
Tag der mündlichen Prüfung:	26.06.2018

Darmstadt 2018
D17

Cavalcanti Miranda, Flavia: Large Eddy Simulation of Turbulent Reacting Flows With Radiative Heat Transfer,
Darmstadt,Technische Universität Darmstadt,
Jahr der Veröffentlichung der Dissertation auf TUprints: 2019
Tag der mündlichen Prüfung: 26.06.2018

Erklärung

Hiermit erkläre ich, dass ich die vorliegende Arbeit, abgesehen von den in ihr ausdrücklich genannten Hilfen, selbständig verfasst habe.

Datum, Unterschrift

Acknowledgements

I would like to express my sincere gratitude to my advisor Prof. Dr.-Ing. Johannes Janicka for the opportunity of being part of his research group and for his guidance, support and encouragement. My work and professional development enriched a lot with his vast experience, knowledge and motivation. I would like to extend my gratitude to Prof. Pedro Coelho for our discussions, his essential contribution and effort to report on my work.

I would like to acknowledge the *Deutsche Forschnungsgemeinschaft* (DFG) in the framework of the Excellence Initiative, Darmstadt Graduate School of Excellence Energy Science and Engineering (GSC1070) for founding this research work.

I also would like to thank my colleagues at EKT and RSM for providing a nice working environment. My special thanks to Guido, who was my last hope when the code was not working. I further would like to thank Fernando, Samim and Robert for the productive scientific discussions we had. Many thanks to Wibke, Pedro, Nikil, Sebastian, Adam, Louis and Alija for the patient proofreading of this work and to my office mates Jhon, Benny, Tao and Anna for the pleasant atmosphere provided.

I would further like to thank the ones that indirectly contributed to this work by helping me to have a better work-life-balance: Doudou, Gabriela and VCE friends. Besides that, I would like to thank my parents and my sister for the care, understanding and unconditional support. Their presence is more than important, it is fundamental, in all the steps of my life. I am also very grateful to the persons that I consider my family in Germany: David and Arne for the fellowship, support, patience and help.

Damstadt, April 2018

Flavia Cavalcanti Miranda

Contents

1 Introduction **1**
- 1.1 State of Research . . . 3
- 1.2 Objectives . . . 7
- 1.3 Thesis Outline . . . 8

2 Mathematical Description of Turbulent Flows **11**
- 2.1 Governing Equations . . . 11
  - 2.1.1 Conservation of Mass and Momentum . . . 12
  - 2.1.2 Species Transport . . . 13
  - 2.1.3 Conservation of Energy . . . 14
  - 2.1.4 The Equation of State . . . 16
  - 2.1.5 Summary of the Employed Equations . . . 16
- 2.2 Turbulence . . . 17
  - 2.2.1 Turbulent Modeling . . . 19
  - 2.2.2 Large Eddy Simulation . . . 20
- 2.3 Summary . . . 23

3 Fundamentals of Combustion and Modeling Reacting Flows **25**
- 3.1 Fundamentals of Chemical Reaction . . . 25
  - 3.1.1 Chemical Reaction Kinetics . . . 26
- 3.2 Flame Modes . . . 27
  - 3.2.1 Nonpremixed Flames . . . 28
  - 3.2.2 Premixed Flames . . . 29
- 3.3 Turbulence-Chemistry Interaction . . . 30
- 3.4 Combustion Modeling . . . 32
  - 3.4.1 Chemistry Reduction Using Flamelet Generated Manifolds . . . 32
  - 3.4.2 FGM Coupling with LES . . . 34
- 3.5 Stochastic Field Method for Modeling Turbulent Combustion . . . 35
  - 3.5.1 Filtered Probability Density Function . . . 35
  - 3.5.2 Eulerian Monte Carlo Stochastic Field Method . . . 36
  - 3.5.3 Summary of the Solved Equations . . . 37
- 3.6 Summary . . . 38

4 Numerical Methods **39**
- 4.1 General Solution Procedure . . . 39
  - 4.1.1 Domain Discretization . . . 40
    - 4.1.1.1 Spatial Discretization of the Transport Equations . . . 40

4.1.2 Convective Fluxes . . . 42
4.1.3 Diffusive Fluxes . . . 44
4.1.4 Temporal Discretization . . . 44
4.1.5 Pressure-velocity Coupling . . . 45
4.1.6 Boundary Conditions . . . 47
4.2 Numerical Method for the Eulerian Stochastic Field Method . . . 48
4.3 Overall Solution Procedure for Simulation without Radiation . . . 48
4.4 Parallelization . . . 49
4.5 Summary . . . 49

5 Thermal Radiation and Turbulence-Radiation Interactions 51
5.1 Fundamentals of Thermal Radiation . . . 51
5.1.1 Blackbody . . . 52
5.1.2 Solid Angles . . . 53
5.1.3 Spectral Radiative Intensity . . . 54
5.2 Radiative Transfer Equation in Participating Media . . . 54
5.2.1 Boundary Conditions for RTE . . . 55
5.2.2 Optical Thickness . . . 55
5.3 Radiative Heat Flux and Divergence of the Radiative Heat Flux . . . 55
5.4 Spectral Treatment of Radiation . . . 56
5.4.1 Weighted Sum of Gray Gases (WSGG) Model . . . 57
5.4.1.1 Nongray WSGG Model . . . 58
5.4.1.2 Gray WSGG Model . . . 61
5.5 Numerical Methods for the Radiative Transfer Equation . . . 62
5.5.1 Finite Volume Method for the RTE . . . 63
5.5.2 Finite Volume Method for the Divergence of the Radiative Heat Flux 66
5.5.3 Shortcomings of the Employed Methods for Solving the RTE . . . 67
5.6 Overall Solution Procedure for Simulation with Radiation . . . 67
5.7 Turbulence-Radiation Interactions (TRI) . . . 68
5.8 Summary . . . 71

6 Verification of the Radiation Solver 73
6.1 Verification of the Solver for the Radiative Transfer Equation . . . 73
6.1.1 2D Enclosure with a Pure Absorbing-Emitting Medium . . . 74
6.1.2 2D Enclosure with a Pure Scattering Medium . . . 75
6.1.3 Cubical Enclosure . . . 76
6.1.4 Hexahedral Enclosure . . . 77
6.1.5 3D Annular Sector . . . 77
6.1.6 L-shaped Enclosure . . . 78
6.1.7 Cylindrical Enclosure . . . 79
6.1.8 Verification of the implemented WSGG Models . . . 80
6.1.8.1 Rectangular Box . . . 81
6.1.8.2 Cylindrical Combustion Chamber . . . 82
6.2 Summary . . . 84

7 Preliminary Investigation: Validation of the Used Models 87

7.1 Sandia Flame D . . . 87
7.1.1 Description of the Configuration . . . 87
7.1.2 Numerical Setup . . . 88
7.1.3 Results . . . 91
7.1.4 Summary . . . 95
7.2 Bluff-Body Stabilized Nonpremixed Flame . . . 96
7.2.1 Description of the Configuration . . . 96
7.2.2 Numerical Setup . . . 97
7.2.3 Results . . . 98
7.2.4 Summary . . . 100

8 Results **103**
8.1 Sandia Flame D . . . 104
8.1.1 Noncoupled Simulations . . . 105
8.1.2 Coupled Simulations . . . 109
8.1.3 Summary . . . 109
8.2 Bluff-Body Stabilized Nonpremixed Flame . . . 111
8.2.1 Summary . . . 112

9 Summary and Outlook **115**

A Supplemental results **119**

List of Figures

2.1 Kinetic energy spectrum for a turbulent flow. 18
2.2 Kinetic energy spectrum for turbulent flows showing the difference among the three approaches: DNS, RANS and LES. The explicitly resolved region is illustrated in blue while the modeled part in red. 20

3.1 (a) Basic representation of a diffusion flame and (b) species distribution of a one-dimensional nonpremixed methane-air flame with $a = 100\,\mathrm{s}^{-1}$ and $T_u = 300\,\mathrm{K}$. 28
3.2 (a) Basic representation of a premixed flame and (b) species distribution of a one-dimensional premixed methane-air flame with $\phi = 1$ and $T_u = 300\,\mathrm{K}$. 30
3.3 Representation of a premixed flame in (a) laminar and (b) turbulent regime. 30
3.4 Classical turbulent combustion regime diagram (Peters [107]). 31
3.5 Visualization of the applied three-dimensional table. (a) Complete representation with a cut for $\phi = 1$ and overlapped CO_2 source term $\dot{\omega}_{CO_2}$. (b) Slice for $\phi = 1$ with three indicated areas α) adiabatic, β) burner stabilized and γ) extrapolated. 33

4.1 Example of a block structured grid including a local refinement. Figure adapted from Künne [78]. 40
4.2 (a) An arbitrary control volume P showing the global $(\mathrm{x}_1, \mathrm{x}_2, \mathrm{x}_3)$ and the local (ξ_1, ξ_2, ξ_3) coordinate systems, (b) two dimensional view for $\xi_3 = 0$ of this control volume and its neighbors. 41
4.3 Example of a control volume illustrating the considered face e and its neighbors for calculating the convection fluxes with the TVD scheme. 43

5.1 Spectrum of electromagnetic radiation (wavelength in vacuum). 52
5.2 Scheme of a surface radiating and its solid angle. 53
5.3 Spectral absorption coefficient for CO_2 4.3 μm band at $T = 1000\,\mathrm{K}$, $p = 1\,\mathrm{bar}$ and $p_{CO_2} = 0.1\,\mathrm{bar}$ (from HITRAN database 2012). 56
5.4 Representation of the pressure absorption coefficient with the WSGG model using I gray gases. Figure adapted from Dorigon et al. [41]. 57
5.5 Representation of the discretized solid angles (a) with constant angle distribution and direction vectors and (b) with the angular distribution proposed in the method FT_n FVM. 64
5.6 Illustration of the Ray effect. 67

6.1 Geometry for the 2D box-shaped cases. 74

6.2 Nondimensional heat transfer on the wall for a pure absorbing and emitting medium. . . . 75
6.3 Nondimensional heat transfer on the bottom wall for a pure scattering medium. . . . 75
6.4 Nondimensional heat transfer on the centerline of the bottom wall ($Y = 0$, $Z = 0.5L$) for the grid 50 x 50 x 50 and the nondimensional absorption coefficient $\kappa^* = 10$. . . . 76
6.5 (a) Geometry and (b) spatial grid of the plane xy for the hexahedral enclosure (Baek et al. [13]). . . . 77
6.6 Radiative heat flux for the hexahedral enclosure on the wall along the line A-A for three different absorption coefficients. . . . 78
6.7 Geometry of the annular sector. . . . 78
6.8 Radial heat flux on the outer wall along (a) $\mu = 30^o$ (line 1) and (b) z = 0.5 m (line 2) for the annular sector. . . . 79
6.9 L-shaped geometry enclosure. . . . 79
6.10 Radiative heat flux for the L-shaped enclosure along the A-A line for four different absorption coefficient. . . . 80
6.11 Radial section of the grid used for the cylindrical enclosure. . . . 80
6.12 Radiative source term along the central axis of the cylinder for (a) $\kappa = 0.1\,\mathrm{m}^{-1}$, (b) $\kappa = 1\,\mathrm{m}^{-1}$ and (c) $\kappa = 10\,\mathrm{m}^{-1}$. . . . 81
6.13 Temperature distribution for the rectangular box. . . . 82
6.14 Radiative source term along line 1 and wall heat flow along lines 2 and 3 (see Fig. 6.13). Top: air combustion and bottom: oxyfuel combustion. No benchmark data is available for line 3 in the air combustion case. . . . 83
6.15 Geometry for the cylindrical combustion chamber test. . . . 83
6.16 (a) Temperature field (b) H_2O and (c) CO_2 mole fraction distributions for the cylindrical combustion chamber case. . . . 85
6.17 Radiative source term for the cylindrical combustion chamber, (a) axial profile at chamber centerline, (b) radial profile at axial position $z = 1\,\mathrm{m}$ and (c) radial profile at axial position $z = 1.5\,\mathrm{m}$. . . . 86

7.1 Schematic diagram of the inlet configuration for the simulations of the flame D. . . . 88
7.2 Axial positions of the experimental measured lines for the flame D. . . . 88
7.3 Cross section of the coarse grid for the flame D simulations. . . . 89
7.4 Cross section of the fine grid for the flame D simulations. . . . 89
7.5 Dimensions of the computational domain for the (a) coarse and (b) fine grid. 90
7.6 Profiles of the mean velocity fields and variance at the axial position $x/D = 0.14$ for the flame D. . . . 90
7.7 Profiles of the mean axial velocity component and its variance at different axial positions for the flame D. . . . 92
7.8 Profiles of the mean radial velocity component and its variance at different axial positions for the flame D. . . . 92
7.9 Radial profiles for Temperature T at different axial positions for the flame D. . . . 93

7.10 Radial profiles for CO_2 mass fraction Y_{CO_2} at different axial positions for the flame D. 93
7.11 Mean and rms values of the mixture fraction Z along the centerline for the flame D. 93
7.12 Contours of the subgrid-scale variance Z^2_{sgs} by using the ESF method (on the left) and using the model proposed by Branley and Jones (on the right) for the simulation of the flame D using the coarse grid and Smagorinsky model. 94
7.13 Contours of the mean temperature. The red dashed line shows the stoichiometric value for the mixture fraction of $Z_{st} \approx 0.055$ for the simulation of the flame D using the coarse grid and Smagorinsky model. 95
7.14 Schematic configuration of the bluff-body burner. Figure adapted from [1]. 97
7.15 Axial positions of the experimental measured profiles for the bluff-body. . . 97
7.16 Cross section of the grid for the bluff-body case with the dimensions of the computational domain. 98
7.17 Profiles of the mean axial velocity component and its variance at different axial positions for the bluff-body flame. 99
7.18 Profiles of the mean radial velocity component and its variance at different axial positions for the bluff-body flame. 99
7.19 Radial profiles for the mixture fraction at different axial positions for the bluff-body flame. 100
7.20 Radial profiles for the Temperature T at different axial positions for the bluff-body flame. 100
7.21 Radial profiles for CO_2 mass fraction Y_{CO_2} at different axial positions for the bluff-body flame. 101
7.22 Contours of the subgrid-scale variance Z^2_{sgs} by using the ESF method (on the left) and with the model proposed by Branley and Jones (on the right) for the bluff-body configuration. 102

8.1 Temperature profiles along the jet axial center line for the flame D (continuous lines) and scaled flame (dashed lines). 105
8.2 Mean distributions of (a) CO_2 mole fraction, (b) H_2O mole fraction, (c) temperature and (d) radiative heat source term for the flame D calculated with the frozen fields. 106
8.3 Mean radiative heat source profiles for the scaled flame D with different TRI treatments calculated with the frozen fields. 106
8.4 Mean radiative heat source profiles for the scaled flame D showing the absorption and emission contributions calculated with the frozen fields. . . 106
8.5 (a) Mean emission radiative term calculated with the frozen fields of the scaled flame D for methods 1 (dashed lines) and 3 (continuous lines). (b) Quantification of the emission term on TRI by employing Eq. (8.2). 107
8.6 (a) Mean blackbody intensity calculated with the frozen fields of the scaled flame D for methods 1 (dashed lines) and 3 (continuous lines). (b) Quantification of the blackbody intensity self-correlation by employing Eq. (8.3). 108
8.7 Mean radiative heat source profiles calculated with the frozen fields of the flame D for two different angular discretizations. 108

8.8 (a) Mean emission term for the coupled simulation of the scaled flame for methods 1 (dashed lines) and 3 (continuous lines). (b) Quantification of the emission term on TRI by employing Eq. (8.2). 109
8.9 Top: mean temperature profiles for the coupled simulation of the scaled flame. Bottom: absolute difference among the employed methods. 110
8.10 Mean distributions of (a) CO_2 mole fraction, (b) H_2O mole fraction, (c) temperature and (d) radiative heat source term for the bluff-body flame calculated with the frozen fields. 112
8.11 Mean radiative heat source profiles for the scaled bluff-body flame with two different TRI treatments calculated with the frozen fields. 112
8.12 (a) Mean emission radiative term calculated with the frozen fields of the scaled bluff-body flame for methods 1 (dashed lines) and 3 (continuous lines). (b) Quantification of the emission term on TRI by employing Eq. (8.2). 113
8.13 (a) Mean blackbody intensity calculated with the frozen fields of the scaled bluff-body flame for methods 1 (dashed lines) and 3 (continuous lines). (b) Quantification of the blackbody intensity self-correlation by employing Eq. (8.3). 113

A.1 Mean radiative heat source profiles for the flame D with different TRI treatments calculated with the frozen fields. 119
A.2 Mean radiative heat source profiles for the flame D showing the absorption and emission contributions calculated with the frozen fields. 119
A.3 Mean emission term calculated with the frozen fields of the flame D for methods 1 (dashed lines) and 3 (continuous lines). (b) Quantification of the emission term on TRI by employing Eq. (8.2) 120
A.4 Mean blackbody intensity calculated with the frozen fields of the flame D for methods 1 (dashed lines) and 3 (continuous lines). (b) Quantification of the blackbody intensity self-correlation by employing Eq. (8.3). 120
A.5 Mean radiative heat source profiles for the coupled simulation of the flame D with different TRI treatments. 120
A.6 Mean emission term for the coupled simulation of the flame D for methods 1 (dashed lines) and 3 (continuous lines). (b) Quantification of the emission term on TRI by employing Eq. (8.2). 121
A.7 Top: mean temperature profiles for the coupled simulation of the flame D. Bottom: difference among the employed methods. 121
A.8 Mean radiative heat source profiles for the coupled simulation of the scaled flame D with different TRI treatments. 122
A.9 Mean radiative heat source profiles for the bluff-body flame with two different TRI treatments calculated with the frozen fields. 122
A.10 Mean emission radiative term calculated with the frozen fields of the bluff-body flame for methods 1 (dashed lines) and 3 (continuous lines). (b) Quantification of the emission term on TRI by employing Eq. (8.2). 122

A.11 Mean blackbody intensity calculated with the frozen fields of the bluff-body flame for methods 1 (dashed lines) and 3 (continuous lines). (b) Quantification of the blackbody intensity self-correlation by employing Eq. (8.3). 123

List of Tables

5.1 WSGG model coefficients for $p_w/p_c = 2$ (Dorigon et al. [41]). 59
5.2 WSGG model coefficients (Bordbar et al. [16]). 60
5.3 WSGG model coefficients (Johansson et al. [61]). 61

6.1 Error (%) for the cubical enclosure for three different grids and three different absorption coefficients ($\kappa^* = \kappa L$). 77
6.2 Coefficients for the temperature, Eq. (6.6), and chemical species distributions, Eqs. (6.7) and (6.8), as given in Centeno et al. [20] 84

8.1 Methods used for approximating the filtered emission radiative source term. 104

Nomenclature

Variables that are exclusively used locally are not included in the nomenclature.

Upper case Latin letters		**Units**
$\mathcal{C}$	Courant number	–
D	Diffusion number	–
C_Ω	Micro-mixing constant	–
C_s	Smagorinsky constant	–
$\mathcal{D}$	Diffusion coefficient	m^2/s
E	Spectrum of the turbulent kinetic energy	$\mathrm{m}^3/\mathrm{s}^2$
$E_{b\nu}$	Spectral black emissive power distribution	$\mathrm{W}/(\mathrm{m}^3 \cdot \mathrm{sr})$
E_b	Total emissive power of a blackbody	$\mathrm{W}/(\mathrm{m}^2 \cdot \mathrm{sr})$
$E_{m,j}$	Activation energy for direction m and reaction j	$(\mathrm{kgm}^2)/(\mathrm{s}^2\mathrm{kmol})$
$\mathcal{F}$	Joint probability density function	–
$\mathcal{G}$	Spatial filtering operator	$1/\mathrm{m}$
$\mathcal{L}$	Characteristic length scale	m
I_ν	Spectral radiative intensity	$\mathrm{W}/(\mathrm{m}^3 \cdot \mathrm{sr})$
I_b	Total blackbody intensity	$\mathrm{W}/(\mathrm{m}^2 \cdot \mathrm{sr})$
$I_{b\nu}$	Spectral blackbody intensity	$\mathrm{W}/(\mathrm{m}^3 \cdot \mathrm{sr})$
$\mathcal{I}$	Number of gray gases	–
I	Radiative intensity	$\mathrm{W}/(\mathrm{m}^2 \cdot \mathrm{sr})$
$K_{m,j}$	Reaction rate of the direction m and reaction j	$\mathrm{kmol}/(\mathrm{m}^3\mathrm{s})$
$\mathcal{M}$	Molar mass	kg/mol
N	Number of stochastic fields	–
N_s	Number of species k	–
$\mathcal{P}$	Probability density function	–
$\dot{\mathcal{Q}}$	External source or sink of enthalpy	$\mathrm{J}/(\mathrm{m}^3\mathrm{s})$
$\mathcal{Q}_j$	Total reaction rate of the reaction j	$\mathrm{kmol}/(\mathrm{m}^3\mathrm{s})$
$\mathcal{Q}$	General source term	–
$\mathcal{R}$	Ideal gas constant	J/(mol K)
S_{ij}	Strain rate	$1/\mathrm{s}$
S_r	Radiative source term	$\mathrm{J}/(\mathrm{m}^3\mathrm{s})$
T	Temperature	K

$\mathcal{U}$	Characteristic velocity	m/s
$V_{k,i}$	Diffusion velocity of the species k in the direction i	m/s
$[X_k]$	Mole concentration of the species k	kmol/kg
X	Mole fraction	–
$\mathcal{X}_k$	Symbol for the species k	–
Y	Mass fraction	–
Y_F	Mass fraction of fuel	–
Y_O	Mass fraction of oxidizer	–
$Y_\mathrm{n,pv}$	Normalized progress variable	–
Y_pv	Progress variable	–
Z	Mixture fraction	–

Lower case Latin letters		**Units**
$\mathbf{q}_{\mathrm{r}\nu}$	Spectral radiative heat flux	$\mathrm{W/m^3}$
$\mathbf{q}_\mathrm{r}$	Radiative heat flux	$\mathrm{W/m^2}$
b_k	Weights for species k	–
c_0	Speed of light in vacuum	m/s
c_p	Specific heat capacity at constant pressure	J/kg K
$f_{k,i}$	Volume force acting on the species k in the direction i	$\mathrm{m/s^2}$
f_{rad}	Frequency in which the radiative source term is updated	$\mathrm{s^{-1}}$
g	Acceleration of Gravity	$\mathrm{m/s^2}$
h	Specific enthalpy	J/kg
h_p	Planck's constant	Js
l	Length scale	m
l_d	Kolmogorov dissipative scale	m
l_t	Integral length scale	m
m	Mass	kg
n	Number of polar angle division	–
p	Pressure	$\mathrm{kg/(s^2m)}$
p_a	Partial pressure of the species a	$\mathrm{kg/(s^2m)}$
q_i	Energy flux in the direction i	$\mathrm{J/(m^2s)}$
s_L	Laminar flame speed	m/s
s_T	Turbulent flame speed	m/s
t	Time	s
u'	Velocity fluctuation	m/s
u_i	Velocity in the direction i	m/s
x_i	Cartesian coordinate in the direction i	m

Upper case Greek letters		**Units**
Δt	Time interval	s
Δ	Grid cell length	m
Ω	Solid angle	sr

Lower case Greek letters		**Units**
δ	Dirac delta function	–
δ_f	Flame thickness	m
δ_{ij}	Kronecker-symbol	–
ϵ	Dissipation's rate of the turbulent kinetic energy	m^2/s^3
η	Refractive index	–
κ_ν	Absorption coefficient	1/m
κ_b	Boltzmann's constant	J/K
κ_p	Partial absorption coefficient	$1/(m \cdot atm)$
λ	Wavelength	m
λ_T	Thermal conductivity	W/(mK)
μ	Dynamic viscosity	kg/(sm)
ν	Wavenumber	1/m
ν'_k	Stochiometric coefficient of the species k as reactant	–
ν''_k	Stochiometric coefficient of the species k as product	–
$\dot{\omega}_k$	Chemical source term of the species k	$kg/(m^3s)$
ϕ	Equivalence ratio	–
ϕ_α	General species/scalar α	–
Φ_ν	Scattering phase function	–
ψ	Azimuthal angle	sr
ψ_α	Sample or composition space of the species/scalar α	–
ρ	Density of the mixture	kg/m^3
$\sigma_{s\nu}$	Scattering coefficient	1/m
τ_ν	Optical thickness of opacity	–
τ_ϕ	Subgrid mixing time scale	s
τ_c	Chemical time scale	s
τ_K	Kolmogorov time scale	s
τ_t	Integral time scale of the flow	s
τ_{ij}	Viscous stress tensor	$kg/(m^2m)$
θ	Polar angle	sr
ε	Emissivity	–
φ	Arbitrary variable	–

ξ_{α}^{n}	n^{th} stochastic field of the species α	–
ξ_{PV}^{n}	n^{th} stochastic field of the progress variable	–
ξ_{h}^{n}	n^{th} stochastic field of the enthalpy	–
ξ_{Z}^{n}	n^{th} stochastic field of the mixture fraction	–
$\zeta(0,1)$	Dichotomic vector	–
v	Kinematic viscosity	m^2/s
v_t	Turbulent kinematic viscosity	m^2/s
v_{eff}	Effective turbulent kinematic viscosity	m^2/s

Subscript Indices

$\cdot_k$	species k
$\cdot_t$	turbulent
$\cdot_b$	burnt
$\cdot_{\mathrm{F}}$	fuel
$\cdot_l$	lean
$\cdot_{\mathrm{O}}$	oxidizer
$\cdot_{\mathrm{pv}}$	progress variable
$\cdot_r$	rich
$\cdot^{\mathrm{sgs}}$	subgrid part
$\cdot_{st}$	stochiometric
$\cdot_u$	unburnt
$\cdot_w$	wall

Operators and Symbols

$\bar{\cdot}$	Filter
$\hat{\cdot}$	Test filter
$\langle\rangle$	Average
$\sqrt{\overline{\cdot'^2}}$	Standard deviation
$\tilde{\cdot}$	Favre-filter

Dimensionless numbers

Da	Damköhler number	–
Ka	Karlovitz number	–
Le	Lewis number	–
Ma	Mach number	–
Pr	Prandtl number	–

Pr_t	Turbulent Prandtl number	–
Re	Reynolds number	–
Re_t	Turbulent Reynolds number	–
Sc	Schmidt number	–
Sc_t	Turbulent Schmidt number	–

Abbreviations

ATF	*Artificially Thickened Flame*	4
CCS	*Carbon Capture and Storage*	1
CDS	*Central Difference Scheme*	42
CFD	*Computational Fluid Dynamic*	2
CR	*Cyclic Reduction*	74
CW	*Cumulative Wavenumber*	57
DNS	*Direct Numerical Simulation*	3
DOM	*Discrete Ordinates Method*	62
ESF	*Eulerian Stochastic Field*	5
FGM	*Flamelet Generated Manifold*	4
FSCK	*Full Spectrum Correlated-k*	56
FVM	*Finite Volume Method*	62
LBL	*Line-by-Line*	5
LDA	*Laser-Doppler Anemometry*	87
LES	*Large Eddy Simulation*	3
LIF	*Laser Induced Fluorescence*	87
LIS	*Library of Iterative Solvers*	65
MPI	*Message Passing Interface*	49
OTFA	*Optically Thin Fluctuation Assumption*	6
PDF	*Probability Density Function*	4
PIV	*Particle Image Velocimetry*	96
RAM	*Random-Access Memory*	66
RANS	*Reynolds Averaged Navier-Stokes equations*	3
RTE	*Radiative Transfer Equation*	2
SIP	*Strongly Implicit Procedure*	47
SLW	*Spectral Line Weighted sum of gray gases*	56
SNB	*Statistical Narrow-Band*	60
SSOR	*Symmetric Successive Overrelaxation*	74
TCI	*Turbulence-Chemistry Interactions*	3
TKE	*Turbulent Kinetic Energy*	17
TNF	*International Workshop on Measurement and Computation of Turbulent Nonpremixed Flames*	3
TRI	*Turbulence-Radiation Interactions*	3
TVD	*Total Variation Diminishing*	42
WSGG	*Weighted Sum of Gray Gases*	5

Chapter 1

Introduction

As defined in Keating [67], combustion refers to any relatively fast exothermic chemical reaction which releases considerable energy as heat. Combustion is the most common method of energy conversion. Since the mankind discovered how to transform heat into mechanical energy, the application of combustion technology has been spreading until today. As discussed in El-Mahallawy and Habik [43], energy represents the ability to do work. For example, it enables the humankind to move rapidly and efficiently on the Earth, through the air and on the water.

As reported in [2], about 85 % of the primary energy consumption comes from combustion processes. Extensive progress has been made since the beginning of the last century to extend the knowledge and application of combustion science in order to achieve new limits. However, combustion is responsible for the emission of CO, NO_x, soot, CO_2 and others pollutants. A reduction of these gases became of international interest because of the necessity to decrease the risks associated with climate change and air pollution. Hence, having in mind that the global energy demand is expected to increase, the challenge of a global reduction in the emission of greenhouse gases and the current difficulties in developing renewable energy sources for a foreseeable future, combustion science will continue being a very important topic and a very active field of technology.

The efficiency of processes involving combustion plays a significant role in the energy scene. A higher efficiency in combustion processes can lead, for instance, to a reduction in fuel consumption, an increase of productivity or a reduction of emission of polluting gases. The energy conversion efficiency of existing combustion engines is still low. Therefore, the continuous studying and modeling of the phenomena involved in the combustion process are an urgent need. Moreover, since the parameters involved in combustion systems are affected by heat transfer, the understanding and development of mathematical models for analyses of heat transfer is crucial.

Among the various phenomena occurring in combustion systems, the radiative transfer is of significant importance. Radiation is the main mechanism of energy transfer in equipment which operates at high temperature, such as combustion chambers and furnaces. Besides that, the fraction of the total heat transfer coming from radiation grows with the combustor size [139]. Furthermore, in oxyfuel combustion radiative heat transfer plays an essential role [60, 8, 30]. Oxyfuel is part of the *Carbon Capture and Storage* (CCS) technique in which the fuel is burnt in pure oxygen together with recycled flue gas instead

of air [26]. This leads to a significantly change in the combustion process. Besides that, radiative heat transfer in this case is even more important due to the higher concentrations of CO_2 and H_2O which increase the emissivity of the flue gas. Moreover, radiative heat transfer also controls the propagation of large-scale fires, such as pool fires and forest fires.

Radiative heat transfer differs from the two modes of heat transfer conduction and convection in several ways. Unlike the other modes, radiative heat transfer does not require the presence of a medium. Moreover, while heat transfer rates are roughly proportional to the temperature difference, radiative heat transfer is roughly proportional to the difference in the temperature to the fourth power.

As discussed in Modest and Haworth [96], despite of its importance, just a little attention has been given to the accurate modeling of thermal radiation in combustion systems. In a large part of the works found in the literature, thermal radiation is ignored or treated with simplistic models. The incorporation of radiation in numerical simulations of combustion would not only increase the complexity of the problem but also the computational time. Furthermore, for considering radiation effects it is necessary to have a procedure that enables geometrical flexibility and allows the coupling with a *Computational Fluid Dynamic* (CFD) code.

The radiative heat transfer in participating media is calculated based on absorption, emission and scattering of radiative intensity from the medium and is governed by the *Radiative Transfer Equation* (RTE) [95, 58]. The RTE does not present an analytical solution and its accurate numerical solution is complicated to achieve. Radiative heat transfer occurs within the electromagnetic wave spectrum from $0.1\,\mu$m to $100\,\mu$m. Moreover, the absorption coefficient of molecular gases including carbon dioxide and water vapor varies greatly and rapidly across the spectrum, which consequently leads to a strong spectral dependency of the radiative intensity. This spectral behavior increases the difficult for modeling thermal radiation because the radiative properties of the medium have to be independently approximated for each considered wavelength.

Radiative heat transfer also causes minor pollutant species to form and interacts with soot [42]. The fields of velocity, temperature and species concentration are influenced in a decisive way by the distribution and intensity of the radiative heat flux. Therefore, the correct modeling of this mechanism is indispensable for obtaining reliable results.

According to Viskanta and Menguc [139], the major processes that need to be taken into account in a combustion system in addition to thermal radiation are: chemical kinetics, thermochemistry, molecular diffusion, laminar and turbulent fluid dynamics, eventual phase transitions and surfaces effects. Each of these phenomena needs physical models to enable the numerical study of the entire processes. Thus, a code to be applied to combustion systems should be robust for dealing with flows with strong variations of density and temperature, present a reliable turbulence modeling and have an efficient model for the computing the chemical reactions.

Studying combustion systems by taking into account radiation effects is a challenging topic because it involves thermal radiation, chemistry and turbulence, which are already

extensive topics and the interaction among the three phenomena makes the study of such problems even more complicated. Chemistry, turbulence and thermal radiation interact with each other in a highly nonlinear way, which increases the modeling difficulties. The *Turbulence-Chemistry Interactions* (TCI) occur in a two-way coupling. According to Poinsot and Veynante [109], turbulence is modified by combustion because of the strong flow accelerations through the flame front caused by heat losses and also because of the extensive changes in kinetic viscosity related to temperature variations. Turbulence can also influence chemistry, for instance, by altering the flame structure, which can lead to an increase in the chemical reaction or even inhibit it [109]. *Turbulence-Radiation Interactions* (TRI) effects can be compared to those resulting from turbulence-chemistry interactions. According to Coelho [34], the turbulence-radiation interactions may significantly increase the mean radiation intensity in turbulent flames, besides that, the flame temperature and net radiative power as well as all quantities that are influenced by temperature, e.g., NO emissions are affected.

In conclusion, combustion modeling by considering radiative heat transfer is a crucial and current topic in today's world, but unfortunately it is also a very complex subject. The next section gives a briefly overview of the main techniques used to study this topic and the main investigations related to it are outlined.

1.1 State of Research

Together with experimental approaches, CFD is an outstanding tool for studying fluid mechanics, which allows a detailed access to flow information. Its success also depends on the increase in the performance of single processors as well as the development of multi-processors and parallel architectures which have been occurring since the past few decades. Compared to experiments, its cost can be significant lower and interesting phenomena are easier to be separated and analyzed. However, CFD has to be a reliable and efficient tool in terms of the selection of procedures and modeling concerns. Therefore, equally important are experiments. The model development and validation in numerical simulations of combustion systems are mainly based on the investigation of laboratory flames. Hence, available experimental databases such as those of the *International Workshop on Measurement and Computation of Turbulent Nonpremixed Flames* (TNF) [1] are crucial.

The prediction of such complex problems with numerical techniques requires adequate models that are able to represent the physical and chemical processes involved. With *Direct Numerical Simulation* (DNS) these phenomena are exactly accounted. In this method, all spatial and time scales are explicitly captured. Although it is an accurate method, the use of DNS is restricted to relative simple problems because of its prohibitive computational costs. *Reynolds Averaged Navier-Stokes equations* (RANS) and *Large Eddy Simulation* (LES) are two feasible alternatives to DNS. In RANS, the mean flow is computed and all the fluctuations are modeled, while in LES, the large structures are explicitly captured and the subgrid-scales are approximated. LES is a more accurate method compared to RANS and has become a common model to simulate complex tur-

bulent reaction flows [54]. The LES approach was introduced by Smagorinsky [125]. His work was followed by the work of Germano et al. [49], who proposed a dynamic procedure to calculated the Smagorinsky constant, making LES a more general modeling approach.

LES is an excellent approach to deal with turbulent flows, however, its application for combustion systems is not a simple task [108]. In LES, the instantaneous form of governing equations are filtered, as a consequence unclosed terms appear which correspond to effects of the TCI and TRI. In a typical LES grid, the flame structure and species distributions can not be captured and the TCI need to be modeled. As discussed in Poinsot and Veynante [109], the relevance of TCI has long been recognized and has been an active research topic. Several approaches can be found in the literature to model TCI which are based in different assumptions. For instance, the *Artificially Thickened Flame* (ATF) model [18, 102, 37] and the G-equation formalism [70] can be cited. In the ATF model, the flame front is thickened until it can be resolved, while the flame speed is kept unchanged. On the other hand, in the G-equation approach the flame front is tracked by using the G level set function.

The explicit description of all chemical processes that occur in a combustion system involves a large number of reactions and species. For example, according to the work of Smith et al. [126], in which the GRI3.0 mechanism was employed, the combustion of methane/air mixture consisted of 325 reactions with 53 species. Moreover, the wide range of time scales that are present in chemical reaction kinetics can lead to a stiff system of equations to be solved. For these reasons, the explicit treatment of all detailed reaction mechanisms, in either DNS or LES frameworks for turbulent flows, is in technical applications not feasible.

Different strategies can be found in the literature to overcome this problem. A common approach is the reduction of the reaction mechanisms, in which it is assumed that some intermediary reactions achieve the equilibrium and some less important reactions do not participate. Another strategy that can be cited is the tabulation technique. It is based on the idea introduced by Williams [143] which postulated that 3D turbulent diffusion flames could be described with a set of one-dimensional laminar flames, called flamelets. In this approach, the flamelet solutions are calculated in a preprocessing step employing detailed chemistry. The results are then stored in a look-up table which are functions of one or more controlling variables. This way, the number of equations to be solved is significantly reduced as only transport equations for the controlling variables have to be computed. Peters [105, 106] used this idea to study diffusion flames and the mixture fraction was used to characterize the flames. Van Oijen [137] applied this tabulation technique to premixed flames by introducing the concept of reaction progress variable, leading to the *Flamelet Generated Manifold* (FGM). This strategy can be applied for both, premixed and diffusion flames, and is the one adopted in this work.

It is worth to remind that by modeling the chemical processes in LES framework does not solve the TCI problem, that still has to be modeled. For this aim, FGM can be coupled, for example, with the ATF model as it was successfully done in Künne et al. [80, 79, 81]. Another solution is treating the subgrid-scales in a statistical manner as by employing *Probability Density Function* (PDF) methods. Within this method, one possibility is to

employ a presume PDF for the subgrid-scales of each transported scalar. For example, a common shape admitted for the control variables is the so-called β PDF [115]. This approach is based on the strong assumption that the control variables are statistically independent. However, as discussed in Kuehne at al. [76], not all transported scalars can be sufficiently well described with this approximation.

An alternative approach is the transported PDF methods [110], which are more accurate but, unfortunately, also computationally more expensive, with their cost increasing exponentially with the number of variables. Different stochastic Monte Carlo solution methods have been developed to overcome this issue. In these methods, the subgrid PDF is represented by either stochastic particles or fields, i.e. obtained by a set of Eulerian stochastic differential equations. This latter strategy corresponds to the *Eulerian Stochastic Field* (ESF), which is the method used in this work. The formulation is based on the work of Valino [135] as well as Jones and Navarro-Martinez [63]. This method can be used for any flame regime and can potentially describe any given configuration. For more information about the implemented method, the reader is referred to Avdic et al. [11, 12].

By focusing the attention in the radiative heat transfer, its strong spectral dependency can be described with different models as, for example, the *Line-by-Line* (LBL) [95, 58]. In this model all the spectral lines are considered in the calculation. It is the most accurate model but, unfortunately, not feasible for engineering applications because it is time consuming. For this reason, it is used mainly as benchmark for the validation of more approximate spectral models.

A more practical approach is to employ global models, which are methods with a much reduced computational cost. In these models the total radiative heat flux or its divergence are calculated by spectrally integrating the radiative properties. One global model that can be cited is the *Weighted Sum of Gray Gases* (WSGG) [57], in which the spectral variation of the absorption coefficient is replaced by a few gray gases and transparent windows. Because of the simplicity of this model and its proved satisfactory accuracy [41], [20], [61], it is the model applied in this work.

Early studies of radiative heat transfer in RANS and LES have not considered turbulence-radiation interactions and the radiative source term has been calculated using only the mean and filtered quantities. The main reason for this neglection is the difficulty of modeling the contribution of the subgrid-scales. Only recently the importance of TRI has gained interest and more works considering TRI can be found in the literature. An extensive review about TRI in reactive flows can be found in Coelho [33]. In the following paragraphs, the main investigations related to the study of TRI in combustion systems are presented.

TRI has been firstly and mainly studied in the context of RANS. In this approach, the mean flow properties are calculated and all the fluctuations must be modeled. As reported by Coelho [34] and Li and Modest [86], ignoring TRI in the framework of RANS can result in large errors in the prediction of the radiative heat transfer. Such errors can be generated because the time-averaged radiation intensity and heat fluxes computed with the mean values may be different from those calculated with the entire values. This occurs due the highly nonlinear coupling between fluctuations of radiative intensity, temperature and

species concentrations.

The first numerical study concerning TRI was performed by Germano [48]. They analyzed the effects of random fluctuations on the radiative heat transfer by assuming a gray medium and proved the importance of the fluctuations on the results.

Mazumder and Modest [90] studied a methane-air diffusion flame in a bluff-body combustor by using the velocity-composition PDF method. They adopted the *Optically Thin Fluctuation Assumption* (OTFA), introduced in Song and Viskanta [129], and only the emission TRI was considered. In this study they found out an increase of approximately 40 % in the radiative heat loss from the flame due TRI.

Coelho [31] investigated the Sandia flame D [4, 5] using the OTFA [129] and Gaussian PDFs for the TRI. The measured temperature and species concentrations were used for the analyses. They found out an enhancement of the radiative heat loss due to the turbulent fluctuations of about 50 % for this flame.

Li and Modest [86] used the composition PDF method to investigate the importance of TRI in RANS simulations for several 2D jet flames. In this paper, the author showed that by ignoring TRI radiation, heat losses are always significantly underpredicted and as a consequence, the temperature field is substantially overpredicted. By using the same methods and framework, the Sandia flame D and two artificially scaled flames derived from it were investigated by Wang et al. [141]. They confirmed the importance of TRI for RANS context and argued that the OTFA assumption is still valid for the calculation of overall quantities, but it has significant effects on local quantities in the flame.

Additionally, Pal et al. [103] with the composition PDF method and RANS approach studied the influence of TRI on NO production for the flame D and scaled flames with and without soot. They found out that taking TRI into account results in a severely decrease in NO production.

Wu et al. [145] applied DNS for investigating the TRI in an idealized premixed system. The author used a photon Monte Carlo method [140] for solving the radiative transfer equation and analyzed the three contributions to TRI: temperature self-correlation, absorption coefficient-Planck function correlation and absorption coefficient-intensity correlation. They found out that the temperature self-correction was the dominant contribution only in the optically thin case and, besides that, for intermediate values of optical thickness, all three correlations were important.

In order to compute the filtered radiative source term in the LES framework, the contribution of the resolved scales to TRI can be explicit calculated, whereas the terms involving the subgrid-scales are unclosed. A few works investigated the importance of TRI in LES context. Coelho [34] used a semi-causal stochastic model to approximate solutions of the filtered radiative transfer equation (RTE) for the Sandia flame D and found out that the errors obtained by neglecting the TRI in LES are much smaller than those in RANS. Besides that, the author pointed out the successful extension of the OTFA approximation to LES. Furthermore, Gupta et al. [51] used a transported filtered density function (FDF) method coupled to the photon Monte Carlo method (PMC) to simulate the Sandia flame D and the artificially scaled flame D with and without soot. In this work, the authors

found out that the contribution of the subgrid-scales can be neglected for the absorption TRI. Additionally, they pointed out the importance of the subgrid-scale fluctuations to emission TRI.

In the present work the OTFA assumption is used for approximating the filtered absorption term and the ESF method is applied for representing the unclosed subgrid-scale emission TRI.

1.2 Objectives

This work has the main objective of developing and applying numerical methods for investigating turbulent combustion systems by taking into account thermal radiation effects. This study is conducted using the academic code FASTEST. This code has been used by several institutions in the context of computational fluid dynamics and in the Institute of Energy and Power Plant Technology at TU Darmstadt it has been extended to efficiently compute chemically reacting flows in complex geometries. In this work, FASTEST is extended with a radiation solver to enable the study of such complex systems by considering radiative heat transfer. In addition, the implemented solver is verified and applied for investigating the effects of radiation in two relevant flame configurations: the Sandia flame D [4, 5] and the bluff-body stabilized nonpremixed flame [1]. Moreover, the importance of *Turbulence-Radiation Interactions* (TRI) is analyzed for these flames.

The flame D is on of the standard cases of the Sandia flame series and consists of a turbulent piloted methane-air jet flame, which, according to Barlow and Frank [5], burns as diffusion flame. The second application has a higher industrial relevance: the bluff-body flame, which consists of a turbulent diffusion flame stabilized in an axisymmetric bluff body burner. Both applications are well documented cases, where experimental measurements are available.

The main objectives of this study are summarized as follows:

- Implementation of a radiation solver in FASTEST for an emitting-absorbing scattering medium by taking into consideration the spectral behavior of radiation. Herein, a three dimensional solver based on the finite volume method in block structured grids is implemented and the *Weighted Sum of Gray Gases* (WSGG) model is used for the spectral treatment of radiation.
- Verification of the implemented solver, where the solver is tested in very simple 2D to relatively complex 3D geometries and the results are compared with those from literature or analytical solutions. Besides that, the routines for computing the WSGG models are also verified.
- Study of turbulent flames without radiation effects. This is done as a prestep for the further investigations with thermal radiation. Radiation depends on the species concentration distributions and temperature field. For this reason, it is essential to assure that the code used is accurate enough for dealing with radiative heat transfer. In this step, besides the setup for the numerical simulations, the results without

radiation is presented. Herein, the Sandia flame D and bluff body configurations are described and numerically studied.

- Study of radiation effects on the Sandia flame D [4, 5] and artificially scaled flame D, where the subgrid-scale TRI are taken into focus. The scaled flame is derived by quadrupling the domain but keeping the Reynolds number constant, i. e., reducing the velocity. This case is additionally investigated because it presents larger radiation effects.
- Study of the bluff-body burner [1] and its artificially scaled configuration, done as for the previous case. The subgrid-scale TRI for these cases are also analyzed.

1.3 Thesis Outline

This thesis is structured as follows:

- Chapter 2 summarizes the theoretical background of turbulent flows and presents assumptions and modeling approaches employed in this work. The governing equations for a Newtonian fluid and a brief overview of turbulent flows are presented. Then, the filtered equations for LES are shown together with the corresponding unclosed terms, which are approximated with the Smagorinsky and Germano models.
- Chapter 3 presents the fundamentals of turbulent combustion. The basics of chemical reaction and flame modes are described. Then, the turbulence-chemistry interaction is briefly discussed. This section is followed by the combustion modeling, where the FGM model is described. For the coupling of FGM and LES, the PDF method ESF is employed. Details regarding this method are given in the last sections of this chapter.
- Chapter 4 describes the numerical methods used in this work for solving the governing equations of turbulent reacting flows. Spatial and temporal discretizations, together with the algorithm for the pressure correction, are shown in this chapter. Then, the numerical methods for solving the equations constituents of the ESF method is briefly outlined. The last section gives the overall solution procedure for a simulation without radiation effects.
- Chapter 5 discusses the theoretical background of radiative heat transfer and the numerical methods used for solving the RTE, where the FVM is shown. Basics concepts are explained and models used for treating the spectral behavior of the radiative intensity are explained. This chapter is concluded with a discussion about turbulence-radiation interaction.
- Chapter 6 presents verification tests for the radiation solver. Several tests including relative complex geometries in 3D and isotropically scattering media are shown. In addition, the WSGG models are also verified with benchmark tests.
- Chapter 7 exhibits a preliminary step for the investigations with radiation in which the employed code is validated. Herein, the configuration and setup for the Sandia

flame D and the bluff-body flame are reported together with the simulations of these cases without considering radiation effects.

- Chapter 8 investigates the Sandia flame D, the bluff-body flame and their corresponding scaled flames by taking into account radiative heat transfer. Herein, the subgrid-scale contributions to TRI are analyzed for both flames.
- Chapter 9 summarizes the thesis and proposes topics for future research in this area.

Chapter 2

Mathematical Description of Turbulent Flows

This chapter presents a brief overview of the governing equations and models necessary to compute turbulent flows. First, the basic set of equations together with the assumed simplifications are outlined. After that, a theoretical background of turbulent flows is given and in the last section the modeling approaches to compute such flows are presented.

2.1 Governing Equations

Fluids are substances that can be easily deformed, in other words, any stress applied to it will result in motion of that fluid [142]. According to Ferziger and Peric [45], although liquids and gases present a lot of differences, both types of fluids obey the same laws of motion. From the macroscopic point of view, a fluid can be considered as a continuous substance. In this case, variations in properties such as density, pressure, temperature and velocity are so smooth that the differential calculus can be applied to analyze the substance [142]. This constitutes the continuum hypothesis and it is applicable in the most technical systems. This hypothesis is considered for all analyses in this work.

In this section the fundamental equations for describing turbulent flow are shown. They consist of partial differential equations and are presented in the Einstein summation convention. The most of the notations used here are in agreement with Poinsot and Veynante [109].

The important assumption of low Mach number is done for all problems studied here. The Mach number is defined as the ratio of the flow speed to the speed of sound in the fluid. For $Ma < 0.3$, the system can be considered as incompressible. This assumption is employed in order to simplify the problem to be solved and it is discussed in more detail in Section 2.1.4.

Additionally, three nondimensional numbers important to characterize the system will be introduced:

- The Lewis number is the ratio of the thermal diffusion to the species diffusion:

$$Le_k = \frac{\lambda_T/(\rho c_p)}{\mathcal{D}_k} \,, \tag{2.1}$$

  where $\mathcal{D}_k$ is the species diffusion coefficient, λ_T denotes the thermal conductivity, ρ corresponds to the density and c_p is the specific heat capacity by constant pressure. This parameter is a local property and according to Hirschfelder et al. [56], it changes just slightly in the flame.

- The Prandtl number Pr compares momentum and heat transport,

$$Pr = \frac{v}{\lambda_T/(\rho c_p)} \,, \tag{2.2}$$

  in which v is the kinematic viscosity and it is calculated as the ratio of the dynamic viscosity μ to the density ρ, $v = \mu/\rho$.

- The Schmidt number relates momentum and species diffusion coefficient

$$Sc_k = \frac{v}{\mathcal{D}_k} \,. \tag{2.3}$$

By using these three parameters Eqs. (2.1), (2.2) and (2.3), the following relation is obtained

$$Le_k = \frac{Sc_k}{Pr} \,. \tag{2.4}$$

2.1.1 Conservation of Mass and Momentum

In the continuity equation, the time variation of the mass contained in a considered volume is equal to sum of mass fluxes through this volume surface. It leads to the differential equation

$$\frac{\partial \rho}{\partial t} + \frac{\partial}{\partial x_i}(\rho u_i) = 0 \,, \tag{2.5}$$

where u_i is the velocity component in direction i.

The conservation of momentum is obtained by applying the principle of Newtonian mechanics. In this equation the change in the rates of momentum corresponds to the sum of all acting forces. In this work gravity g is the only volumetric force considered. The momentum equation, also known as Navier-Stokes equation, is given by

$$\frac{\partial \rho u_j}{\partial t} + \frac{\partial \rho u_i u_j}{\partial x_i} = -\frac{\partial p}{\partial x_j} + \frac{\partial \tau_{ij}}{\partial x_i} + \rho g_j \,, \tag{2.6}$$

in which p is the pressure and τ_{ij} corresponds to the viscous stress tensor. This tensor can be calculated based on the Stoke's hypothesis as

$$\tau_{ij} = \mu \left(\frac{\partial u_i}{\partial x_j} + \frac{\partial u_j}{\partial x_i} \right) - \frac{2}{3} \mu \frac{\partial u_k}{\partial x_k} \delta_{ij} \ . \tag{2.7}$$

2.1.2 Species Transport

Reacting flows consist of a mixture of components and each species can be represented via its mass fraction Y_k, which gives the relative mass m of the species k to the total mass within the considered volume

$$Y_k = \lim_{V \to 0} \frac{m_k}{\sum_{\alpha=1}^{N_s} m_\alpha} \ , \tag{2.8}$$

where N_s corresponds to the total numbers of species.

The mass fraction Y_k can be also obtained by using the molar fraction of the species X_k and the mole mass of the species $\mathcal{M}_k$ and mixture $\mathcal{M}$

$$X_k = \frac{\mathcal{M}}{\mathcal{M}_k} Y_k \ , \tag{2.9}$$

$$\frac{1}{\mathcal{M}} = \sum_{k=1}^{N_s} \frac{Y_k}{\mathcal{M}_k} \ . \tag{2.10}$$

The transport equation for the mass fraction Y_k, which corresponds to the mass conservation equation for the species k, is given as

$$\frac{\partial \rho Y_k}{\partial t} + \frac{\partial}{\partial x_i} (\rho (u_i + V_{k,i}) Y_k) = \dot{\omega}_k \ . \tag{2.11}$$

In this equation, $\dot{\omega}_k$ describes the chemical source term. Besides that, $V_{k,i}$ is the diffusion velocity and represents the relative velocity of the considered species k to other components of the mixture. This variable can be approximated by using the Fick's law

$$V_{k,i} Y_k = -\mathcal{D}_k \frac{\partial Y_k}{\partial x_i} \ . \tag{2.12}$$

This formulation is employed in this work but other approaches can be found in Poinsot and Veynante [109]. The variable $\mathcal{D}_k$ in Eq. (2.12) denotes the binary diffusion coefficient and can be calculated as a function of the kinematic viscosity v and the Schmidt number Sc_k,

$$\mathcal{D}_k = \frac{v}{Sc_k} \ . \tag{2.13}$$

In order to be consistent with the chemistry tabulation as it will be seen in Section 3.4.1, the different species are assumed to have the same Schmidt number $Sc_k = Sc = 0.7$.

By adding all the transport equations for all the species, Eq. (2.11), the continuity equation Eq. (2.5) should be obtained again. For ensuring consistency, the additional conditions need to be fulfilled

$$\sum_{k=1}^{N_s} Y_k = 1 \ , \qquad \sum_{k=1}^{N_s} \dot{\omega}_k = 0 \ , \qquad \sum_{k=1}^{N_s} V_{k,i} Y_k = 0 \ . \tag{2.14}$$

2.1.3 Conservation of Energy

The energy conservation equation can be written in multiple forms, see Poinsot and Veynante [109] for more details. In this work the equation in terms of enthalpy h is adopted. The enthalpy is also used for describing the chemical system in this work. Besides that, in this form, the energy equation does not present a chemical source term [131]. It is expressed as

$$\frac{\partial \rho h}{\partial t} + \frac{\partial}{\partial x_i}(\rho u_i h) = \frac{\mathrm{D}p}{\mathrm{D}t} + \tau_{ij}\frac{\partial u_i}{\partial x_j} + \dot{\mathcal{Q}} + \rho \sum_{k=1}^{N_s} Y_k f_{k,i} V_{k,i} - \frac{\partial q_i}{\partial x_i} \ . \tag{2.15}$$

In this equation h denotes the enthalpy for a mixture and can be expressed in terms of the individual species' enthalpies h_k and their mass fractions as

$$h = \sum_{k=1}^{N_s} h_k Y_k \ . \tag{2.16}$$

The terms $\frac{\mathrm{D}p}{\mathrm{D}t}$ and $\tau_{ij}\frac{\partial u_i}{\partial x_j}$ of Eq. (2.15) describe the change of enthalpy due to pressure variations and viscous heating, respectively. For low Mach number flows, both terms can be neglected [109].

The third term of Eq. (2.15) corresponds to the heat source term. Since in this work only radiation effects are considered as external sources, this term is computed as

$$\dot{\mathcal{Q}} = S_\mathrm{r} \ , \tag{2.17}$$

where S_r corresponds to the radiative source term. This source term $\dot{\mathcal{Q}}$ is responsible for coupling the radiation solver with the flow solver. This term will be seen in details in Chapter 5.

The fourth term in Eq. (2.15) represents the volumetric forces that could act differently on each species k. Nevertheless, gravity is the only volumetric force considered in this work and it acts equally on all species $f_{k,i} = g_i$. For this reason and remembering Eq.

(2.14), this term can also be neglected,

$$\sum_{k=1}^{N_s} Y_k f_{k,i} V_{k,i} = g_i \sum_{k=1}^{N_s} Y_k V_{k,i} = 0 \ . \tag{2.18}$$

The last term in Eq. (2.15) corresponds to heat fluxes in the considered domain. Moreover, the energy flux q_i present in this term can be calculated as [109]

$$q_i = -\lambda_T \frac{\partial T}{\partial x_i} + \rho \sum_{k=1}^{N_s} h_k Y_k V_{k,i} \ , \tag{2.19}$$

where T is the temperature. Besides that, the enthalpy for each species h_k can be given as a sum of the sensible enthalpy and the formation enthalpy at T_{ref},

$$h_k = \underbrace{\int_{T_{\text{ref}}}^{T} c_{p_k} \, \mathrm{d}T}_{\text{sensible enthalpy}} + \underbrace{\Delta h_{f_k}^{\text{ref}}}_{\text{formation enthalpy}} \ , \tag{2.20}$$

where c_{p_k} denotes the specific heat capacity of each species. Furthermore, the specific heat capacity for a mixture is calculated as

$$c_p = \sum_{k=1}^{N_s} c_{p_k} Y_k \ . \tag{2.21}$$

If Eqs. (2.21), (2.16) and Fick's law Eq. (2.12) are applied in Eq. (2.19), after some mathematical arrangements it yields

$$q_i = -\frac{\lambda_T}{c_p} \frac{\partial h}{\partial x_i} + \sum_{k=1}^{N_s} \left(h_k \frac{\partial Y_k}{\partial x_i} \left(\frac{\lambda_T}{c_p} - \rho \mathcal{D}_k \right) \right) \ . \tag{2.22}$$

In order to simplify this equation even more, the already defined Lewis number Eq. (2.1) is used to replace the term λ_T / c_p in the second term of Eq. (2.22). Furthermore, in this work, it is assumed Lewis number equals one, $Le = 1$. Finally, the transport equation for the enthalpy Eq. (2.15) can be rewritten as follows

$$\frac{\partial \rho h}{\partial t} + \frac{\partial}{\partial x_i}(\rho u_i h) = S_{\text{r}} + \frac{\partial}{\partial x_i} \left(\frac{\lambda_T}{c_p} \frac{\partial h}{\partial x_i} \right) \ . \tag{2.23}$$

Once more, the coefficients in the diffusion term in Eq. (2.23) can be expressed in terms of the Prandtl number Pr Eq. (2.2). For this aim, the relation given in Eq. (2.4) together with the assumption of $Le = 1$ leads to $Sc = Pr$ and to

$$\frac{\lambda_T}{c_p} = \frac{\mu}{Pr} \ . \tag{2.24}$$

2.1.4 The Equation of State

In order to close the system of equations, the thermal equation of state is employed,

$$\rho = \frac{p}{T}\frac{\mathcal{M}}{\mathcal{R}} \,, \tag{2.25}$$

where $\mathcal{R}$ is the ideal gas constant and $\mathcal{M}$ is the mean molar mass of the mixture.

As mentioned before, in this work the low Mach number hypothesis is assumed and according to Poinsot and Veynante [109] , for combustion with low Mach numbers, the changes in the mean pressure are negligible and a constant pressure p^{ref} can be applied in Eq. (2.25).

2.1.5 Summary of the Employed Equations

All governing equations presented above form a closed system of equations to be solved. The employed equations are summarized as follows:

- Conservation of mass

$$\frac{\partial \rho}{\partial t} + \frac{\partial}{\partial x_i}(\rho u_i) = 0 \tag{2.26}$$

- Conservation of momentum

$$\frac{\partial \rho u_j}{\partial t} + \frac{\partial \rho u_i u_j}{\partial x_i} = -\frac{\partial p}{\partial x_j} + \frac{\partial}{\partial x_i}\left[\mu\left(\frac{\partial u_i}{\partial x_j} + \frac{\partial u_j}{\partial x_i}\right) - \frac{2}{3}\mu\frac{\partial u_k}{\partial x_k}\delta_{ij}\right] + \rho g_j \tag{2.27}$$

- Species transport

$$\frac{\partial \rho Y_k}{\partial t} + \frac{\partial}{\partial x_i}(\rho u_i Y_k) = \frac{\partial}{\partial x_i}\left(\rho\mathcal{D}\frac{\partial Y_k}{\partial x_i}\right) + \dot{\omega}_k \quad \text{with} \quad \rho\mathcal{D} = \frac{\mu}{Sc} \tag{2.28}$$

- Conservation of energy

$$\frac{\partial \rho h}{\partial t} + \frac{\partial}{\partial x_i}(\rho u_i h) = S_{\text{r}} + \frac{\partial}{\partial x_i}\left(\frac{\lambda_T}{c_p}\frac{\partial h}{\partial x_i}\right) \quad \text{with} \quad \frac{\lambda_T}{c_p} = \frac{\mu}{Pr} \tag{2.29}$$

- Thermal equation of state

$$\rho = \frac{p^{\text{ref}}}{T}\frac{\mathcal{M}}{\mathcal{R}} \tag{2.30}$$

2.2 Turbulence

In general a flow can be classified in three different regimes: laminar, transitional and turbulent. A nondimensional parameter, Reynolds number Re, is commonly used to characterize these regimes [121],

$$Re = \frac{\mathcal{U}\mathcal{L}}{v} , \tag{2.31}$$

where $\mathcal{U}$ and $\mathcal{L}$ are the characteristic velocity and the length scales of the bulk flow, respectively. This parameter expresses the ratio of the inertial forces to the viscous forces.

For low Re, each fluid particle follows a smooth trajectory and in this case the flow is classified as laminar. As the flow speed is increased, consequently, Re also increases and it may lead to instabilities and a more random type of flow can be produced, called turbulent [45]. Furthermore, the intermediate regime is called transition.

Most flows encountered in engineering applications are turbulent and the present work is focused on this regime. Such flows are highly unsteady, three-dimensional and dissipative. They fluctuate on a wide range of length and time scales.

In order to quantify the fluctuation present in a flow, the time-averaged velocity $\langle u \rangle$ is calculated from the instantaneous velocity u over a time interval Δt as

$$\langle u \rangle = \frac{1}{\Delta t} \int_0^{\Delta t} u(t) \mathrm{d}t . \tag{2.32}$$

In addition, the corresponding fluctuation part is $u' = u - \langle u \rangle$.

The aforementioned range of different scales present in a turbulent flow can be represented in an energy spectrum. According to Pope [111], such spectrum shows how the *Turbulent Kinetic Energy* (TKE) is distributed among the eddies of different sizes. The TKE is defined as [111]

$$\mathrm{TKE} = \frac{1}{2} u_i' u_i' . \tag{2.33}$$

Besides that, the spectrum of the TKE $E(\nu)$ can be determined from the TKE,

$$\mathrm{TKE} = \int_0^{\infty} E(\nu) \mathrm{d}\nu . \tag{2.34}$$

This spectrum depends on the wavenumber $\nu = 2\pi/l$, where l is the length scale. The energy spectrum for a turbulent flow is shown in Fig. 2.1. In the production zone, energy is injected in the flow and it is transferred among the turbulent structures in two forms: direct, i. e. from the largest to the smallest, or inverse, from the smallest to the largest. In the inertial subrange and dissipation area, it can be noted that the largest structures which have the smallest wavenumbers contain greater amount of energy, while the smaller structures, with larger wavenumbers, carry smaller amount of energy. The process of nonlinear energy transfer between the different scales prevails in the inertial

area. The energy spectrum in this region decreases following a characteristic slope of $\nu^{-5/3}$. Moreover, in the dissipation area, the viscous forces are sufficiently large to dissipate the energy contained in the small structures and no smaller vortices are then formed. For a more in-depth knowledge and comprehensive description of turbulent flows, the reader is referred to Lesieur [85] and Pope [111]

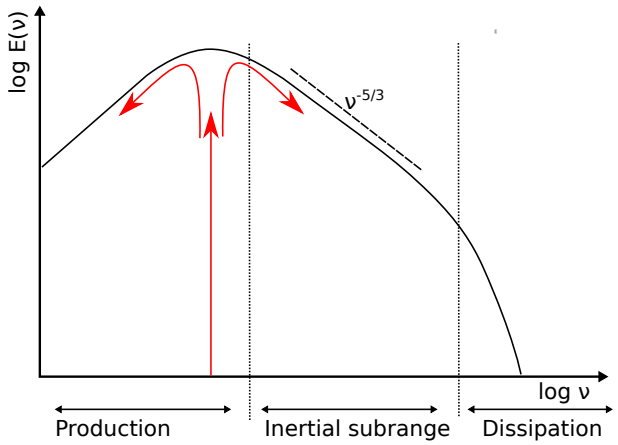

Figure 2.1: Kinetic energy spectrum for a turbulent flow.

Before presenting the computational approaches for modeling turbulent flows, it is interesting to estimate the range of turbulent scales present in a turbulent flow. For this purpose, the integral length scale l_t and its corresponding characteristic velocity $u(l_t)$ are introduced. The variable l_t can be understood as a typical length scale, for example, the length of the largest eddies present in the considered flow. By using these parameters, the turbulent Reynolds number can be defined

$$Re_t = \frac{u(l_t)l_t}{v} \ . \tag{2.35}$$

Following the Kolmogorov's theory, the smallest-scale of motions represent a characteristic length scale which can be denoted as Kolmogorov dissipative scale l_d [85],

$$l_d = \left(\frac{v^3}{\epsilon}\right)^{1/4} \ , \tag{2.36}$$

where ϵ is the rate of dissipation. This parameter can be approximated by

$$\epsilon \approx \frac{u(l_t)^2}{l_t/u(l_t)} = \frac{u(l_t)^3}{l_t} \ . \tag{2.37}$$

Finally, the multiplicity of scales in a turbulent flow can be expressed by the ratio of the integral length scale to the Kolmogorov length scale

$$\frac{l_t}{l_d} \approx \frac{u(l_t)^3/\epsilon}{(v^3/\epsilon)^{1/4}} = Re_t^{3/4} \ . \tag{2.38}$$

This ratio represents an estimation of the number of degrees of freedom which are needed to describe the motion in each direction of the space. Therefore, the total number of degrees of freedom is of the order of $Re_t^{9/4}$ in three dimensions. As it can be seen by analyzing this equation, an increase of the turbulent Reynolds number leads to an increase in the range of length scales which have to be captured.

2.2.1 Turbulent Modeling

Three main computational approaches can be used to simulate turbulent flows: DNS, LES and RANS. Their definitions together with their advantages and disadvantages are presented bellow.

In DNS the complete system of equations shown in Section 2.1.5 for their instantaneous quantities are solved. In this case no turbulence model is used and all space and time scales of the turbulent structures present in the flow, from the largest length to the Komogorov length scale, are explicitly solved. Moreover, by analyzing Eq. (2.38), it is easy to note that for the current state of computer technology DNS can only be carried out for simple academic flows or flows with relatively low-Reynolds-number. For the most engineering applications it is infeasible because of the huge number of grid points necessary for the calculations and, consequently, the computational costs become prohibitive.

In the RANS approach the range of scales are reduced by time averaging the instantaneous Eqs. (2.26) - (2.30). Each quantity in the system of equations is split into a mean and its corresponding fluctuation value, yielding unclosed correlations which have to be approximated. In this approach, the entire range of wavenumber are modeled as shown in Fig. 2.2. Therefore, errors emerging from the modeling can drastically affect the simulation. RANS is applied when information about the time-averaged mean quantities is sufficient and the full three dimensional unsteady flow evolution is not required. For turbulent reacting flows unsteady effects are very important and only mean quantities may be insufficient. In this case, as for the problems explored in this work, LES can be used to overcome the drawbacks of RANS without having a prohibitive computational cost as DNS.

In LES the largest structures present in the turbulent flow, generally the ones larger than the length of the grid cell, are explicitly calculated while the smallest ones are modeled. In this approach the system of equations in Section 2.1.5 is filtered and, as in the RANS approach, unclosed correlations appear. Again, these terms have to be modeled, but in this approach, only structures presenting length scale smaller than the cut-off length scale are modeled, as it can be seen in Fig. 2.2. According to Pope [111], LES is expected to tend toward DNS when the cut-off length scale tends to zero. Moreover, it represents a combination of DNS and RANS. This approach is employed in this work and is discussed in detail in Section 2.2.2.

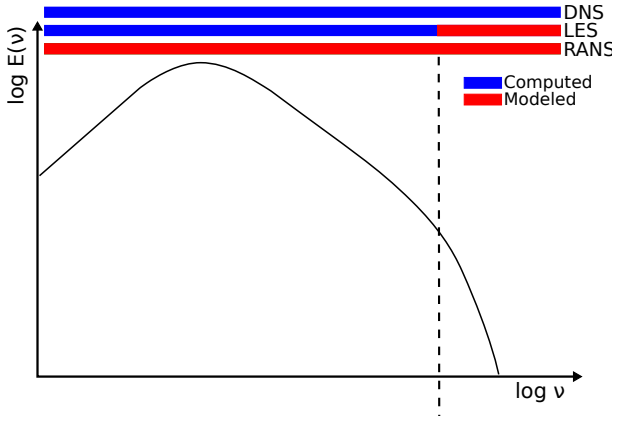

Figure 2.2: Kinetic energy spectrum for turbulent flows showing the difference among the three approaches: DNS, RANS and LES. The explicitly resolved region is illustrated in blue while the modeled part in red.

2.2.2 Large Eddy Simulation

As aforementioned, in LES the smaller scales are filtered out by applying a $\mathcal{G}$ low pass filter. An arbitrary filtered quantity φ is defined as

$$\bar{\varphi}(x_i) = \int \varphi(x_i') \, \mathcal{G}(x_i - x_i') \mathrm{d}x_i' \, . \tag{2.39}$$

Different filter functions and procedures can be found in the literature, see Pope [111] and Poinsot and Veynante [109]. In this work, the filter procedure is done implicitly by using the grid length. Such procedure corresponds to a box filter in physical space [109],

$$\mathcal{G}(x_i) = \begin{cases} \Pi_{i=1}^{3} \frac{1}{\Delta_i} & \text{if } |x_i| \leq \Delta_i/2, \; i = 1,2,3 \\ 0 & \text{otherwise} \end{cases} \tag{2.40}$$

where Δ_i is the grid cell length in direction i.

Once the filter is applied, the arbitrary variable φ can be split into a filtered $\bar{\varphi}$ (resolved) and a subgrid φ^{sgs} (unresolved) scale,

$$\varphi = \bar{\varphi} + \varphi^{\mathrm{sgs}} \, . \tag{2.41}$$

In order to avoid additional unclosed terms due to nonconstant density as in combustion systems, a density-weighted filtering called Favre-filtering [44] is used,

$$\widetilde{\varphi} = \frac{\overline{\rho\varphi}}{\bar{\rho}} \, . \tag{2.42}$$

Again here φ can be separated into resolved $\widetilde{\varphi}$ and subgrid-scales φ'':

$$\varphi = \widetilde{\varphi} + \varphi'' \, . \tag{2.43}$$

By applying the filtering to the balance equations presented in Section 2.1.5 it results in the set of equations:

- Conservation of mass

$$\frac{\partial \overline{\rho}}{\partial t} + \frac{\partial}{\partial x_i}\left(\overline{\rho}\widetilde{u}_i\right) = 0 \tag{2.44}$$

- Conservation of momentum

$$\frac{\partial}{\partial t}\left(\overline{\rho}\ \widetilde{u}_j\right) + \frac{\partial}{\partial x_i}\left(\overline{\rho}\ \widetilde{u}_i\widetilde{u}_j\right) = \frac{\partial}{\partial x_i}\left(\overline{\tau}_{ij} - \overline{\rho}\left(\widetilde{u_i u_j} - \widetilde{u}_i\widetilde{u}_j\right)\right) - \frac{\partial \overline{p}}{\partial x_j} + \overline{\rho} g_j \tag{2.45}$$

- Species transport

$$\frac{\partial \overline{\rho}\widetilde{Y}_k}{\partial t} + \frac{\partial}{\partial x_i}\left(\overline{\rho}\ \widetilde{u}_i\widetilde{Y}_k\right) = \frac{\partial}{\partial x_i}\left(\frac{\overline{\mu}}{Sc}\frac{\partial \widetilde{Y}_k}{\partial x_i} - \overline{\rho}\left(\widetilde{u_i Y_k} - \widetilde{u}_i\widetilde{Y}_k\right)\right) + \overline{\dot{\omega}}_k \tag{2.46}$$

- Conservation of energy

$$\frac{\partial \overline{\rho}\widetilde{h}}{\partial t} + \frac{\partial \overline{\rho}\widetilde{u}_i\widetilde{h}}{\partial x_i} = \overline{S}_{\mathrm{r}} + \frac{\partial}{\partial x_i}\left(\frac{\overline{\mu}}{Pr}\frac{\partial \widetilde{h}}{\partial x_i} - \overline{\rho}\left(\widetilde{u_i h} - \widetilde{u}_i\widetilde{h}\right)\right) \tag{2.47}$$

In this set of equations the following unclosed terms appear and need to be modeled:

$$\widetilde{\sigma}_{ij}^{\mathrm{sgs}} = \widetilde{u_i u_j} - \widetilde{u}_i\widetilde{u}_j \tag{2.48}$$

$$\widetilde{\sigma}_{Y_k}^{\mathrm{sgs}} = \widetilde{u_i Y_k} - \widetilde{u}_i\widetilde{Y}_k \tag{2.49}$$

$$\widetilde{\sigma}_{h}^{\mathrm{sgs}} = \widetilde{u_i h} - \widetilde{u}_i\widetilde{h}\ . \tag{2.50}$$

These terms correspond to the subgrid-scale tensor, species flux and enthalpy flux, respectively.

The modeling approach employed to close this set of equations is based on the diffusive characteristic of turbulent flows. The unresolved subgrid-scale tensor are approximated according to the Boussinesq assumption [109]. This is done by introducing a turbulent viscosity v_t which is combined with the molecular viscosity and an effective viscosity is obtained $v_{\mathrm{eff}} = v + v_t$. By applying this eddy-viscosity approach, it yields

$$\widetilde{\sigma}_{ij}^{\mathrm{sgs}} - \frac{1}{3}\widetilde{\sigma}_{kk}^{\mathrm{sgs}}\delta_{ij} = -2v_t\left(\widetilde{S}_{ij} - \frac{\delta_{ij}}{3}\widetilde{S}_{kk}\right)\ , \tag{2.51}$$

where $\widetilde{\sigma}_{ij}^{\mathrm{sgs}}$ and $\frac{1}{3}\widetilde{\sigma}_{kk}^{\mathrm{sgs}}\delta_{ij}$ are the anisotropic and isotropic parts of the Reynolds stresses. Besides that, $\widetilde{S}_{ij}$ denotes the filtered strain rate

$$\widetilde{S}_{ij} = \frac{1}{2}\left(\frac{\partial \widetilde{u}_i}{\partial x_j} + \frac{\partial \widetilde{u}_j}{\partial x_i}\right)\ . \tag{2.52}$$

The isotropic contribution in Eq. (2.51) is usually added to the filtered pressure given a modified pressure

$$\overline{P} = \overline{p} + \frac{1}{3}\overline{\rho}\overline{\vartheta}^{\text{sgs}}_{kk} \ . \tag{2.53}$$

The Smagorinsky model The turbulent viscosity v_t can be computed by employing the Smagorinsky model [125]. In this model, v_t is obtained from dimensional arguments and it is given as

$$v_t = C_s^2 \Delta^{4/3} l_t^{2/3} (2\widetilde{S}_{ij}\widetilde{S}_{ij})^{1/2} \ , \tag{2.54}$$

with Δ being the grid size, l_t the turbulence integral length scale and C_s a model constant. Suggested values for C_s varies between 0.065 and 0.2. As in Pope [111], for the simulations carried out here C_s is set to 0.17. Furthermore, Eq. (2.54) can be simplified by considering $l_t \approx \Delta$, yielding

$$v_t = (C_s \Delta)^2 (2\widetilde{S}_{ij}\widetilde{S}_{ij})^{1/2} \ . \tag{2.55}$$

The Germano model Germano et al. [49] developed a dynamic procedure to calculate the model constant C_s of the Smagorinsky model Eq. (2.55). This parameter is calculated based on the size of the resolved eddies and it depends on time and position. In this procedure, a second larger filter ($\widehat{\Delta} > \Delta$) is applied to Eq. (2.45) and, analogous to Eq. (2.48), it yields

$$\widehat{\overline{\vartheta}}_{ij} = \widehat{\overline{u_i}\overline{u}_j} - \widehat{\overline{u}}_i \widehat{\overline{u}}_j \ . \tag{2.56}$$

Furthermore, by applying this second filter to Eq. (2.48), it leads to

$$\widehat{\overline{\vartheta}^{\text{sgs}}_{ij}} = \widehat{\overline{u_i}\overline{u}_j} - \widehat{\widetilde{u}_i}\widehat{\widetilde{u}_j} \ . \tag{2.57}$$

The so-called Leonard term L_{ij} is computed by subtracting the last two equations and, this way, information lost due to the second filtering is obtained,

$$L_{ij} \coloneqq \widehat{\overline{u}_i}\widehat{\overline{u}_j} - \widehat{\overline{u}}_i\widehat{\overline{u}}_j = \widehat{\overline{\vartheta}}_{ij} - \widehat{\overline{\vartheta}^{\text{sgs}}_{ij}} \ . \tag{2.58}$$

The above relation is known as Germano identity. If the same model assumption as in Eq. (2.55) is applied to $\overline{\vartheta}^{\text{sgs}}_{ij}$ and to $\widehat{\overline{\vartheta}}_{ij}$, it gives

$$-2C\overline{m}^{\text{sgs}}_{ij} \coloneqq \overline{\vartheta}^{\text{sgs}}_{ij} - \frac{1}{3}\overline{\vartheta}^{\text{sgs}}_{kk}\delta_{ij} = -2C\Delta^2(2\widetilde{S}_{ij}\widetilde{S}_{ij})^{1/2}\left(\widetilde{S}_{ij} - \frac{1}{3}\widetilde{S}_{kk}\delta_{ij}\right) \tag{2.59}$$

$$-2C\widehat{\overline{m}}_{ij} \coloneqq \widehat{\overline{\vartheta}}_{ij} - \frac{1}{3}\widehat{\overline{\vartheta}}_{kk}\delta_{ij} = -2C\widehat{\Delta}^2(2\widehat{\widetilde{S}}_{ij}\widehat{\widetilde{S}}_{ij})^{1/2}\left(\widehat{\widetilde{S}}_{ij} - \frac{1}{3}\widehat{\widetilde{S}}_{kk}\delta_{ij}\right) \ , \tag{2.60}$$

where $C = C_s^2$. Then, the definition $M_{ij} \coloneqq \widehat{m^{\text{sgs}}_{ij}} - \widehat{\overline{m}}_{ij}$ is used together with the Eqs. (2.58)- (2.60) and the following relation is obtained

$$2CM_{ij} = L_{ij} - \frac{1}{3}L_{kk}\delta_{ij} \ , \tag{2.61}$$

which represents five linearly independent equations for the determination of the Smagorinsky coefficient. However, C can not satisfy all of them at the same time. Thus, Lilly [87] proposed the minimization of the mean square residual, resulting in

$$C = \frac{M_{ij}L_{ij} - \frac{1}{3}L_{kk}\delta_{ij}M_{ij}}{2M_{ij}M_{ij}} = \frac{M_{ij}L_{ij}}{2M_{ij}M_{ij}} \,. \tag{2.62}$$

Unfortunately, according to Pope [111] this formulation can lead to spatial and temporal fluctuations. For this reason, Hahn [53] and Olbricht [101] used a temporal relaxation procedure to overcome the problem,

$$C\left(t^{n+1}\right) = (1 - w_g)\, C\left(t^n\right) + w_g \frac{M_{ij}L_{ij}}{2M_{ij}M_{ij}} \,, \tag{2.63}$$

in which $w_g = 10^{-2}$ is a weighting factor. However, this procedure can produce negative values for the turbulent viscosity. Therefore a restriction as $0 \leq C\left(t^{n+1}\right) \leq 1$ is employed.

Finally, the unclosed terms of the enthalpy and species transport equations are modeled by using the gradient flux approach resulting to

$$\widetilde{\mathfrak{d}}_h^{\mathrm{sgs}} = \widetilde{u_i h} - \widetilde{u}_i \widetilde{h} = -\frac{v_t}{Pr_t}\frac{\partial \widetilde{h}}{\partial x_i} \,, \tag{2.64}$$

$$\widetilde{\mathfrak{d}}_{Y_k}^{\mathrm{sgs}} = \widetilde{u_i Y_k} - \widetilde{u}_i \widetilde{Y}_k = -\frac{v_t}{Sc_t}\frac{\partial \widetilde{Y_k}}{\partial x_i} \,, \tag{2.65}$$

where Pr_t and Sc_t are the turbulent Prandtl and Schmidt numbers. These turbulent parameters are commonly assumed to be equal to the laminar ones [59]. Remembering the assumption done in Section 2.1.2, these turbulent parameters are set to $Sc = Pr = 0.7$.

2.3 Summary

In this chapter the fundamental equations to describe turbulent flows were presented. First, the governing equations and important relations were introduced. Also the assumed simplifications leading to the final employed equations were addressed. After that, a brief overview of turbulence and its modeling were given. Finally, the turbulence models used in this work were described.

Two terms have not been discussed so far: the chemical source term $\overline{\dot{\omega}}_k$ and the radiation source term $\overline{S}_r$. In order to compute these terms, a theoretical background of combustion and radiation will be given in the Chapters 3 and 5, respectively. Additionally, the approaches employed to calculate these filtered source terms will be addressed in detail.

Chapter 3

Fundamentals of Combustion and Modeling Reacting Flows

In this chapter, a theoretical background of turbulent reacting flows is presented together with the modeling approach used in this work to describe them.

In the first sections, the fundamentals about chemical reaction kinetics are given and the flame modes are discussed. Then, a brief overview of turbulence-chemistry interaction is presented. This is followed by a general discussion about combustion modeling and the flamelet generated manifold approach is addressed. Finally, the stochastic field method is described, which is used for the coupling between the employed combustion approach and the LES solver.

3.1 Fundamentals of Chemical Reaction

According to El-Mahallawy and Habik [43], combustion is defined as a rapid exothermic reaction in which energy is liberated as heat. Furthermore, it depends on dynamic, time-dependent events that occur on a molecular level. Besides that, flames denote combustion reactions that are able to propagate through a medium.

A chemical reaction equation provides a mathematical means for reactive systems in which the change of composition and mass conservation is expressed [67]. Moreover, a combustion reaction is a chemical reaction in which a fuel combines with an oxidizer (usually oxygen from air) to form combustion products. An example is the global reaction of the combustion of methane CH_4 in dry air (mixture of O_2 and N_2),

$$\nu'_{\mathrm{CH_4}}\mathrm{CH_4} + \nu'_{\mathrm{O_2}}\mathrm{O_2} + \nu'_{\mathrm{N_2}}\mathrm{N_2} \rightarrow \nu''_{\mathrm{CO_2}}\mathrm{CO_2} + \nu''_{\mathrm{H_2O}}\mathrm{H_2O} + \nu''_{\mathrm{N_2}}\mathrm{N_2}\ , \tag{3.1}$$

in which the products are water H_2O and carbon dioxide CO_2. If the theoretical amount of oxidant to complete the combustion of the fuel is present and the most stable products are formed, it can be expressed in terms of stoichiometric equation. The stoichiometric coefficients for the above global reaction are:

$$\nu'_{\mathrm{CH_4}} = 1, \quad \nu'_{\mathrm{O_2}} = 2, \quad \nu''_{\mathrm{CO_2}} = 1, \quad \nu''_{\mathrm{H_2O}} = 2 \quad \text{and} \quad \nu'_{\mathrm{N_2}} = \nu''_{\mathrm{N_2}} = 2 \cdot \frac{0.79}{0.21}\ . \tag{3.2}$$

This global reaction is a simplification of the real chemical process. In reality the reactants, methane and dry air, do not turn into the final products at once, instead of it, many elementary reactions exist and hundreds of intermediate species are formed.

3.1.1 Chemical Reaction Kinetics

Reaction kinetics is about how fast each elementary reaction proceeds. A stoichiometric relation describing M chemical elementary reactions of arbitrary complexity can be represented as

$$\sum_{k=1}^{N_s} \nu'_{kj} \mathcal{X}_k \rightleftarrows \sum_{k=1}^{N_s} \nu''_{kj} \mathcal{X}_k \quad \text{for} \quad j = 1,M \ , \tag{3.3}$$

where N_s denotes the number of species $\mathcal{X}_k$ involved, ν'_{kj} and ν''_{kj} are the stoichiometric coefficient of the species k in the reaction j. The arrows in this equation indicate that it may evolve in both directions.

In chemical kinetics the reaction rate is defined as the mass in moles per unit time in which reactants are converted into products. The rates constant for the forward and backward reactions ($\mathrm{K}_{f,j}$ and $\mathrm{K}_{b,j}$) are commonly described with the Arrhenius law:

$$\mathrm{K}_{m,j} = \mathrm{A}_{m,j} \exp\left(-\frac{\mathrm{E}_{m,j}}{\mathcal{R}T}\right) \quad \text{for} \quad m \in \{f,b\} \ . \tag{3.4}$$

In this equation $\mathrm{A}_{m,j}$ is the gas kinetic collision frequency and $\exp\left(-\frac{\mathrm{E}_{m,j}}{\mathcal{R}T}\right)$ is the Boltzmann factor, where $\mathrm{E}_{m,j}$ denotes the activation energy.

$\mathrm{K}_{f,j}$ and $\mathrm{K}_{b,j}$ can be combined in order to calculate the total reaction rate $\mathcal{Q}_j$ of an elementary reaction:

$$\mathcal{Q}_j = \mathrm{K}_{f,j} \prod_{k=1}^{N_s} [X_k]^{\nu'_{kj}} - \mathrm{K}_{b,j} \prod_{k=1}^{N_s} [X_k]^{\nu''_{kj}} \ , \tag{3.5}$$

where $[X_k] = \rho Y_k / \mathcal{M}_k$ is the molar concentration of the species k. Once the total reaction rate is calculated, the chemical source term $\dot{\omega}_k$ of the species k, that is necessary for calculating the species transport equation 2.28, can be computed as

$$\dot{\omega}_k = \sum_{j=1}^{M} \dot{\omega}_{k,j} = \mathcal{M}_k \sum_{j=1}^{M} \nu_{kj} \mathcal{Q}_j \ , \tag{3.6}$$

with $\nu_{kj} = \nu''_{kj} - \nu'_{kj}$.

3.2 Flame Modes

Before investigating more complex flame configurations, it is important to study fundamental flame structures. Therefore, the basic types of flames are briefly presented in this section. There are two general types of flames:

- **Premixed flames**, in which the fuel and oxidizer are mixed before reaching the flame region. As outlined in El-Mahallawy and Habik [43], these flames can only be obtained if the initial reactants mixture lies between certain composition limits called the composition limits of flammability.
- **Diffusion flames**, also known as nonpremixed flames, in which the mixture of fuel and air, as well the combustion, occur at the interface.

These flames differ from each other in many aspects such as local flame structure, temperature distribution and dynamic behavior.

Before studying these flames separately, it is necessary to quantify the reactants present in a mixture. The equivalence ratio denotes the fuel-oxidizer ratio normalized with its value in stoichiometric conditions:

$$\phi = \left(\frac{Y_\mathrm{F}}{Y_\mathrm{O}}\right) / \left(\frac{Y_\mathrm{F}}{Y_\mathrm{O}}\right)_{st} , \tag{3.7}$$

where the subindex O and F denote oxidizer and fuel, respectively. Besides that, the subindex *st* corresponds to the stoichiometric condition.

As defined in Keating [67], a fuel-air mixture having excess air is termed a fuel-lean mixture ($\phi < 1$), while a mixture that has excess fuel is called a fuel-rich mixture ($\phi > 1$). The stoichiometric conditions for methane combustion are given as

$$\left(\frac{Y_{\mathrm{CH_4}}}{Y_{\mathrm{O_2}}}\right)_{st} = \frac{\nu'_{\mathrm{CH_4}}\mathcal{M}_{\mathrm{CH_4}}}{\nu'_{\mathrm{O_2}}\mathcal{M}_{\mathrm{O_2}}} = \frac{1}{4} . \tag{3.8}$$

Alternatively, a mixture can be described with the mixture fraction Z, which is a linear combination of the mass fractions of reactants. In this work, the mixture fraction is defined in terms of atomic elements. A transport equation for this quantify, assuming equal diffusivity and proper normalization, was derived in Poinsot and Veynante [109],

$$\frac{\partial \rho Z}{\partial t} + \frac{\partial}{\partial x_j}(\rho u_j Z) = \frac{\partial}{\partial x_j}\left(\rho \mathcal{D} \frac{\partial Z}{\partial x_j}\right) , \tag{3.9}$$

in which Z can be also seen as a passive scalar.

The element mixture fraction for a considered atomic element p is defined as

$$Z_p = \sum_{k=1}^{N_s} a_{kp} \frac{\mathcal{M}_p}{\mathcal{M}_k} Y_k , \tag{3.10}$$

where a_{kp} is the number of atomic element p in the chemical species k. Moreover, the mixture fraction is defined in the way that it has value zero if only oxidizer is present and is unity if only fuel exists. It yields

$$Z = \frac{Z_p - Z_{p,O}}{Z_{p,F} - Z_{p,O}} \, . \tag{3.11}$$

The equivalence ratio can also be calculated in terms of the mixture fraction as

$$\phi = \frac{Z}{1-Z} \frac{1-Z_{st}}{Z_{st}} \, , \tag{3.12}$$

where Z_{st} corresponds to the mixture fraction in stoichiometric conditions.

As described in El-Mahallawy and Habik [43], if only a sufficient quantity of fuel is added to an oxidizer so that the mixture just becomes flammable, the percentage of fuel at this point is called lower flammable limit or lean limit ϕ_l. The contrary is called upper flammability limit or rich limit ϕ_r and it happens if more fuel is added until the point is reached at which the mixture will no longer burn. The flammability limits for methane in air are [78]

$$0.48 = \phi_l < \phi < \phi_r = 1.77 \quad \text{oder} \quad 0.0278 = Z_l < Z < Z_r = 0.0944 \, . \tag{3.13}$$

3.2.1 Nonpremixed Flames

As briefly described above, the flames in this case appear at the border between the fuel and oxidizer. They are safer to operate and nonpremixed burners are simpler to design. Thus, they have far greater practical application than premixed flames.

A simple case to exemplify this kind of flame is presented in Fig. 3.1 (a). In this configuration, the fuel and oxidizer flow in opposed directions, against each other. The reactants have to diffuse in order to mix and to react [43]. According to Keating [67], differing from premixed flames, diffusion flames depend on the mixing rate between reactants more than on kinetic mechanisms. Furthermore, no parameter as flame speed or characteristic thickness can be used for these flames.

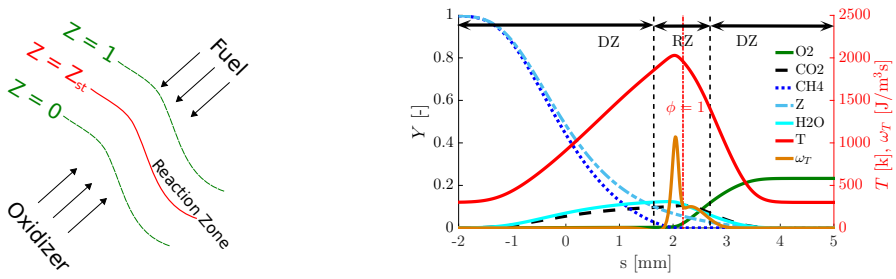

(a) (b)

Figure 3.1: (a) Basic representation of a diffusion flame and (b) species distribution of a one-dimensional nonpremixed methane-air flame with $a = 100\,\mathrm{s}^{-1}$ and $T_u = 300\,\mathrm{K}$.

The structure of such flames depends on the relation between the characteristic time scales of chemistry and diffusion, which relates to the thickness of the mixing zone. Moreover, these flames do not propagate and their location is determined by mixing.

In this configuration, the strain rate a is an important parameter in order to quantify the spatial extent of the flame structure. It is expressed as

$$a = \frac{u_{\mathrm{F}} + u_{\mathrm{O}}}{h} \, ,$$

where h corresponds to the distance between the positions where the velocities u_{F} and u_{O} are measured.

Fig. 3.1(b) shows the structures of a diffusion methane flame with $a = 100\,\mathrm{s}^{-1}$ and unburnt temperature $T_u = 300\,\mathrm{K}$. Three different regions can be identified in this figure: two diffusion zones (DZ), in which the reactants are mixed but the mixture composition is outside the flammability limits, and a reaction zone (RZ), where combustion takes place. Compared to premixed flames, diffusion flames have a wider reaction zone. In order to indicate the chemical reaction, the heat release ω_T is additionally plotted in this figure. It can be observed that its maximum, as well as the maximum of the temperature profile, is located close to stoichiometric conditions.

The reaction zone in diffusion flames may be very thin, depending on how fast chemical reactions are; in the limit of an infinitely fast reaction, the reaction zone is also infinitely thin.

3.2.2 Premixed Flames

A simple premixed flame scheme is depicted in Fig. 3.2(a). In this case, reactants are already mixed before approaching the flame front. The progress of the reaction can be described with the normalized progress variable $Y_{\mathrm{n,pv}}$, which is also shown in Fig. 3.2(a). In the transition of unburnt to burnt, $Y_{\mathrm{n,pv}}$ increases from zero in the unburnt region to one in the burnt state. It is calculated with the reaction progress variable Y_{pv} as

$$Y_{\mathrm{n,pv}} = \frac{Y_{\mathrm{pv}} - Y_{\mathrm{pv,min}}}{Y_{\mathrm{pv,max}} - Y_{\mathrm{pv,min}}} \, , \tag{3.14}$$

in which Y_{pv} is given as a linear combination of weighted species mass fraction,

$$Y_{\mathrm{pv}} = \sum_k b_k Y_k \, , \tag{3.15}$$

where weights b_k are arbitrary chosen. As it will be seen in Section 3.4.1, in this work the carbon dioxide is the species chosen to be the reaction progress variable, $Y_{\mathrm{pv}} = Y_{\mathrm{CO_2}}$.

Fig. 3.2(b) presents the structure of a one-dimensional premixed methane-air flame. Three zones can be distinguished: a preheated zone (PZ), where the mixture is heated by diffusion, a reaction zone (RZ), where the chemical reactions take place, and an oxidation zone (OZ), in which the most of the chemical conversion is finalized.

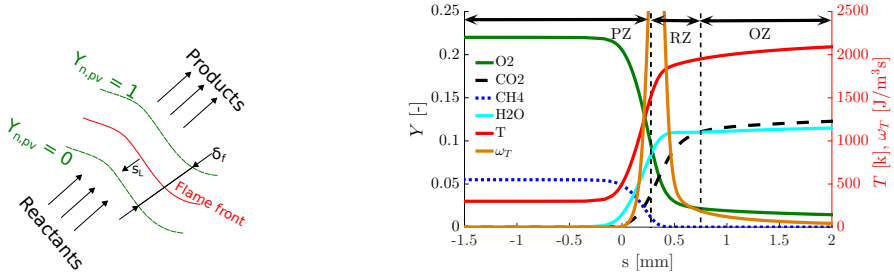

(a) (b)

Figure 3.2: (a) Basic representation of a premixed flame and (b) species distribution of a one-dimensional premixed methane-air flame with $\phi = 1$ and $T_u = 300\,\mathrm{K}$.

Two important parameters for the characterization of laminar premixed flames can be observed in Fig. 3.2(a): the laminar flame speed s_L and the flame thickness δ_f. The laminar flame speed, also known as burning velocity, is defined as the velocity in which the flame front moves through the unburnt gas. Besides that, the flame thickness corresponds to the spatial extent of the flame structure.

3.3 Turbulence-Chemistry Interaction

In reacting turbulent flow, the present turbulent structures interact with the flame front and may disturb it due to the wide range of scales existing. In order to exemplify this interaction, a scheme of a premixed flame is presented in Fig. 3.3 (a) for a laminar regime whereas in Fig 3.3 (b) a turbulent flame is shown.

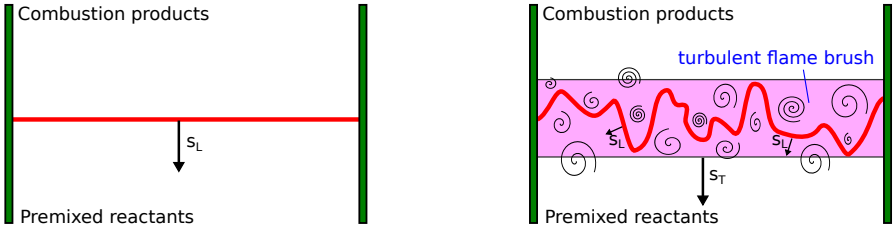

(a) (b)

Figure 3.3: Representation of a premixed flame in (a) laminar and (b) turbulent regime.

Analogous to the laminar flame speed, a turbulent flame speed s_T is indicated in this picture. The flame front is presented with its flame thickness in red and, as it can be seen, the instantaneous turbulent thickness is similar to the laminar case. On the other hand, the corresponding time averaged turbulent flame thickness, illustrated by the bright colored area is greater than for the laminar case. This time averaged value for turbulent flames is a characteristic parameter for these cases and is referred to as flame brush.

Peter [107] presented a diagram, shown in Fig. 3.4, for classifying the different turbulent regimes that can be found for premixed flames. This diagram is based on the integral

length scale l_t, flame thickness, laminar flame speed and on the velocity fluctuation magnitude u_{rms}.

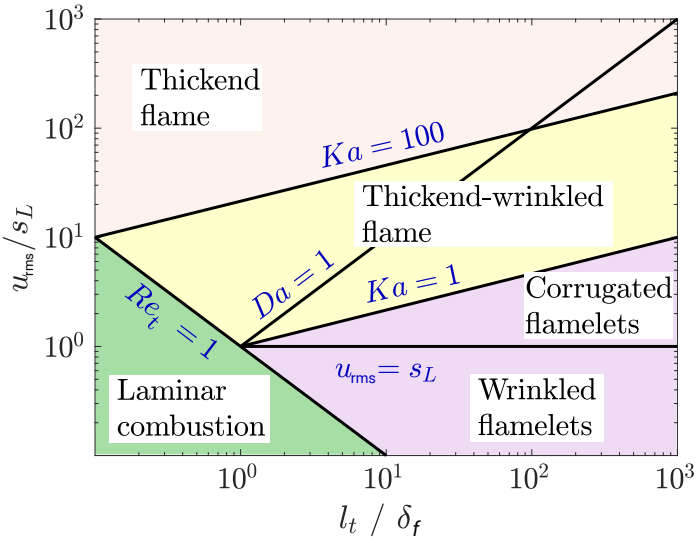

Figure 3.4: Classical turbulent combustion regime diagram (Peters [107]).

In order to classify the different regimes, three nondimensional parameter are used:

- Damköler number Da, which corresponds to the largest eddies, is defined as the ratio of the integral time scale τ_t to the chemical time scale τ_c

$$Da = \frac{\tau_t}{\tau_c} = \frac{l_t/u_{\text{rms}}}{\delta_f/s_L} \,, \tag{3.16}$$

- Karlovitz number Ka, which represents the smallest eddies (Kolmogorov scale), is calculate as the ratio of the chemical time scale τ_c to the Kolmogorov time scaleτ_K

$$Ka = \frac{\tau_c}{\tau_K} = \left(\frac{u_{\text{rms}}}{s_L}\right)^{3/2} \left(\frac{l_t}{\delta_f}\right)^{-1/2} \,, \tag{3.17}$$

- Turbulent Reynolds number is expressed as

$$Re_t = \frac{u_{\text{rms}}\, l_t}{v} = \left(\frac{l_t}{\delta_f}\right) \left(\frac{u_{\text{rms}}}{s_L}\right) \,. \tag{3.18}$$

Depending on the above nondimensional parameters, four basic different regimes can be observed within the diagram. A laminar combustion zone is identified for $Re_t < 1$, where no turbulence-flame interaction takes place. Then, in the region between $Re_t > 1$ and $Ka < 1$ the flamelet regime is found. In this region, because $Da > 1$, the chemical time scale is lower than the turbulent time scale. Moreover, the chemical reactions are not disturbed by turbulence because the flame is thin. According to u_{rms}/s_L, this regime is subdivided into wrinkled flamelet regime ($u_{\text{rms}} < s_L$) or corrugated flamelet regime

($u_{\text{rms}} > s_L$). A third region called thickened-wrinkled flame zone can be seen in the diagram for $1 < Ka < 100$. In this region the Kolmogorov scale is smaller than the flame thickness but it is larger than the reaction zone. Thus, the turbulent eddies may modify the preheated mixture but not the reaction zone. Finally, the region for $Ka \geq 100$ is called thickened flame or well stirred reactor zone. In this regime the chemical time scales are longer than the integral time scales of the flow and for this reason, the turbulent structures can strongly interact with the chemical reaction.

3.4 Combustion Modeling

The complete and explicit description of all chemical reactions in a combustion system involves a large number of species. For example, according to the work of Smith et al. [126], in which the GRI3.0 mechanism was employed, the combustion of methane/air mixture consists of 325 reactions with 53 species. Thus, the computation of all detailed reaction mechanisms in either DNS or LES framework for turbulent flows in complex geometries, as in this work, is not feasible due to the large range of time scales involved.

To overcome the above mentioned problem, simplified chemical kinetics schemes are commonly used. In this work the reduction strategy based on the tabulation of precomputed thermochemical states is employed. In this preprocessing step, the results are stored in a look-up table and are mapped according to one or more controlling variables. Therefore, the number of equations to be solved is significantly reduced by using this method as only transport equations for the controlling variables have to be computed. Besides that, for the production of the chemical database in this preprocessing, the detailed chemical mechanisms can be applied.

Within the tabulated technique, the approach called *Flamelet Generated Manifold* (FGM) is the one chosen here. This strategy is based on the assumption that the multi-dimensional turbulent flames can be divided into a large amount of one-dimensional laminar flames or flamelets, which have the same flame structure as the precomputed flames [143, 46]. This work uses the FGM variant implemented by Künne [78] and Ketelheun [71]. This approach was successfully validated and applied in several simulations of combustion systems of industrial size ([77], [12] and [11]) and will be outlined in the section below.

3.4.1 Chemistry Reduction Using Flamelet Generated Manifolds

In this strategy, the unity Lewis number $Le_k = Le = 1$ is assumed in the preprocessing step, in which the chemical database is produced. This assumption results in equal diffusion coefficients for all species $\mathcal{D}_k = \mathcal{D}$. Consequently, the combustion system becomes simpler and the mixture fraction and enthalpy do not vary along a flamelet. As pointed out in Künne [78], the discrepancies due to this assumption are acceptable for turbulent methane/air combustion.

According to Ketelheun [71], the generation of the chemical database is realized by computing a one-dimensional flame with detailed chemistry using the CHEM1D [3] code. As a reaction mechanism, the GRI3.0 [126] reaction scheme with 53 species involved in 325 elementary reactions is used.

Fig. 3.5(a) depicts the three-dimensional manifold utilized in this work with a cut for $\phi = 1$. The first dimension in this plot corresponds to the progress variable Y_{PV}, Eq. (3.15), which describes the progress of the mixture from unburnt to burnt. The second controlling variable is the mixture fraction Z, which is not directly indicated in the picture but it is expressed in terms of equivalence ratio ϕ, as in Eq. (3.12). This variable describes the transition of lean to rich mixture. It is commonly employed in order to include variable mixture occurring in nonpremixed combustion. Moreover, it is also necessary for simulating regions in which the mixture fraction varies. The last controlling variable is the enthalpy h, shown in gray-shading in this picture. It is required for computing heat losses in a nonadiabatic combustion as, for example, in technical applications involving walls. Additionally, the chemical source are also plotted in this picture. As it can be seen, this variable only has significant values in the direction of the progress variable where the reaction zone occurs. Furthermore, its maximum is close to the stoichiometric condition $\phi = 1$ and decreases in the directions of the lean and rich mixture.

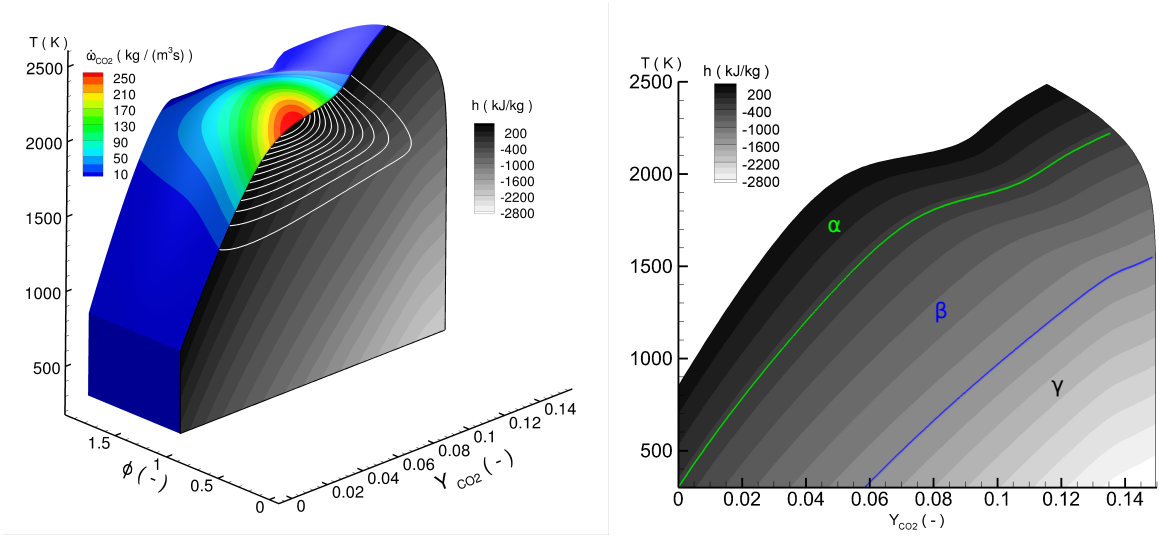

(a) (b)

Figure 3.5: Visualization of the applied three-dimensional table. (a) Complete representation with a cut for $\phi = 1$ and overlapped CO_2 source term $\dot{\omega}_{CO_2}$. (b) Slice for $\phi = 1$ with three indicated areas α) adiabatic, β) burner stabilized and γ) extrapolated.

The choice of the controlling variables necessary to describe the progress of the reactions depends on the phenomenon to be studied. As a progress variable, the mass fraction of CO_2, Y_{CO_2} is employed in this work, $Y_{\mathrm{PV}} = Y_{CO_2}$. According to Künne [78] and Jesch [59], choosing Y_{CO_2} as the progress variable Y_{PV} is a reasonable compromise between accuracy and affordable computational costs.

The preprocessed three-dimensional table is a result of many two-dimensional tables (or slices) with constant equivalence ratios. Each of these slices describes a thermochemical

condition depending on the enthalpy and on the progress variable. Such two-dimensional table is presented for $\phi = 1$ in Fig. 3.5 (b). This slice consists of three areas, which are generated from the flamelets with constant enthalpy level ($Le = 1$). As mentioned above, these flamelets are computed with the one-dimensional solver CHEM1D [3] and using the GRI3.0 [126] reaction scheme. The three areas indicated in this picture are: α) adiabatic, β) burner stabilized and γ) extrapolated zones. The first zone covers adiabatic premixed flamelets with different unburnt temperatures from 300 K to 850 K. Since the temperature can not be lowed below a certain unburnt level, the enthalpy has to be reduced in another way. For this aim, the burner-stabilized flamelets are used in zone β). They are computed by calculating one-dimensional flames stabilized above a porous burner, where the enthalpy level is lowered. Then, the unburnt gas velocity is changed for obtaining different enthalpy levels. In region γ), the flamelets are determined by extrapolation. In this area the enthalpy presents the lowest values and no chemical reactions take place. This procedure is repeated for all required equivalence ratios and then saved in the table. Further information about the table generation strategy can be found in Ketelheun [71].

In conclusion, the complete thermochemical conditions are determined by three controlling variables, which are transported in the LES solver. All other required variables, as chemical source term, temperature, viscosity and density, are obtained by looking up the values stored in the table ($\tilde{\varphi} = \tilde{\varphi}(\tilde{Z},\tilde{Y}_{CO_2},\tilde{h})$) for every step of the simulation.

3.4.2 FGM Coupling with LES

By employing commonly computational grids used for LES of complex geometries, the flame cannot be resolved, but its effect on the subgrid-scales should be taken into account. Besides that, as discussed in Section 3.4.1, in the FGM context, the dependent scalars are retrieved from the precomputed chemistry table by using the Favre filtered value of the mixture fraction $\tilde{Z}$. Furthermore, as already known, a filtered variable does not have any information about its corresponding subgrid values. Additionally, the thermochemical properties of the combustion products in the chemistry table are not linearly related and a correct determination of the thermochemical state cannot be obtained by using only LES filtered values of the controlling variable [11]

$$\widetilde{\phi(Z)} \neq \phi(\tilde{Z}) \; . \tag{3.19}$$

Therefore, the subgrid distribution should be taken into account and *Probability Density Function* (PDF) can be used to describe it. This is done in this work by using the Eulerian Monte Carlo stochastic field method. This method deals with a joint scalar subgrid PDF transport equation and is presented in the following section.

3.5 Stochastic Field Method for Modeling Turbulent Combustion

Following Avdic et al. [11], the species ϕ_α, for a location x_i and time t, can be described by a one-point fine-grained probability density function $\mathcal{P}$ as

$$\mathcal{P}_\alpha(\psi_\alpha; x_i,t) = \delta(\psi_\alpha - \phi_\alpha(x_i,t)) \ , \tag{3.20}$$

where δ is the Dirac delta function and ψ represents a sample or composition space of the species ϕ_α. Furthermore, the joint PDF $\mathcal{F}(\psi; x_i,t)$ for the complete set of species involved in the considered combustion process can be determined by multiplying all the marginal probabilities $\mathcal{P}_\alpha$,

$$\mathcal{F}(\psi; x_i,t) = \prod_{\alpha=1}^{N_\alpha} \delta(\psi_\alpha - \phi_\alpha(x_i,t)) \ . \tag{3.21}$$

$\mathcal{F}(\psi; x_i,t)$ describes the probability that a certain species state ϕ_α can be found in the sample space between ψ_α and $\psi_\alpha + \mathrm{d}\psi_\alpha$.

3.5.1 Filtered Probability Density Function

In the context of LES, the density-weighted Favre filtering with the filter function $\mathcal{G}$ should be applied. Therefore, by applying Eqs. (2.39) and (2.42) to the joint PDF $\mathcal{F}(\psi; x_i,t)$, it yields the density weighted (or filtered) joint subgrid probability density function $\tilde{\mathcal{P}}_{sgs}(\psi)$

$$\tilde{\mathcal{P}}_{sgs}(\psi) = \int_V \frac{\rho(x_i - x_i')}{\bar{\rho}} \mathcal{F}(x_i') \mathcal{G}(x_i - x_i', \Delta(x_i)) dx_i' \ . \tag{3.22}$$

The first statistical moment of the $\tilde{\mathcal{P}}_{sgs}(\psi)$ represents the filtered mean value $\widetilde{\phi}_\alpha$, given as

$$\widetilde{\phi}_\alpha = \int_{-\infty}^{\infty} \int_V \frac{\rho(x_i - x_i')}{\bar{\rho}} \psi_\alpha \mathcal{F}(x_i') \mathcal{G}(x_i - x_i', \Delta(x_i)) \mathrm{d}x_i' \mathrm{d}\psi_\alpha \ . \tag{3.23}$$

Besides that, the second moment corresponds to the subgrid variance $\widetilde{\phi^2}_{\alpha,\mathrm{sgs}}$, obtained as

$$\widetilde{\phi^2}_{\alpha,\mathrm{sgs}} = \int_{-\infty}^{\infty} \int_V \frac{\rho(x_i - x_i')}{\bar{\rho}} \psi_\alpha^2 \mathcal{F}(x_i') \mathcal{G}(x_i - x_i', \Delta(x_i)) \mathrm{d}x_i' \mathrm{d}\psi_\alpha - \widetilde{\phi_\alpha}^2 \ . \tag{3.24}$$

Gao and O'Brien [47] derived an exact evolution equation for $\tilde{\mathcal{P}}_{sgs}(\psi)$. By assuming equal diffusivity and following previous works by Mustata et al. [99], Jones and Navarro-Martinez [62] and Avdic et al. [11] for modeling the micro-mixing term, the PDF transport

equation is expressed as follows

$$\frac{\partial \bar{\rho}\tilde{\mathcal{P}}_{sgs}(\psi)}{\partial t} + \frac{\partial}{\partial x_i}\left(\bar{\rho}\,\tilde{u}_i\tilde{\mathcal{P}}_{sgs}(\psi)\right) - \sum_{\alpha=1}^{N_\alpha}\frac{\partial}{\partial \psi_\alpha}\left(\mathcal{Q}_\alpha\tilde{\mathcal{P}}_{sgs}(\psi)\right) = \frac{\partial}{\partial x_i}\left[\left(\frac{\bar{\mu}}{Sc} + \frac{\mu_t}{Sc_t}\right)\frac{\partial\tilde{\mathcal{P}}_{sgs}(\psi)}{\partial x_i}\right] - \frac{\bar{\rho}}{\tau_\phi}\sum_{\alpha=1}^{N_\alpha}\left[\left(\psi_\alpha - \bar{\phi}_\alpha\right)\tilde{\mathcal{P}}_{sgs}(\psi)\right] , \tag{3.25}$$

where $\mathcal{Q}_\alpha$ is the source term depending on the considered controlling variable and the subgrid mixing time scale τ_ϕ is calculated by using the micro-mixing constant C_Ω as

$$\tau_\phi^{-1} = C_\Omega\frac{\overline{v} + v_t}{\Delta^2} . \tag{3.26}$$

As suggested in Avdic et al. [11], in this work it is assumed $C_\Omega = 2$.

3.5.2 Eulerian Monte Carlo Stochastic Field Method

The Monte Carlo formulation based on the *Eulerian Stochastic Field* (ESF) method proposed by Valino [135] and Jones and Navarro-Martinez [63] is employed in order to solve the PDF transport equation Eq. (3.25). In this formulation, the density weighted PDF $\tilde{\mathcal{P}}_{sgs}(\psi)$ is expressed in terms of an ensemble of N stochastic fields $\xi_\alpha(x_i,t) = [\xi_\alpha^1, \cdots, \xi_\alpha^N]$ as

$$\tilde{\mathcal{P}}_{sgs}(\psi; x_i,t) = \frac{1}{N}\sum_{n=1}^{N}\prod_{\alpha=1}^{N_\alpha}\delta(\psi_\alpha - \xi_\alpha^n(x_i,t)) . \tag{3.27}$$

Following this formulation, the transport equation for the N stochastic fields is given as ([135], [63], [11])

$$\mathrm{d}(\bar{\rho}\xi_\alpha^n) = -\frac{\partial}{\partial x_j}(\bar{\rho}\,\tilde{u}_j\xi_\alpha^n)\mathrm{d}t + \frac{\partial}{\partial x_j}\left[\left(\frac{\bar{\mu}}{Sc} + \frac{\mu_t}{Sc_t}\right)\frac{\partial\xi_\alpha^n}{\partial x_j}\right]\mathrm{d}t + \mathcal{Q}_\alpha^n\mathrm{d}t - \frac{\bar{\rho}}{2\tau_\phi}\left(\xi_\alpha^n - \widetilde{\phi}_\alpha\right)\mathrm{d}t + \sqrt{2\bar{\rho}^{\,2}\frac{\mu_t}{Sc_t}}\frac{\partial\xi_\alpha^n}{\partial x_j}\mathrm{d}\mathrm{W}_j^n , \tag{3.28}$$

where the last term of this equation represents the random stochastic component and the variable dW_j^n in this term denotes increments of a vector Wiener process, which is independent of the spatial coordinates and is different for each stochastic field.

Following Avdic et al. [11, 12], the ESF method is adopted in conjunction with the FGM chemistry reduction strategy, given in Section 3.4.1. Thus, Eq. (3.28) is solved for N stochastic fields for each of the controlling variables $\Phi = [Y_{CO2},h,Z]$. The source terms of the transport equations for $\xi^n_{Y_{\mathrm{CO_2}}}$, ξ_h^n and ξ_Z^n are given by

$$\mathcal{Q}_{Y_{\mathrm{CO_2}}} = \dot{\omega}, \qquad \mathcal{Q}_h = S_{\mathrm{rad}}, \qquad \mathcal{Q}_Z = 0, \tag{3.29}$$

where $\dot{\omega}$ corresponds the production or the consumption of CO_2 due to the chemical reaction and S_{rad} describes to the augmentation or attenuation due to radiative heat transfer.

The first and the second moments, representing the filtered mean and subgrid variance of ϕ_α, can be determined as

$$\widetilde{\phi}_\alpha = \frac{1}{N}\sum_{n=1}^{N}\int_{\psi_\alpha=-\infty}^{\psi_\alpha=\infty}\psi_\alpha\delta(\psi_\alpha-\xi_\alpha^n)\mathrm{d}\psi_\alpha = \frac{1}{N}\sum_{n=1}^{N}\xi_\alpha^n\ , \tag{3.30}$$

$$\widetilde{\phi^2_{\alpha,\text{sgs}}} = \frac{1}{N}\sum_{n=1}^{N}\int_{\psi_\alpha=-\infty}^{\psi_\alpha=\infty}\psi_\alpha^2\delta(\psi_\alpha-\xi_\alpha^n)\mathrm{d}\psi_\alpha - \widetilde{\phi_\alpha}^2 = \frac{1}{N}\sum_{n=1}^{N}\left(\xi_\alpha^n\right)^2 - \widetilde{\phi_\alpha}^2\ . \tag{3.31}$$

The greater the number of stochastic fields, the more accurate is the PDF distribution and, consequently, the calculated first moments. On the other hand, a greater number of stochastic fields leads to an increase in computational costs. As reported by Haworth and Pope [55], between 10 and 30 fields are commonly used for LES modeling studies.

3.5.3 Summary of the Solved Equations

By using the FGM chemistry reduction strategy and the ESF for the coupling with LES, besides the continuity and momentum equation, N stochastic equations for each controlling variable need to be solved. As discussed in Sec. 3.4.1, the controlling variables are the progress variable, mixture fraction and enthalpy. The corresponding stochastic differential equations are

$$\begin{aligned}\mathrm{d}(\bar{\rho}\xi_{\text{PV}}^n) = &-\frac{\partial}{\partial x_j}(\bar{\rho}\,\widetilde{u}_j\xi_{\text{PV}}^n)\mathrm{d}t + \frac{\partial}{\partial x_j}\left[\left(\frac{\bar{\mu}}{Sc}+\frac{\mu_t}{Sc_t}\right)\frac{\partial\xi_{\text{PV}}^n}{\partial x_j}\right]\mathrm{d}t\\ &+\dot{\omega}_{\text{PV}}^n\mathrm{d}t - \frac{\bar{\rho}}{2\tau_\phi}\left(\xi_{\text{PV}}^n-\widetilde{\phi}_{\text{PV}}\right)\mathrm{d}t + \sqrt{2\bar{\rho}^{\,2}\frac{\mu_t}{Sc_t}}\frac{\partial\xi_{\text{PV}}^n}{\partial x_j}\mathrm{dW}_j^n \quad \text{for} \quad n=1,\cdots,N\ ,\end{aligned} \tag{3.32}$$

$$\begin{aligned}\mathrm{d}(\bar{\rho}\xi_Z^n) = &-\frac{\partial}{\partial x_j}(\bar{\rho}\,\widetilde{u}_j\xi_Z^n)\mathrm{d}t + \frac{\partial}{\partial x_j}\left[\left(\frac{\bar{\mu}}{Sc}+\frac{\mu_t}{Sc_t}\right)\frac{\partial\xi_Z^n}{\partial x_j}\right]\mathrm{d}t\\ &-\frac{\bar{\rho}}{2\tau_\phi}\left(\xi_Z^n-\widetilde{\phi}_Z\right)\mathrm{d}t + \sqrt{2\bar{\rho}^{\,2}\frac{\mu_t}{Sc_t}}\frac{\partial\xi_Z^n}{\partial x_j}\mathrm{dW}_j^n \quad \text{for} \quad n=1,\cdots,N\ ,\end{aligned} \tag{3.33}$$

$$\mathrm{d}(\bar{\rho}\xi_h^n) = -\frac{\partial}{\partial x_j}(\bar{\rho}\,\widetilde{u}_j\xi_h^n)\mathrm{d}t + \frac{\partial}{\partial x_j}\left[\left(\frac{\bar{\mu}}{Sc} + \frac{\mu_t}{Sc_t}\right)\frac{\partial \xi_h^n}{\partial x_j}\right]\mathrm{d}t + \overline{S}_\mathrm{r}\mathrm{d}t$$
$$- \frac{\bar{\rho}}{2\tau_\phi}\left(\xi_h^n - \widetilde{\phi}_h\right)\mathrm{d}t + \sqrt{2\bar{\rho}^{\,2}\frac{\mu_t}{Sc_t}}\frac{\partial \xi_h^n}{\partial x_j}\mathrm{d}\mathrm{W}_j^n \quad \text{for} \quad n = 1, \cdots, N\,. \tag{3.34}$$

3.6 Summary

In this chapter a general description of turbulent reactive flows and modeling approaches were presented. First, the fundamentals of chemical reactions and kinetics were given. Then, the basic flame modes found in combustion systems, diffusion and premixed flames, were addressed. This section was followed by a brief overview of turbulence-chemistry interaction.

In the remaining sections the modeling approaches employed in this work were outlined. Here, the chemistry reduction by tabulation with the FGM method was presented. Furthermore, in order to couple the combustion solver with LES, a model called ESF is used in conjunction with FGM. Thus, in the last section the ESF method was introduced and its formulation was presented.

Chapter 4

Numerical Methods

Analytical solutions for the governing equations given in Section 2.1.5 only exist for very simplified cases. Thus, for the problems studied here, which involve combustion processes with large temperature gradients in 3D geometries, numerical methods are necessary.

In this work, the academic CFD code FASTEST (Flow Analysis by Solving Transport Equations Simulating Turbulence) is used and further developed. This code is used by several research institutions for numerous applications in the field of CFD. Originally, FASTEST was developed for simulating incompressible flows in the context of RANS [104]. At the Institute of Energy and Power Plant Technology at the TU Darmstadt, this code has been extended to efficiently compute chemically reacting flows in complex geometries for RANS and LES. This version is based on the low mach number approximation implemented by Hahn [53] and Olbricht [101]. As it will be seen in details in the following sections, the solution algorithm is based on finite volume method and the pressure-correction scheme is done with the fractional step projection method proposed by Chorin [27].

In the next section, the general solution procedure is outlined, where the spatial and temporal discretization schemes, the algorithm for pressure-correction and the boundary conditions are presented. After that, in Section 4.2, the numerical methods for solving the equations for the EFS method are briefly described. Moreover, in the next two sections, the overall solution procedure and details about the parallelization in FASTEST are shown.

4.1 General Solution Procedure

The governing equations shown in Chapter 2 together with the boundary conditions have to be discretized in order to be solved numerically. The procedure begins with the spatial discretization, followed by the temporal discretization, pressure correction and, finally, boundary conditions setup.

4.1.1 Domain Discretization

As already mentioned, the in-house code FASTEST is used in this work. It uses a block structured mesh to describe the domain. In this strategy, the computational domain consists of one or more computational grids made of arbitrary shaped hexahedrons, as illustrated in Fig. 4.1. This gives flexibility in the design of the mesh and requires less memory when compared to unstructured grids. For local refinements, O-grid structures can be employed. Ghost cells are used to build the connectivities between the blocks. Moreover, the commercial software ANSYS ICEM CFD [6] is used for generating the meshes.

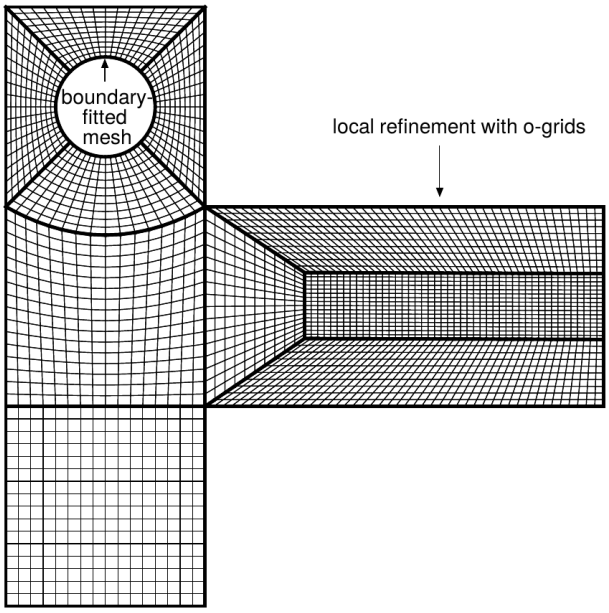

Figure 4.1: Example of a block structured grid including a local refinement. Figure adapted from Künne [78].

FASTEST employs the finite volume method for the spatial discretization and the following sections present the application of this method for the governing equations shown in Section 2.1.5.

4.1.1.1 Spatial Discretization of the Transport Equations

In the finite volume method the domain is divided into a finite number of control volumes and the conservation equations are applied to each control volume. The process of discretization by applying this method will be demonstrated for a generic conservation equation for the quantity φ,

$$\frac{\partial \rho\varphi}{\partial t} + \frac{\partial}{\partial x_i}(\rho u_i \varphi) = \frac{\partial}{\partial x_i}\left(\Gamma_\varphi \frac{\partial \varphi}{\partial x_i}\right) + w_\varphi \ , \tag{4.1}$$

where Γ_φ and w_φ represent the diffusion coefficient and the source term, respectively.

Firstly, Eq. (4.1) is integrated over a control volume V ,

$$\int_V \frac{\partial \rho\varphi}{\partial t}\,\mathrm{d}V + \int_V \frac{\partial}{\partial x_i}(\rho u_i \varphi)\,\mathrm{d}V = \int_V \frac{\partial}{\partial x_i}\left(\Gamma_\varphi \frac{\partial \varphi}{\partial x_i}\right)\mathrm{d}V + \int_V w_\varphi\,\mathrm{d}V\ . \tag{4.2}$$

By applying the Gauss's theorem [45], the volume integrals of the convective and the diffusive terms can be transformed into surface integrals. Thus, Eq. (4.2) can be written as

$$\int_V \frac{\partial \rho\varphi}{\partial t}\,\mathrm{d}V + \int_S \rho u_i \varphi n_i\,\mathrm{d}S = \int_S \left(\Gamma_\varphi \frac{\partial \varphi}{\partial x_i}\right) n_i\,\mathrm{d}S + \int_V w_\varphi\,\mathrm{d}V\ , \tag{4.3}$$

where S is the surface surrounding the control volume and n_i denotes the unity vector normal to S and directed outwards. Remembering the control volumes used in this work are hexahedron, the surface integrals can be calculated as a sum of the integrals over the six faces,

$$\int_V \frac{\partial \rho\varphi}{\partial t}\,\mathrm{d}V + \sum_c \int_{Sc} \rho u_i \varphi n_i\,\mathrm{d}Sc = \sum_c \int_{Sc} \left(\Gamma_\varphi \frac{\partial \varphi}{\partial x_i}\right) n_i\,\mathrm{d}Sc + \int_V w_\varphi\,\mathrm{d}V\ , \tag{4.4}$$

where c represents the considered face. For instance, in a two dimensional configuration c = n, e, s, w with n, e, s, w being the north, east, south and west face, respectively. In Fig. 4.2(b) a typical two dimensional control volume is shown.

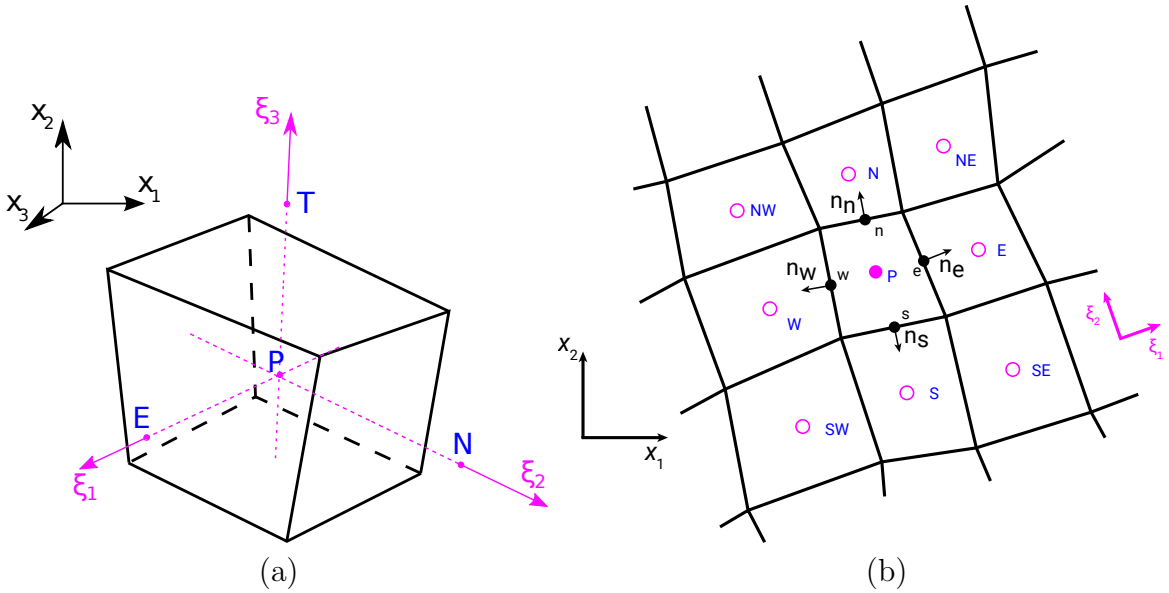

Figure 4.2: (a) An arbitrary control volume P showing the global $(\mathrm{x}_1, \mathrm{x}_2, \mathrm{x}_3)$ and the local (ξ_1, ξ_2, ξ_3) coordinate systems, (b) two dimensional view for $\xi_3 = 0$ of this control volume and its neighbors.

The second-order accurate approximation is used to replace the volume and surface integrals. Thus, Eq. (4.4) takes the form:

$$\frac{\partial \rho\varphi}{\partial t}\Delta V + \sum_c \rho u_i \varphi \; n_i A_c = \sum_c \left(\frac{\Gamma_\varphi \partial \varphi}{\partial x_i} \right) n_i A_c + w_\varphi \Delta V \; , \tag{4.5}$$

where ΔV corresponds to the volume of the control volume and A_c the area of the face c.

It should be noted that for the convective and diffusive flux terms in Eq. (4.5), the variables and gradients have to be known at the center of the faces, and not only in the center of the control volume. Thus, a reconstruction of cell centered variables at the cell interface locations should be done. For this propose, a local cell based coordinate system (ξ_1, ξ_2, ξ_2) is introduced, as shown in Figs. 4.2(a) and (b). As seen before, the governing equations are written based on the Cartesian system x_1,x_2,x_3 and a transformation is then required between these two systems. This transformation is used in the computation of the convective and diffusive flux terms, which is described in the subsequent Sections 4.1.2 and 4.1.3.

4.1.2 Convective Fluxes

In FASTEST the convective fluxes are approximated by using a scheme based on the *Central Difference Scheme* (CDS) for the momentum conservation and the *Total Variation Diminishing* (TVD) for scalar transport equations.

For the momentum equation the multi-linear interpolation scheme (MULI) proposed in Lehnhäuser and Schäfer [83] is used to approximate the variables at the center of the cell face. It is a second order formulation and is based on the Taylor series expansion. According to Lehnhäuser and Schäfer [83], for rectangular grid cells, this approximation is equivalent to the standard CDS. Besides that, this formulation requires only slightly more computational costs than the classical CDS. By employing this scheme, the value of an arbitrary variable on the east face is given as

$$\varphi_e = w_E \varphi_E + (1 - w_E)\varphi_P + w_{NS}(\varphi_N - \varphi_S) + w_{TB}(\varphi_T - \varphi_B) \; , \tag{4.6}$$

with the interpolation weights w_E, w_{NS} and w_{TB}

$$\begin{aligned} w_E &= \frac{x_{i,P} - x_{i,e}}{\mathcal{J}_e} \psi_e^{1i} \; , \\ w_{NS} &= \frac{x_{i,P} - x_{i,e}}{\mathcal{J}_e} \psi_e^{2i} \; , \\ w_{TB} &= \frac{x_{i,P} - x_{i,e}}{\mathcal{J}_e} \psi_e^{3i} \; , \end{aligned} \tag{4.7}$$

where

$$\begin{aligned} \psi_e^{1i} &= \epsilon_{ikl}[(x_{k,N} - x_{k,S})(x_{l,T} - x_{l,B})] \,, \\ \psi_e^{2i} &= \epsilon_{ikl}[(x_{k,T} - x_{k,B})(x_{l,E} - x_{l,P})] \,, \\ \psi_e^{3i} &= \epsilon_{ikl}[(x_{k,E} - x_{k,P})(x_{l,N} - x_{l,S})] \,, \end{aligned} \tag{4.8}$$

$$\mathcal{J}_e = (x_{i,E} - x_{i,P})\psi_e^{1i} \,, \tag{4.9}$$

and ϵ_{ikl} being the Levi-Civita symbol.

CDS does not present numerical dissipation and for this reason oscillations may be produced leading to unphysical values. Therefore, the TVD scheme is used for the scalar transport equations to assure boundedness of the transported variables and to obtain a stable solution. This work employs the TVD implementations of Kempf [68] and the interpolation slope of the MULI scheme is limited using CHARM limiter of Zhou et al. [149]. If one considers Fig. 4.3, the value of an arbitrary variable on the cell face (e) is calculated from its downwind (D) and upwind (U) neighbors as

$$\varphi_e = \varphi_U + \frac{|x_{i,e} - x_{i,U}|}{|x_{i,D} - x_{i,U}|} B(r)(\varphi_U - \varphi_{UU}) \,, \tag{4.10}$$

with the flux limiter function $B(r)$

$$B(r) = \begin{cases} \frac{r(3r+1)}{(r+1)^2} & \text{if } r > 0 \,, \\ 0 & \text{if } r \leq 0 \,, \end{cases} \tag{4.11}$$

where the r is the gradient ratio given as

$$r = \frac{|x_{i,U} - x_{i,UU|}}{|x_{i,D} - x_{i,U|}} \cdot \frac{\varphi_D - \varphi_U}{\varphi_U - \varphi_{UU}} \,. \tag{4.12}$$

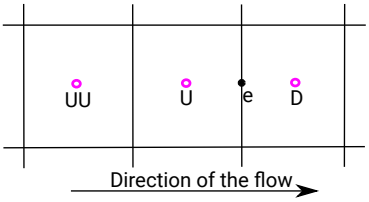

Figure 4.3: Example of a control volume illustrating the considered face e and its neighbors for calculating the convection fluxes with the TVD scheme.

As discussed in Künne [78], if the gradient ratio is close to one, for example in the case of a well resolved gradient of φ, this scheme leads to the linear upwind scheme of second order. On the other hand, if the gradient is sharp, r tends to zero or infinite and as a result, the solution converges nonlinearly towards an upwind scheme of first order.

FASTEST uses nonstaggered grids and by applying a CDS approximation for the mass flux in the Navier-stokes equation Eq. (2.27) the decoupling of the pressure and velocity field can occur. Therefore, in order to avoid unphysical oscillations that may result, the

Rhie and Chow [114] interpolation is additionally applied. This procedure, necessary for collocated grids, can be seen as a correction which is proportional to the difference between the pressure gradient at the face and the interpolated pressure gradient at the face.

4.1.3 Diffusive Fluxes

For the diffusive fluxes, not only the value of the variable on the cell face is necessary but also its derivative in this position is required. The derivatives need to be transformed between the global and local coordinate systems [45]:

$$\frac{\partial \varphi}{\partial x_i} = \frac{\beta^{ij}}{\mathcal{J}} \frac{\partial \varphi}{\partial \xi_i} \,, \tag{4.13}$$

where β^{ij} corresponds to the cofactor of $\partial x_i / \partial \xi_j$ in the Jacobian $\mathcal{J}$

$$\mathcal{J} = \det \left(\frac{\partial x_i}{\partial \xi_j} \right) \,. \tag{4.14}$$

By considering Fig. 4.2 and according to Lehnhäuser [82], the computation of derivatives can be done as:

$$\left. \frac{\partial \varphi}{\partial x_i} \right|_e = \frac{\psi^{ji}_{e,gr}}{\mathcal{J}_{e,gr}} \varphi^j_{e,gr} \,, \tag{4.15}$$

with

$$\begin{aligned}
\varphi^1_{e,gr} &= (\varphi_E - \varphi_P) \,, \\
\varphi^2_{e,gr} &= (\varphi_N - \varphi_S + \varphi_{NE} - \varphi_{SE}) \,, \\
\varphi^3_{e,gr} &= (\varphi_T - \varphi_B + \varphi_{TE} - \varphi_{BE}) \,,
\end{aligned} \tag{4.16}$$

$$\begin{aligned}
\psi^{1i}_{e,gr} &= \epsilon_{ikl}((x_{k,N} - x_{k,S} + x_{k,NE} - x_{k,SE})(x_{l,T} - x_{l,B} + x_{l,TE} - x_{l,BE})) \,, \\
\psi^{2i}_{e,gr} &= \epsilon_{ikl}((x_{k,T} - x_{k,B} + x_{k,TE} - x_{k,BE})(x_{l,E} - x_{l,P})) \,, \\
\psi^{3i}_{e,gr} &= \epsilon_{ikl}((x_{k,E} - x_{k,P})(x_{l,N} - x_{l,S} + x_{l,NE} - x_{l,SE})) \,,
\end{aligned} \tag{4.17}$$

$$\mathcal{J}_{e,gr} = (x_{i,E} - x_{i,P}) \psi^{1i}_{e,gr} \,. \tag{4.18}$$

This approximation is analogous to the interpolation scheme in Lehnhäuser and Schäfer [83], shown in Section 4.1.2, and also leads to a second order approach.

4.1.4 Temporal Discretization

A temporal discretization should be applied to discretize the transient term in the generic conservation equation for the quantity φ, Eq. (4.1). This is done in this work with a second order low-storage Runge-Kutta scheme [144] which will be illustrated below.

For brevity, Eq.(4.1) can be rewritten as,

$$\frac{\partial \varphi_r}{\partial t} = R(\varphi_r) \ , \tag{4.19}$$

where $\varphi_r = \rho\varphi$ and $R(\varphi_r)$ represents all the spatially discretized terms on the right-hand side.

With the implemented Runge-Kutta scheme, the new values of φ_r are obtained from the old ones following the expressions:

$$\begin{aligned} \varphi_r^{RK,1} &= \varphi_r^n + \alpha_{RK,1}\Delta t \ R(\varphi_r^n) \ , \\ \varphi_r^{RK,2} &= \varphi_r^n + \alpha_{RK,2}\Delta t \ R(\varphi_r^{RK,1}) \ , \\ \varphi_r^{n+1} &= \varphi_r^n + \Delta t \ R(\varphi_r^{RK,2}) \ . \end{aligned} \tag{4.20}$$

where Δt is the time step interval, φ_r^n corresponds to the old values of φ_r and φ_r^{n+1} denotes the new values. Besides that, the coefficients α_{RK} are

$$\alpha_{RK,1} = \frac{1}{3} \ , \qquad\qquad \alpha_{RK,2} = \frac{1}{2} \ . \tag{4.21}$$

As it can be noted in Eqs. (4.20), only these two arrays (φ_r^n, φ_r^{n+1}) have to be stored.

The choice of the time step Δt is done based on two important parameters, the Courant number $\mathcal{C}$ [39] and the diffusion number D:

$$\mathcal{C} = \frac{u\Delta t}{\Delta x} \ , \qquad\qquad \mathsf{D} = \frac{\mathcal{D}_{k,mix}\Delta t}{\Delta x^2} \ , \tag{4.22}$$

in which Δx is the grid size and $\mathcal{D}_{k,mix}$ corresponds to the diffusion coefficient of the mixture. As already discussed in Section 2.1.3, the same diffusion coefficient is assumed for all species ($\mathcal{D}_{k,mix} = \mathcal{D}$). These key numbers should not exceed a limit to keep the calculation stable. As derived in Künne [78], for the implemented solver, the stability limits are: $|\mathcal{C}| < 1.73$ and $D \leq 0.63$.

4.1.5 Pressure-velocity Coupling

According to Ferziger and Peric [45], for incompressible flows the solution of the Navier-Stokes equations is not straightforward because of the lack of an independent equation for the pressure, which is required to calculate the pressure gradient. For compressible flows the continuity equation is used to calculate the density and the pressure is obtained from the equation of state. For incompressible flows, the pressure field must be constructed in a way to satisfy the continuity equation. The so-called fractional step projection method proposed by Chorin [27] is the procedure used in FASTEST. This method is briefly presented in this section.

In the fist step, an estimated velocity field is calculated from Eq. (2.45) by using the explicit time integration,

$$\begin{aligned}(\overline{\rho}\ \widetilde{u}_j)^{*,RK,i} &= (\overline{\rho}\ \widetilde{u}_j)^n + \alpha_{RK,i}\Delta t\ R(\widetilde{u}_j^n) \\ &= (\overline{\rho}\ \widetilde{u}_j)^n + \alpha_{RK,i}\Delta t\ \left(C^{RK,i-1} + D^{RK,i-1} - \frac{\partial \overline{p}^{RK,i-1}}{\partial x_j}\right) ,\end{aligned} \tag{4.23}$$

where C and D are the convective and diffusive fluxes, respectively. This first estimation does not necessarily satisfy the conservation of mass and in order to satisfy it, a momentum correction $(\overline{\rho}\widetilde{u}_j)'$ is introduced

$$(\overline{\rho}\ \widetilde{u}_j)^{RK,i} = (\overline{\rho}\ \widetilde{u}_j)^{*,RK,i} + (\overline{\rho}\ \widetilde{u}_j)' \ . \tag{4.24}$$

Analogously, a pressure correction $\overline{p}'$ is defined as

$$\overline{p}^{RK,i} = \overline{p}^{RK,i-1} + \overline{p}' \ . \tag{4.25}$$

Substituting Eqs. (4.23) and (4.25) in Eq. (4.24) leads to

$$(\overline{\rho}\ \widetilde{u}_j)^{RK,i} = (\overline{\rho}\ \widetilde{u}_j)^n + \alpha_{RK,i}\Delta t\ \left(C^{RK,i-1} + D^{RK,i-1} - \frac{\partial \overline{p}^{RK,i-1}}{\partial x_j} - \frac{\partial \overline{p}'}{\partial x_j}\right) . \tag{4.26}$$

By subtracting Eq. (4.23) from Eq. (4.26) and applying Eq. (4.25), a relation between the momentum correction and the pressure correction is obtained

$$(\overline{\rho}\ \widetilde{u}_j)' = -\alpha_{RK,i}\Delta t \frac{\partial \overline{p}'}{\partial x_j} \ . \tag{4.27}$$

The correction given in Eq. (4.24) can be used in the continuity equation as

$$\frac{\partial \overline{\rho}}{\partial t} + \frac{\partial}{\partial x_j}\left(\overline{\rho}\widetilde{u}_j\right)^{*,RK,i} + \frac{\partial}{\partial x_j}(\overline{\rho}\ \widetilde{u}_j)' = 0 \ . \tag{4.28}$$

By replacing Eq. (4.27) in Eq. (4.28), it results in the final form of the Poisson-equation for the pressure correction

$$\frac{\partial}{\partial x_j}\frac{\partial \overline{p}'}{\partial x_j} = \frac{1}{\alpha_{RK,i}\Delta t}\left(\frac{\partial \overline{\rho}}{\partial t} + \frac{\partial}{\partial x_j}\left(\overline{\rho}\widetilde{u}_j\right)^{*,RK,i}\right) \ . \tag{4.29}$$

The equation above is then discretized with the techniques discussed in the previous sections resulting in an expression which relates the pressure correction and the mass

lack,

$$\sum_c \left(\frac{\partial \overline{p}'}{\partial x_j} n_i \right) A_c = \frac{1}{\alpha_{RK,i} \Delta t} \underbrace{\left(\left. \frac{\partial \overline{\rho}}{\partial t} \right|_c \Delta V + \sum_c (((\overline{\rho} \widetilde{u}_j)^{*,RK,i} \, n_j) \Big|_c A_c) \right)}_{\text{mass lack}} . \tag{4.30}$$

Considering all control volumes, the algebraic system $\mathbf{A}\mathbf{p}' = \mathbf{b}$ can be built. This system is solved in FASTEST with an iterative *Strongly Implicit Procedure* (SIP) proposed by Stone [132]. Details about this solver and its implementation in FASTEST can be found in Leister [84].

The fractional step projection method can be summarized in the following steps:

- Estimate the velocity fields:

$$(\overline{\rho} \, \widetilde{u}_j)^{*,RK,i} = (\overline{\rho} \, \widetilde{u}_j)^n + \alpha_{RK,i} \Delta t \; R(\widetilde{u}_j^n) \; . \tag{4.31}$$

- Calculate the pressure correction:

$$\sum_c \left(\frac{\partial \overline{p}'}{\partial x_j} n_i \right) A_c = \frac{1}{\alpha_{RK,i} \Delta t} \left(\left. \frac{\partial \overline{\rho}}{\partial t} \right|_c \Delta V + \sum_c (((\overline{\rho} \widetilde{u}_j)^{*,RK,i} \, n_j) \Big|_c A_c) \right) . \tag{4.32}$$

- Correct the velocity fields:

$$(\overline{\rho} \, \widetilde{u}_j)^{RK,i} = (\overline{\rho} \, \widetilde{u}_j)^{*,RK,i} - \alpha_{RK,i} \Delta t \frac{\partial \overline{p}'}{\partial x_j} \; . \tag{4.33}$$

- Update the pressure field:

$$\overline{p}^{RK,i} = \overline{p}^{RK,i-1} + \overline{p}' \; . \tag{4.34}$$

- Verify if the mass lack is smaller than a previously specified limit.

4.1.6 Boundary Conditions

In order to perform the computations, the boundary conditions should be given. The standard boundary conditions in FASTEST are:

- **Inlet**. At the inlet all the variables are given with Dirichlet condition.
- **Outlet**. For the outlet, the Neumann condition is applied for all variables except for the velocity component normal to the boundary. Unfortunately, it was observed that when applying zero gradient conditions for this variable, instabilities appear. In this case, as done in Richter et al. [116], the velocity normal to the boundary u_n

is calculated by the convection equation

$$\frac{\partial u_n}{\partial t} + U_c \frac{\partial u_n}{\partial n} = 0 \,, \tag{4.35}$$

where U_c denotes a characteristic convection velocity which must be provided. Additionally, the resulting velocity is scaled with the inlet mass flux to ensure the global mass conservation.

- **Wall**. For this boundary the velocity component normal to the wall is set to zero while the tangential component can assume a value, as in the case of moving walls or be equal to zero for nonslip condition. For all scalars, except for the temperature, the Neumann condition is applied. Moreover, Dirichlet condition is employed for the temperature.
- **Symmetry**. In this case all variables receive a zero gradient Neumann condition.

4.2 Numerical Method for the Eulerian Stochastic Field Method

The equations for the ESF method, Eqs. (3.32), (3.33) and (3.34), are discretized using the same techniques given in Section 4.1. The chemical source terms necessary for solving these equations are obtained from the FGM table based on the controlling variables corresponding to that field. Moreover, the required filtered values of the transported scalars are calculated with Eq. (3.30).

For calculating the vector Wiener process, as done in Avdic et al. [11] and [12], a weak first order approximation using the dichotomic vector $\zeta(0,1)$ (see [74]) is employed

$$\mathrm{dW}_j^n = \zeta(0,1)\sqrt{\Delta t} \,, \tag{4.36}$$

in which $\zeta(0,1) \approx \{-1,1\}$. As it can be seen, a positive or negative unity is then associated to each sample, depending on its sign within the normal distribution used. More details about the approximation of this term can be found in Avdic [10].

4.3 Overall Solution Procedure for Simulation without Radiation

An overall solution procedure for the simulations without the radiation solver is presented below:

1. Determine dichotomic vector $\zeta(0,1)$ as discussed in Section 4.2 and Avdic [10];
2. Runge-Kutta stages:

- Compute the Wiener term dW_j^n as given in Eq. (4.36);
- Solve transport stochastic fields ξ_{PV}^n, ξ_Z^n and ξ_h^n according to Eqs. (3.32), (3.33) and (3.34), respectively;
- Compute the momentum equations $(\bar{\rho}\widetilde{u}_j)^*$ according to Eq. (2.45);
- Access the FGM table for obtaining ρ, μ and $\dot{\omega}_k$;
- Calculate filtered values $\bar{\rho}$, $\bar{\mu}$ and $\overline{\dot{\omega}}_k$ with Eq. (3.30);
- Calculate the momentums $\widetilde{\phi}_\alpha$ and $\phi_{\alpha,\mathrm{sgs}}$ of the stochastic fields according to Eqs. (3.30) and (3.31);
- Calculate mass lack as indicated in Eq. (4.30);
- Compute the outflow velocity scaling u_n
- Update the pressure field $\overline{p}$ according to Eq. (4.34);
- Correct velocity fields $\bar{\rho}\widetilde{u}_j$ according to Eq. (4.33);

Variables as temperature or species mass fractions, except for the progress variable, are obtained in postprocessing by looking up the FGM table.

4.4 Parallelization

Since this work deals with LES of reacting flows in 3D complex geometries, the parallelization of the numerical methods employed for solving the governing equations is indispensable. The parallelization in FASTEST is done with *Message Passing Interface* (MPI) and the domain decomposition is used. This technique is convenient since FASTEST uses block structured grids and the assigning the work for each core can be done by simply distributing the blocks. The blocks can be created or subdivided in a way that an acceptable load balancing is achieved. Furthermore, ghost cells are used for the communication between the blocks. As it will be seen in the next chapter, same strategy is used for parallelizing the radiation solver.

4.5 Summary

This chapter presented the numerical methods used to solve the governing equations which describe a turbulent reacting flow. The general solution procedure was outlined in the first section, where details about the spatial and temporal discretization were given. Here, the finite volume method was applied for an arbitrary transport equation and details about the discretitzed convective and diffusive fluxes were presented. For the temporal discretization, the second-order Runge-Kutta scheme was shown. Also the algorithm for the pressure-correction in FASTEST, the fractional set projection method, was addressed in this section.

In the following sections, the discretization of the equations for the EFS method were shortly presented and the overall solution procedure for a simulation without radiation was outlined. Furthermore, in the final section, details about the parallelization in FASTEST were given.

Chapter 5

Thermal Radiation and Turbulence-Radiation Interactions

In this chapter the equation to describe the transfer of thermal radiation is presented. For this aim, first the fundamentals of the thermal radiation are briefly outlined. Then, the radiative transfer equation is described. In addition, the spectral behavior of radiative intensity is taken into focus, where the *Weighted Sum of Gray Gases* (WSGG) method is presented.

As for the governing equations given in Section 2.1.5, analytical solutions for the radiative transfer equation only exist for very simplified cases and numerical methods are indispensable for solving problems in 3D complex grids. The radiation solver implemented in this work and coupled to FASTEST is based on the finite volume method as it will be described in the following sections. Finally, in the last section an overview of turbulence-radiation interaction is presented.

Unlike presented in Chapters 2 and 3, the equations and mathematical assumptions in this chapter will be presented in vector notation. Because the radiative intensity has up to 6 independent variables (frequency of radiation, three spatial coordinates and two coordinates describing the direction of travel of the radiative intensity), it is convenient to present the mathematical background in vector notation. Most of the notations used here are in agreement with Modest [95].

5.1 Fundamentals of Thermal Radiation

Radiation can be described using quantum mechanics or classical electromagnetic wave theory. The complexity of the quantum mechanics impedes a quantum mechanical description of radiation for complicated engineering problems [58]. The classical electromagnetic wave theory, however, gives conservation equations similar to those obtained by using quantum mechanics. Thus, thermal radiation can be described by electromagnetic waves, even then its calculation requires a lot of computational resources.

From the electromagnetic point of view, thermal radiation can be defined as electromagnetic waves which are emitted by a medium only due its temperature [130]. This definition

limits the wave length to a range between 0.1 μm and 100 μm. Fig. 5.1 shows the electromagnetic wave spectrum grouped into different categories according to its behavior or occurrence.

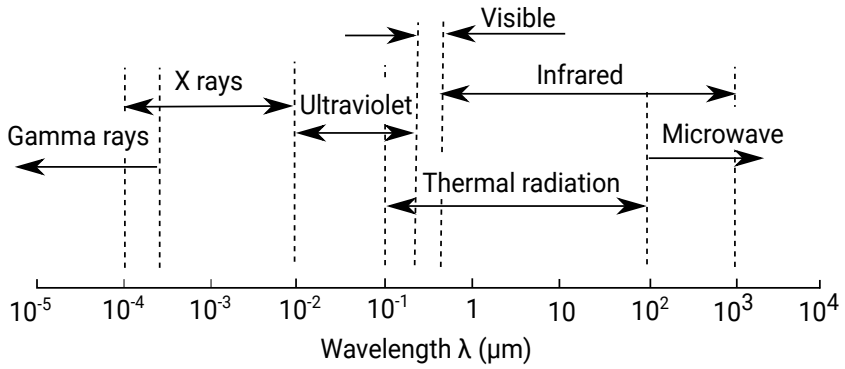

Figure 5.1: Spectrum of electromagnetic radiation (wavelength in vacuum).

In order to compute the radiative heat transfer, it is necessary to define a blackbody, the solid angles Ω and the spectral radiative intensity I_ν, described in the Sections 5.1.1, 5.1.2 and 5.1.3 respectively.

5.1.1 Blackbody

A blackbody is an idealized absorber and emitter. It emits the maximum amount of energy uniformly in all directions and wavelengths [58]. It also absorbs all the radiation incident on it independently of the direction or wavelength. The spectral black emissive power distribution $E_{b\nu}$ described by Planck's law [95] with the assumption of constant refractive index η is

$$E_{b\nu} = \frac{2\pi h_p c_0^2 \nu^5}{\eta^2 \left(e^{\frac{h_p c_0 \nu}{\eta \kappa_b T}} - 1 \right)} , \tag{5.1}$$

where h_p is known as Planck's constant $h_p = 6.6256 \cdot 10^{-34}$ Js, c_0 is the speed of light in vacuum $c_0 = 2.998 \cdot 10^8$ m/s, κ_b denotes the Boltzmann's constant $\kappa_b = 1.3805 \cdot 10^{-23}$ J/K and ν corresponds to the wavenumber.

Following Modest [95], the relation between the blackbody emissive power and intensity is given as

$$E_{b\nu} = \pi I_{b\nu} , \tag{5.2}$$

with $I_{b\nu}$ being the spectral blackbody intensity.

By integrating Eq. (5.1) over all wavenumber, it results in

$$E_b = \eta^2 \sigma T^4 , \tag{5.3}$$

where σ is known as the Stephan-Boltzmann constant $\sigma = 5.670 \cdot 10^{-8}\,\mathrm{W/m^2K^4}$. As for most gases, the refractive index η is very close to unity, thus, $\eta = 1$ is assumed in this work. Furthermore, the total blackbody intensity is given by replacing Eq. (5.3) in Eq. (5.2) yielding

$$I_b = \frac{\sigma T^4}{\pi} \,. \tag{5.4}$$

5.1.2 Solid Angles

Following Modest [95], consider a point P on an opaque surface dA as shown in Fig. 5.2. This surface radiates into a medium in all directions within a hemisphere of unit radius, as it can be seen in Fig. 5.2. In this picture an arbitrary radiation direction $\vec{\mathbf{s}}$ is indicated together with the polar angle θ, the azimuthal angle ψ and the surface normal $\vec{\mathbf{n}}$. For a hemisphere, it is know that $0 \leq \theta \leq \pi/2$ and $0 \leq \psi \leq 2\pi$.

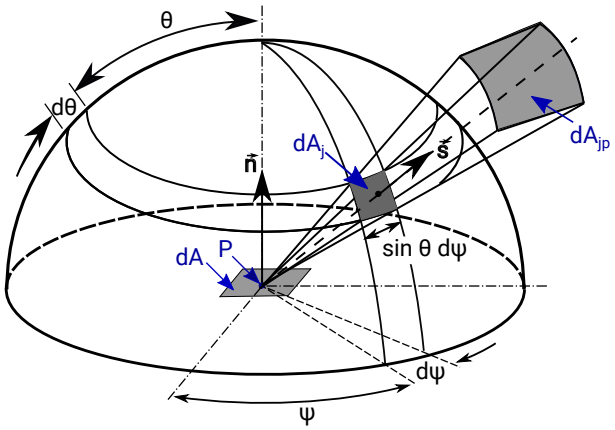

Figure 5.2: Scheme of a surface radiating and its solid angle.

The solid angle is defined as the projection of the surface onto a plane normal to the direction vector, divided by the square of the distance S, which corresponds to the distance between dA_{jp} and P as shown in 5.2. By considering that the surface is projected onto the unit hemisphere, the solid angle results in the projected area itself [95]. For an infinitesimal solid angle, it gives

$$\mathrm{d}\Omega = \frac{\mathrm{dA}_{jp}}{S^2} = \mathrm{dA}_j = (1 \times \sin\theta d\psi)(1 \times d\theta) = \sin\theta \mathrm{d}\theta\mathrm{d}\psi \,. \tag{5.5}$$

The total solid angle can be calculated as

$$\int_{\psi=0}^{2\pi} \int_{\theta=0}^{\pi/2} \sin\theta \mathrm{d}\theta\mathrm{d}\psi = 2\pi \,. \tag{5.6}$$

5.1.3 Spectral Radiative Intensity

Spectral radiative intensity I_ν can be defined as the spectral radiative energy rate per unit solid angle, per unit area normal to the rays and per unit wavelength. Additionally, the total radiative intensity is given by

$$I = \int_0^\infty I_\nu \mathrm{d}\nu. \tag{5.7}$$

5.2 Radiative Transfer Equation in Participating Media

A medium can interact with thermal radiation and in this case is referred to as 'participating medium'. The participating medium can affect the radiative intensity through absorption, emission and scattering. All these phenomena are considered in the *Radiative Transfer Equation* (RTE). As given in Modest [95], the RTE for an emitting-absorbing-scattering medium is

$$\frac{\mathrm{d}I_\nu(\mathbf{r},\mathbf{s})}{\mathrm{d}s} = \kappa_\nu I_{b\nu} - \kappa_\nu I_\nu(\mathbf{r},\mathbf{s}) - \sigma_{s\nu} I_\nu(\mathbf{r},\mathbf{s}) + \frac{\sigma_{s\nu}}{4\pi}\int_{4\pi} I_\nu(\mathbf{r},\mathbf{s}')\Phi_\nu(\mathbf{s}',\mathbf{s})\mathrm{d}\Omega' \,, \tag{5.8}$$

where I_ν represents the spectral radiation intensity at the position vector $\mathbf{r}$ and along the direction of propagation vector $\mathbf{s}$. Besides that, in the left-side of the equation, s denotes the coordinate along the direction $\mathbf{s}$. The first term of the right-hand side represents the contribution of emission. It depends on the absorption coefficient κ_ν and on the blackbody radiation intensity $I_{b\nu}$. The second term corresponds to the radiative energy loss due to absorption. The third and fourth terms are the contributions of the scattering and depend on the scattering coefficient $\sigma_{s\nu}$. The attenuation by scattering, $(-\sigma_{s\nu} I_\nu)$, represents part of the intensity which is removed from the direction $\mathbf{s}$. The augmentation by scattering, $\frac{\sigma_{s\nu}}{4\pi}\int_{4\pi} I_\nu(\mathbf{s}')\Phi_\nu(\mathbf{s}',\mathbf{s})\mathrm{d}\Omega'$, is the gain of radiative intensity from other directions $\mathbf{s}'$ that are scattered in the direction $\mathbf{s}$. The function Φ_ν is called scattering phase function and describes the probability that a ray from one direction $\mathbf{s}'$ can be scattered in direction $\mathbf{s}$. Moreover, it is important to note that the local value of I_ν depends on the wavenumber ν and on the direction $\mathbf{s}$, which is nonlocal quantity.

For problems involving combustion of methane without the presence of soot or particles, the terms of attenuation and augmentation by scattering can be neglected, as for the case of an emitting-absorbing nonscattering medium. In this case, RTE is reduced to

$$\frac{\mathrm{d}I_\nu(\mathbf{r},\mathbf{s})}{\mathrm{d}s} = \kappa_\nu I_{b\nu} - \kappa_\nu I_\nu(\mathbf{r},\mathbf{s}) \,. \tag{5.9}$$

5.2.1 Boundary Conditions for RTE

The wall surface is assumed to be diffusely emitting and reflecting, for this case the boundary condition for the RTE is expressed as [95]

$$I(\mathbf{r}_w,\mathbf{s}) = \varepsilon(\mathbf{r}_w) I_b(\mathbf{r}_w) + \frac{1-\varepsilon(\mathbf{r}_w)}{\pi} \int_{\mathbf{n}_w \cdot \mathbf{s}' < 0} I(\mathbf{r}_w,\mathbf{s}') |\mathbf{n}_w \cdot \mathbf{s}'| \mathrm{d}\Omega', \tag{5.10}$$

where $\mathbf{r}_w$ is a point on the surface, $\varepsilon(\mathbf{r}_w)$ is the wall emissivity, $\mathbf{n}_w$ denotes the local outward surface normal vector and $\mathbf{s}'$ corresponds to any incoming direction ray vector. Furthermore, for the inlet, outlet and symmetry boundary conditions, it holds $I(\mathbf{r}_{\text{boundary}},\mathbf{s}) = I_b(\mathbf{r}_{\text{boundary}})$.

5.2.2 Optical Thickness

The optical thickness or opacity τ_ν along the path length s is a useful dimensionless quantity defined as [58]

$$\tau_\nu = \int_0^s (\kappa_\nu + \sigma_{s\nu}) \mathrm{d}s' \, . \tag{5.11}$$

The optical thickness indicates how strong a medium attenuates radiation at a considered wavelength. The medium is called optically thin if $\tau_\nu \ll 1$, whereas the medium is optically thick for $\tau_\nu \gg 1$.

5.3 Radiative Heat Flux and Divergence of the Radiative Heat Flux

The spectral radiative heat flux vector $\mathbf{q}_{\mathrm{r}\nu}$ can be calculated as:

$$\mathbf{q}_{\mathrm{r}\nu} = \int_{4\pi} I_\nu \, \mathbf{s} \, \mathrm{d}\Omega \, . \tag{5.12}$$

Moreover, the radiative heat flux onto a surface element is given by

$$\mathbf{q}_{\mathrm{r}\nu} \cdot \mathbf{n} = \int_{4\pi} I_\nu \, (\mathbf{s} \cdot \mathbf{n}) \mathrm{d}\Omega, \tag{5.13}$$

where $\mathbf{n}$ is the unity normal vector outgoing from the surface element.

The divergence of the radiative heat flux is expressed as [95]

$$\nabla \cdot \mathbf{q}_{\mathrm{r}} = \nabla \cdot \int_0^\infty \mathbf{q}_{\mathrm{r}\nu} \mathrm{d}\nu = \int_0^\infty \kappa_\nu \left(4\pi I_{b\nu} - \int_{4\pi} I_\nu \mathrm{d}\Omega \right) \mathrm{d}\nu \, . \tag{5.14}$$

Finally, with the divergence of the radiative heat flux, the radiative source term S_{r} necessary to calculate the enthalpy in the energy conservation equation Eq. (2.29), is given

as

$$S_\mathrm{r} = -\nabla \cdot \mathbf{q}_\mathrm{r} \, . \tag{5.15}$$

5.4 Spectral Treatment of Radiation

The radiative properties of gases have a strong spectral dependence. The absorption coefficient κ_ν of a gas, which is necessary for calculating the RTE, varies greatly and rapidly across the spectrum. An example is given in Fig. 5.3, where a small part of the spectrum of the CO_2 4.3 μm band at 1000 K and total pressure of 1 bar is shown.

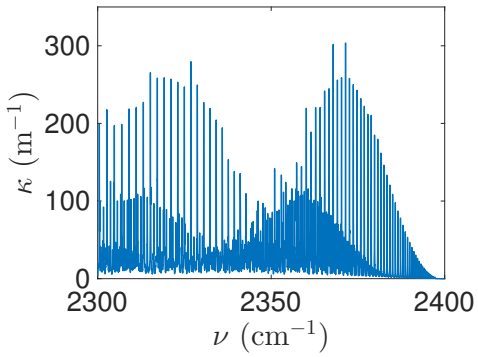

Figure 5.3: Spectral absorption coefficient for CO_2 4.3 μm band at $T = 1000\,\mathrm{K}$, $p = 1\,\mathrm{bar}$ and $p_{CO_2} = 0.1\,\mathrm{bar}$ (from HITRAN database 2012).

There are mainly four approaches to account for spectral variation in radiation properties: *Line-by-Line* (LBL), narrow band, wide band and global models.

The LBL is the most accurate. In this approach, the RTE is solved for all wavenumbers in which the absorption coefficient is given and usually high-resolution spectroscopic databases ([117], [120], [118], [134], [119]) are employed. The main drawback of this calculation is that it requires large computational resources which makes it infeasible for most engineering applications. For this reason, it is mainly used as a benchmark for the validation of more approximate spectral models.

In the narrow band models, the spectrum is divided into narrow bands and the values for the absorption coefficient are averaged over each band. Although this method requires less computational time than LBL calculations, it is still not feasible for engineering applications.

For the wide band models, the correlations are obtained by integrating narrow band results across an entire band. As reported in Modest [95], they have a typical correlational accuracy of ±30% and in some cases may have an error of as much as 70%.

In global models, the total radiative heat flux or its divergence are calculated by spectrally integrating the properties. They have the lowest computation time and, therefore, are often preferred in CFD. Within this category of models the WSGG models [97], the *Full Spectrum Correlated-k* (FSCK) method [91], the *Spectral Line Weighted sum of gray*

gases (SLW) model [40] and the *Cumulative Wavenumber* (CW) model [128] can be cited. The WSGG is most simplified one and presents satisfactory accuracy [41], [20], [61]. For these reasons, it is the model chosen in this work.

5.4.1 Weighted Sum of Gray Gases (WSGG) Model

This model was developed by Hottel and Sarofim [57] and aims to replace the spectral variation of the absorption coefficient by a small number of gray gases. As shown in Fig. 5.4, in this model, the participating medium is formed by a set of $\mathcal{I}$ gray gases with constant pressure absorption coefficients $\kappa_{\mathrm{p},i}$ which represents the highly irregular spectrum. The pressure absorption coefficient denotes the ratio between the absorption coefficient and the sum of the partial pressures of the participating species p_a, $\kappa_{\mathrm{p},i} = \kappa_i / p_a$. This model assumes that each pressure absorption coefficient $\kappa_{\mathrm{p},i}$ is independent on the temperature and on the partial pressure p_a [41].

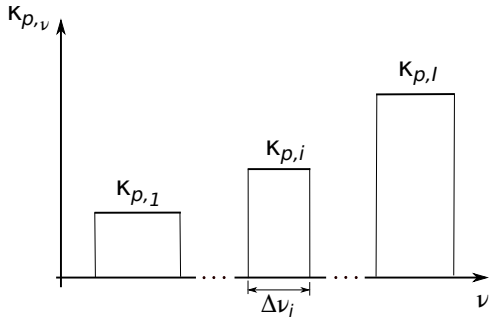

Figure 5.4: Representation of the pressure absorption coefficient with the WSGG model using I gray gases. Figure adapted from Dorigon et al. [41].

This model is based on the total emissivity of the medium along a considered path of length s, which is given as in Howell et al. [58]

$$\varepsilon = \frac{1}{I_b} \int_0^\infty (1 - \exp(-\kappa_{\mathrm{p}\nu} p_a s)) I_{b\nu} \mathrm{d}\nu \ . \tag{5.16}$$

For a binary mixture of H_2O and CO_2, the pressure absorption coefficient $\kappa_{\mathrm{p}\nu}$ is calculated as

$$\kappa_{\mathrm{p}\nu} = \frac{\kappa_{\nu,\mathrm{w}} + \kappa_{\nu,\mathrm{c}}}{p_a} \ , \tag{5.17}$$

where $p_a = p_\mathrm{w} + p_\mathrm{c}$, and p_w and p_c denote the partial pressures of H_2O and CO_2, respectively.

With the WSGG model, the total emissivity is computed as:

$$\varepsilon = \sum_{i=0}^{\mathcal{I}} a_i(T)[1 - \exp(-\kappa_{\mathrm{p},i} p_a s)] \ , \tag{5.18}$$

in which $a_i(T)$ is the weighting factor of the gray gas i depending on the temperature T. This factor represents the fraction of the blackbody emission corresponding to the

spectral interval $\Delta_{\nu i}$, as shown in Fig. 5.4. The coefficients a_i and $\kappa_{\mathrm{p},i}$ are obtained by fitting Eq. (5.18) with the emittance data calculated by accurate models as the LBL or a narrow band model.

Two formulations can be employed in this model: a gray and a nongray. The gray formulation implies that a single RTE is calculated for the spectrally averaged intensity by using total properties. In the nongray model, the RTE is solved for each considered gray gas i.

In the present work, the nongray WSGG models with the coefficients obtained by Dorigon et al. [41], Johansson et al. [61] and Bordbar et al. [16] were implemented. Besides that, the gray WSGG model of Johansson et al. [61] was additionally implemented. The coefficients given in Dorigon et al. [41] were developed for air combustion while the coefficients presented in Bordbar et al. [16] were presented for oxyfuel combustion. Moreover, the coefficients presented in Johansson et al. [61] can be used in both combustion environments.

Dorigon et al. [41] and Bordbar et al. [16] obtained the coefficients by using a recent spectral data HITEMP2010 [119]. While in the work of Johansson et al. [61] the HITRAN92 [117] database was employed.

In the work of Bordbar et al. [16] and Johansson et al. [61] the effects of the variation of the partial pressure of each species are considered, which differ from the work of Dorigon et al. [41] where a fixed partial pressure ratio p_w/p_c is used for determining the coefficients.

In the following sections, for simplicity reasons, the above mentioned models will be presented for nonscattering media.

5.4.1.1 Nongray WSGG Model

By employing the nongray WSGG model, the RTE given in Eq. (5.9) takes the form [97]:

$$\frac{\mathrm{d}I_i}{\mathrm{d}s} = \kappa_i a_i I_b - \kappa_i I_i \ , \tag{5.19}$$

where the subscript i represents the considered gray gas and κ_i is calculated as $\kappa_i = (p_\mathrm{w} + p_\mathrm{c})\kappa_{\mathrm{p},i}$. Besides that, the total radiative intensity is computed as

$$I = \sum_{i=0}^{\mathcal{I}} I_i \ . \tag{5.20}$$

Finally, the radiative heat source given in Eq. (5.15) is expressed in the context of the nongray WSGG model as

$$S_\mathrm{r} = -\sum_{i}^{\mathcal{I}} \left(4\pi\kappa_i a_i I_b - \int_{4\pi} \kappa_i I_i \mathrm{d}\Omega \right) \ . \tag{5.21}$$

Nongray WSGG Model of Dorigon et al. [41]

The authors approximated the weighting factor a_i by the polynomial function,

$$a_i = \sum_{k=1}^{K} b_{i,k} T^{k-1} \ , \tag{5.22}$$

where $b_{i,k}$ corresponds to the polynomial coefficients of each gray gas i. The transparent windows are taken into account when $i = 0$ and the absorption coefficient is equal to zero and its corresponding weighting factor is computed as,

$$a_0 = 1 - \sum_{i=1}^{\mathcal{I}} a_i \ . \tag{5.23}$$

In this model the coefficients a_i and κ_i were determined by fitting the emittance data calculated by the LBL model with 4 gray gases ($I = 4$). Their obtained coefficients are shown in Table 5.1.

Table 5.1: WSGG model coefficients for $p_w/p_c = 2$ (Dorigon et al. [41]).

i	$\kappa_{\mathrm{p},i}$ ($\mathrm{m^{-1}atm^{-1}}$)	$b_{i,1} \times 10^1$ (-)	$b_{i,2} \times 10^4$ ($\mathrm{K^{-1}}$)	$b_{i,3} \times 10^7$ ($\mathrm{K^{-2}}$)	$b_{i,4} \times 10^{11}$ ($\mathrm{K^{-3}}$)	$b_{i,5} \times 10^{14}$ ($\mathrm{K^{-4}}$)
1	0.192	0.5617	7.8440	-8.5630	4.246	-7.44
2	1.719	1.4260	1.7950	-0.1077	-0.6972	1.774
3	11.37	1.3620	2.5740	-3.7110	1.575	-2.267
4	111.016	1.222	-0.2327	-0.7492	0.4275	-0.6608

Nongray WSGG Model of Bordbar et al. [16]

In this method the weighting factor a_i is given as

$$a_i = \sum_{j=0}^{4} b_{i,j} \left(\frac{T}{T_{\mathrm{ref}}} \right)^j \ , \tag{5.24}$$

where T_{ref} is selected as 1200 K. The coefficients $b_{i,k}$ is a polynomial function of the molar ratio:

$$b_{i,j} = \sum_{k=0}^{4} C_{i,j,k} \left(\frac{X_{\mathrm{H_2O}}}{X_{\mathrm{CO_2}}} \right)^k \ . \tag{5.25}$$

The absorption coefficient of each considered gray gas is calculated as

$$\kappa_i = \sum_{k=0}^{4} d_{i,k} \left(\frac{X_{\mathrm{H_2O}}}{X_{\mathrm{CO_2}}} \right)^k \ . \tag{5.26}$$

The model coefficients of Eqs. (5.25) and (5.26) were calculated based on the LBL model and the results are shown in Table 5.2.

Nongray WSGG model of Johansson et al. [61]

Table 5.2: WSGG model coefficients (Bordbar et al. [16]).

coef. name	i	j	$k=0$	$k=1$	$k=2$	$k=3$	$k=4$
C	1	0	0.7412956	-0.5244441	0.5822860	-0.2096994	0.0242031
C	1	1	-0.9412652	0.2799577	-0.7672319	0.3204027	-0.0391017
C	1	2	0.8531866	0.0823075	0.5289430	-0.2468463	0.0310940
C	1	3	-0.3342806	0.1474987	-0.4160689	0.1697627	-0.0204066
C	1	4	0.0431436	-0.0688622	0.1109773	-0.0420861	0.0049188
d	1	-	0.0340429	0.0652305	-0.0463685	0.0138684	-0.0014450
C	2	0	0.1552073	-0.4862117	0.3668088	-0.1055508	0.0105857
C	2	1	0.6755648	1.4092710	-1.3834490	0.4575210	-0.0501976
C	2	2	-1.1253940	-0.5913199	0.9085441	-0.3334201	0.0384236
C	2	3	0.6040543	-0.0553385	-0.1733014	0.0791608	-0.0098934
C	2	4	-0.1105453	0.0464663	-0.0016129	-0.0035398	0.0006121
d	2	-	0.3509457	0.7465138	-0.5293090	0.1594423	-0.0166326
C	3	0	0.2550242	0.3805403	-0.4249709	0.1429446	-0.0157408
C	3	1	-0.6065428	0.3494024	0.1853509	-0.1013694	0.0130244
C	3	2	0.8123855	-1.1020090	0.4046178	-0.0811822	0.0062981
C	3	3	-0.4532290	0.6784475	-0.3432603	0.0883088	-0.0084152
C	3	4	0.0869309	-0.1306996	0.0741446	-0.0202929	0.0020110
d	3	-	4.5707400	2.1680670	-1.4989010	0.4917165	-0.0542999
C	4	0	-0.0345199	0.2656726	-0.1225365	0.0300151	-0.0028205
C	4	1	0.4112046	-0.5728350	0.2924490	-0.0798076	0.0079966
C	4	2	-0.5055995	0.4579559	-0.2616436	0.0764841	-0.0079084
C	4	3	0.2317509	-0.1656759	0.1052608	-0.0321935	0.0033870
C	4	4	-0.0375491	0.0229520	-0.0160047	0.0050463	-0.0005364
d	4	-	109.81690	-50.923590	23.432360	-5.1638920	0.4393889

In this model, the coefficients were derived by fitting the calculated total emittance to those obtained by the *Statistical Narrow-Band* (SNB) model [89] with 4 gray gases. The weighting factor a_i is given by the polynomial function,

$$a_i = \sum_{k=1}^{K} c_{i,k} \left(\frac{T}{T_{\text{ref}}} \right)^{k-1} , \tag{5.27}$$

where $T_{\text{ref}} = 1200\,\text{K}$ and the coefficients $c_{i,k}$ are expressed as

$$c_{i,k} = C1_{i,k} + C2_{i,k} \frac{X_{\text{H}_2\text{O}}}{X_{\text{CO}_2}} + C3_{i,k} \left(\frac{X_{\text{H}_2\text{O}}}{X_{\text{CO}_2}} \right)^2 , \tag{5.28}$$

with $X_{\text{H}_2\text{O}}$ and X_{CO_2} being the molar fraction of H_2O and CO_2. The weighting factor for the transparent gas ($i = 0$) is calculated as in Eq. (5.23). Furthermore, it is assumed

that the absorption coefficient is linearly dependent on the molar ratio,

$$\kappa_i = K1_i + K2_i \frac{X_{\mathrm{H_2O}}}{X_{\mathrm{CO_2}}} \ . \tag{5.29}$$

The model coefficients of Eqs. (5.28) and (5.29) are presented in Table 5.3.

Table 5.3: WSGG model coefficients (Johansson et al. [61]).

i	1	2	3	4
$K1_i$	0.055	0.88	10	135
$K2_i$	0.012	-0.021	-1.6	-35
$C1_{i,1}$	0.358	0.392	0.142	0.0798
$C1_{i,2}$	0.0731	-0.212	-0.0831	-0.0370
$C1_{i,3}$	-0.0466	0.0191	0.0148	0.0023
$C2_{i,1}$	-0.165	-0.291	0.348	0.0866
$C2_{i,2}$	-0.0554	0.644	-0-294	-0.106
$C2_{i,3}$	0.0930	-0.209	0.0662	0.0305
$C3_{i,1}$	0.0598	0.0784	-0.122	-0.0127
$C3_{i,2}$	0.0028	-0.197	0.118	0.0169
$C3_{i,3}$	-0.0256	0.0662	-0.0295	-0.0051

5.4.1.2 Gray WSGG Model

In this formulation, the RTE is expressed as

$$\frac{\mathrm{d}I}{\mathrm{d}s} = \kappa I_b - \kappa I \ , \tag{5.30}$$

where the absorption coefficient κ is calculated by

$$\kappa = -\log(1-\varepsilon)/S_{\mathrm{char}} \ , \tag{5.31}$$

with emissivity ε given by Eq. (5.18) and S_{char} being a characteristic length.

Finally, the radiative heat source given in Eq. (5.15) is calculated in the context of the gray WSGG model as

$$S_{\mathrm{r}} = -\left(4\pi\kappa I_b - \int_{4\pi} \kappa I \mathrm{d}\Omega\right) \ . \tag{5.32}$$

The gray model of Johansson et al. [61] is additionally implemented in this work. In this model the characteristic length S_{char} is assumed to be $3.6V/A$, where V is the volume of the domain and A the corresponding surface area. Besides that, the coefficients a_i and κ_i necessary to calculate the total emissivity ε in Eq. (5.18) are presented, as for the nongray model, in Table 5.3.

5.5 Numerical Methods for the Radiative Transfer Equation

The most common methods that can be found in the literature to solve the RTE are: the method of spherical harmonics (P_N-Approximation), the zonal method, the Monte Carlo method, the discrete transfer radiation model, *Discrete Ordinates Method* (DOM) and its variation the *Finite Volume Method* (FVM). For a more in-depth knowledge and comprehensive description of these methods, the reader is referred to Modest [95] and Howell et al. [58].

In the method of spherical harmonics, the radiative intensity is expanded into a finite series of spherical harmonics and its inverse results in the radiance moments [58]. According to Modest [95], the great advantage of this methods is the conversion of the governing equation to relatively simple partial differential equations. The $P-1$ approximation is the most employed one and has the lowest order.

In the zonal method the enclosure is subdivided into a finite number of isothermal volume and surface area zones. Then, an energy balance is applied for the radiative exchange between two zones, using precalculated exchange areas. Limitations for this method appears when applying it to complex configuration and/or to anisotropically scaterring media.

The Monte Carlo method is based on statistical concepts. It can be applied for relatively complicated problems but by increasing the complexity, greater the required computational costs are [19].

The discrete transfer radiation model combines characteristics of the DOM, the zonal method and the Monte Carlo method. One of its shortcomings is that it is difficult to include anisotropic scattering in the formulation.

Finally, the DOM is based on a discrete representation of the directional variation of the radiative intensity. Similar to the spherical harmonics method, it also reduces the RTE into a set of partial differential equations. In the DOM, a weight is assigned to every direction and the spatial discretizations can be done, for example, using the finite volume or the finite difference method. The finite volume method is a variation of the DOM which has been receiving great attention and becoming also very popular. In the FVM, both spatial and angular discretization of the RTE are done by employing the finite volume discretization procedure [35, 24, 23]. This method is fully conservative and there is no loss of radiative energy [95].

In general there is not one method that can be considered the best choice for all engineering problems. The suitable method depends on the problem and its requirements [124]. The finite volume method is the approach chosen in this work. This method is suitable for a direct coupling with FASTEST because, as already mentioned, the spatial discretization is also done with the finite volume method. It also presents a good compromise between accuracy and computational requirements [65]. Furthermore, this method can be employed for nongray anisotropical medium and it is also valid for a wide range of optical thicknesses (see Section 5.2.2 for the definition of optical thickness).

The history of the FVM for solving the RTE started with the work of Raithby and Chui [113]. They investigated one and two dimensional problems in Cartesian grids. They extended their studies to nonorthogonal meshes in [28]. In that paper they explored 2D curved and nonrectangular geometries. Also for 2D irregular geometries, the work of Chai et al. [25] can be cited. For 3D nonorthogonal geometries, Beak et al. [13] applied the FVM for several geometries, including a kidney-shaped combustion chamber with a moderate spatial grid. For unstructured grids, Murthy and Mathur [98] employed the FVM for computing the RTE in an arbitrary unstructured polyhedra. In this work, for the coupling with FASTEST, the RTE is solved in block structured grids. In context of block structured grids and FVM, Chai and Moder [22] investigated straight and curved interfaces in continuous and discontinuous 2D grids. Also employing block structured grids, the work from Talukdar at al. [133] can be mentioned. They focused their study on continuous grid and computed several 3D problems.

As for the fluid solver, the RTE is also solved in this work in block structured grids. For the coupling between CFD and radiation, it is convenient to avoid interpolations by using the same grid type in both solvers.

In the next sections, the finite volume discretization method for solving the RTE is presented and three different strategies are shown for solving the discrete set of equations obtained by employing the FVM. Then, the discretized radiative source term is addressed and the shortcomings of FVM for solving the RTE are briefly discussed.

5.5.1 Finite Volume Method for the RTE

For simplicity reasons the discretization of the RTE are shown for a gray medium. By employing the finite volume method, this equation is integrated not only over the solid angle element Ω_j, but also over the element of volume V_p, as done in [113], resulting in:

$$\sum_{k}^{N_{\text{faces}}} I_{k,j} D_{k,j} A_k = [-(\kappa_p + \sigma_{s,p}) I_{p,j} + S_{p,j}] V_p \Omega_j \ , \tag{5.33}$$

$$S_{p,j} = \kappa_p I_{b,p} + \frac{\sigma_{s,p}}{4\pi} \sum_{i}^{N_{\text{directions}}} I_{p,i} \Phi_{p,j} \Omega_i, \tag{5.34}$$

where the subscripts k and p denote the volume's face with area A_k and the volume's center, respectively. Besides that, the subscript j represents the discrete radiation direction and the the solid angle element Ω_j is determined as shown in Section 5.1.2. The term $D_{k,j}$ is calculated as:

$$D_{k,j} = \int_{\Omega_j} (\mathbf{s}_j \cdot \mathbf{n}_k) \mathrm{d}\Omega_j \ , \tag{5.35}$$

in which $\mathbf{s}_j$ is the direction vector and $\mathbf{n}_k$ denotes the normal vector of the face k directed outwards.

For solving this integral each direction vector $\mathbf{s}_j$ is described by using spherical coordinates. Fig. 5.5 (a) represents the discretized solid angles and examples of direction vectors $\mathbf{s}_j$.

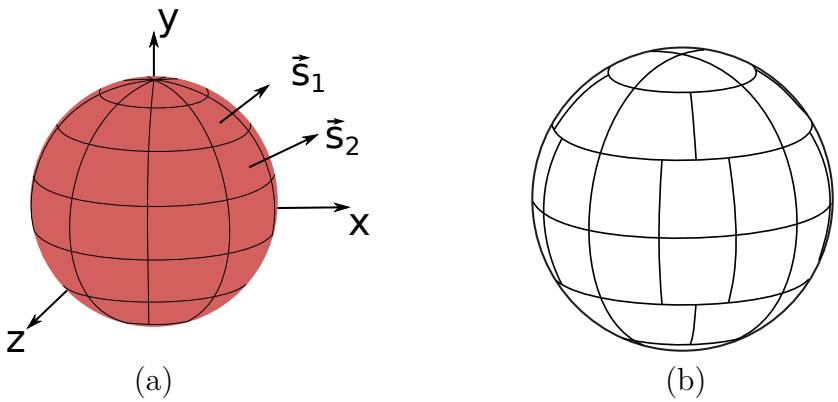

Figure 5.5: Representation of the discretized solid angles (a) with constant angle distribution and direction vectors and (b) with the angular distribution proposed in the method FT_n FVM.

In this work, the angular discretization is accomplished with the method FT_n FVM, introduced by Kim and Huh [72]. In this method the polar angle is divided equally into an even number, n, while the azimuthal angle is uniformly divided into a number from the sequence of 4,8,...$2n-4$,$2n$,$2n-4$,...8,4 in each interval of the polar angles. With this procedure the discretized control angles are distributed more uniformly in comparison to the standard FVM. Fig. 5.5 (b) shows a representation of discrete solid angles for this method.

In order to obtain the radiative intensity at the volume's face necessary for calculating Eq. (5.33), the step scheme is employed, which is a first order scheme. This scheme has been widely used because of inherent stability. Alternatives can be found in the literature as the diamond scheme, which corresponds to the central difference scheme. This scheme is second-order accurate, but is boundedness. Besides that, also the CLAM scheme [136] can be cited. It is a second order scheme with a flux limiter for avoiding the nonphysical results but it can only be applied for orthogonal grids. A comparison about different spatial discretization schemes for solving the RTE can be found in Coelho [32].

By using the step scheme, the radiative intensity leaving the volume at a face is approximated with the value in the center of the volume, $I_p = I_{out}$. Substituting this in Eq. (5.33), yields the algebraic equation for I_p:

$$a_{p,j} I_{p,j} = - \sum_{\substack{k \\ D_{k,j}<0}}^{N_{\text{faces}}} D_{k,j} A_k I_{k,j} + S_{p,j} V_p \Omega_j, \tag{5.36}$$

and the a_p coefficient is given by

$$a_{p,j} = (\kappa_p + \sigma_{s,p}) V_p \Omega_j + \sum_{\substack{k \\ D_{k,j}>0}}^{N_{\text{faces}}} D_{k,j} A_k. \tag{5.37}$$

By applying the FVM method to discretize for the equation of the diffusely emitting and reflecting wall surfaces boundary condition, it yields

$$I_w = \epsilon_w I_{\mathrm{b},w} + \frac{1-\epsilon_w}{\pi} \sum_{\substack{j \\ D_{w,j}<0}}^{N_{\mathrm{directions}}} I_{w,j} |D_{w,j}| \ , \tag{5.38}$$

where I_w is the radiative intensity on the surface and $D_{w,j}$ is calculated as in Eq. (5.35).

If the volumes are visited in the correct order, all terms of the right side in Eq. (5.36) are known and I_p at each node can be calculated by direct substitution [28]. Thus, the solution can be obtained by visiting the nodes following an optimal order. This procedure is called mesh sweeping algorithm. For simple Cartesian grids, the marching order can be easily found but in the case of complex meshes, a list with the optimal sequence should be created. This list is created in this work by following the procedure of Joseph at al. [65]. Once the list is found for each direction, it is saved and used for the calculations.

By applying the mesh sweeping algorithm for nonreflecting boundaries, a nonscattering medium and serial computations the solution can be obtained once all domain is swept, otherwise iterations are necessary. The solution process starts with an initial guess for the radiative intensity and Eq. (5.36) is solved for all discrete directions. This process is repeated until the convergence criterion is satisfied,

$$d = \max_j \left(\max_p \left| \left(I^l_{p,j} - I^{l-1}_{p,j} \right) / I^l_{p,j} \right| \right) < 10^{-6}, \tag{5.39}$$

where the superscripts l and $l-1$ correspond to the radiative intensity for the actual and previous iteration, respectively.

The solution steps using the sweeping algorithm are:

1. Find a sweeping order for each processor;
2. Set an initial value for $I(\mathbf{r},\mathbf{s})$;
3. Update ghost cells;
4. Compute the discretized equation for the boundary conditions for RTE;
5. Solve the discretized RTE, Eq. (5.36), following the sweeping order;
6. Test for convergence, Eq. (5.39), and return to step 3, if not converged.

Alternatively to the sweeping algorithm, Eq. (5.36) can be solved employing an iterative solver. In this work the *Library of Iterative Solvers* (LIS) [7, 100] is coupled to the radiation solver in order to solve the system of discrete equations originated from Eq. (5.36). LIS is a parallel software library for solving linear system of equations in which many iterative solvers and preconditioners are available.

With LIS, two types of solution algorithms were implemented: 'small matrix algorithm' and 'big matrix algorithm'. In the first, the system of discrete equations is solved for each direction and an iteration process is necessary for coupling the different directions. This

way, a matrix with the coefficients for each direction is built and the solution for each direction is calculated. The solution steps for this algorithm are:

1. Set an initial value for $I(\mathbf{r},\mathbf{s})$;
2. Update ghost cells;
3. Compute the discretized equation for the boundary condition for RTE;
4. Solve the discretized RTE, Eq. (5.36), with LIS;
5. Test for convergence, Eq. (5.39), and return to step 2, if not converged.

In the second implemented solution procedure with LIS, a system of discrete equations for all directions is solved at once and, therefore, no iteration is needed in this case. The different directions are coupled with each other due to the term of augmentation by scattering or if reflecting boundary condition is employed. Thus, solving the whole linear system of equations at once is more advantageous because iterations are avoided. On the other hand, because the information about all directions should be provided at once, more computational memory (*Random-Access Memory* (RAM)) is necessary. For comparison: the system of linear equations to be solved in the 'small matrix algorithm' has $n_x \cdot n_y \cdot n_z$ unknown variables, where n_x, n_y and n_z are the number of grid points in each spatial coordinate; while the number of variables to be solved in the 'big matrix algorithm is $n_x \cdot n_y \cdot n_z \cdot N_{\text{directions}}$. The steps for the 'big matrix algorithm' are:

1. Set an initial value for $I(\mathbf{r},\mathbf{s})$;
2. Update ghost cells;
3. Solve the discretized RTE, Eq. (5.36) including the boundary conditions, with LIS.

The parallelization of FVM for radiative heat transfer can be done by using domain decomposition or angular decomposition [36]. The latter has the advantage of a higher speed up. On the other hand, the number of processors is limited to the number of chosen directions of propagation of radiative intensity and the data of the whole domain must be stored in every processor [35]. This is impractical for complex and large grids. Furthermore, the domain decomposition is employed in most CFD codes. Hence, having in mind a coupling between the radiation solver and FASTEST, the domain decomposition is more advantageous and, for this reason, it is the strategy used in this work. In this method, each processor has to store information of a part of the domain and solves the RTE for all discrete directions. As for FASTEST, the communication between the processors is done by updating the values in the ghost cells in every iteration.

5.5.2 Finite Volume Method for the Divergence of the Radiative Heat Flux

As done for discretization of the RTE, for simplicity reasons, the discretized radiative source term for a gray medium is presented. By applying the FVM to Eq. (5.32), it leads

to

$$S_{\mathrm{r},p} = -\left(4\pi\kappa_p I_{b,p} - \sum_{j}^{N_{\mathrm{directions}}} \kappa_p I_{p,j}\Omega_j\right) . \tag{5.40}$$

5.5.3 Shortcomings of the Employed Methods for Solving the RTE

Two shortcomings of the methods applied in this work are presented in this section: false scattering and ray effect.

False scattering appears because of the step scheme used and it is commonly called false diffusion in the CFD community. It denotes the nonphysical smearing of the radiative intensity even without the presence of a scattering medium. According to Chai et al. [21] this effect can be reduced by refining the grid.

Ray effect is a consequence of the angular discretization. As presented in Chai et al. [21], if one employs only specific discrete directions for approximating a continuously varying angular nature of radiation, ray effect is encountered. To illustrate this phenomenon, consider a two-dimensional enclosure with black walls, as shown in Fig. 5.6, containing a nonparticipating medium. Furthermore, three of the walls are cold and the bottom wall contains a small heated strip. Because of the angular discretization, the radiative rays propagate only in specific directions. As a results, only some strips on the other walls are heated. It can be clearly seen that this effect can be reduced by increasing the number of considered directions.

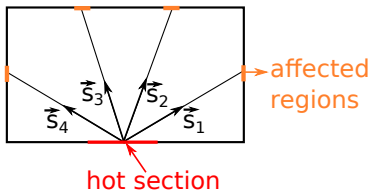

Figure 5.6: Illustration of the Ray effect.

5.6 Overall Solution Procedure for Simulation with Radiation

An overall solution procedure including the radiation solver in presented below:

1. Determine dichotomic vector $\zeta(0,1)$ as discussed in Section 4.2 and Avdic [10];
2. Runge-Kutta stages:
   - Compute the Wiener term dW_j^n as given in Eq. (4.36);
   - Compute transport stochastic fields ξ_{PV}^n, ξ_Z^n and ξ_h^n according to Eqs. (3.32), (3.33) and (3.34), respectively;

- Compute the momentum equations $(\bar{\rho}\widetilde{u}_j)^*$ according to Eq. (2.45);
- Access the FGM table for obtaining ρ, μ and $\dot{\omega}_k$;
- Calculate filtered values $\bar{\rho}$, $\bar{\mu}$ and $\overline{\dot{\omega}}_k$ with Eq. (3.30);
- Calculate the momentum of stochastic fields $\widetilde{\phi}_\alpha$ and $\phi_{\alpha,\mathrm{sgs}}$ according to Eqs. (3.30) and (3.31);
- Calculate mass lack as indicated in Eq. (4.30);
- Compute the outflow velocity scaling u_n
- Update the pressure field $\overline{p}$ according to Eq. (4.34);
- Correct velocity fields $\bar{\rho}\widetilde{u}_j$ according to Eq. (4.33);

3. Access the FGM table for obtaining T, $X_{\mathrm{CO_2}}$ and $X_{\mathrm{H_2O}}$;
4. Compute T^4 and $\kappa_\nu I_{b\nu}$;
5. Calculate filtered values $\overline{T}$, $\overline{X}_{\mathrm{CO_2}}$, $\overline{X}_{\mathrm{H_2O}}$, $\overline{T^4}$ and $\overline{\kappa_\nu I_{b\nu}}$ with Eq. (3.30);
6. Compute the radiative intensity according to the RTE Eq. (5.33);
7. Compute the radiative source term Eq. (5.40).

For the applications studied in this work, in order to reduce the computational time when radiation is considered, the radiation solver is computed at a frequency of f_{rad}, which is set depending on the case studied. This way, the radiative source term is computed at the beginning of the simulation and is updated in a frequency of f_{rad}. The same procedure is used in Goncalves dos Santos et al. [42].

5.7 Turbulence-Radiation Interactions (TRI)

As this work investigates *Turbulence-Radiation Interactions* (TRI) in the combustion of methane without the presence of soot or particles. Therefore scattering is neglected and Eq. (5.9) is employed in this section.

In order to account for radiative heat transfer for flame simulations in the context of LES, it is necessary to work with the filtered RTE and, consequently, filtered radiative source term. Following Coelho [34], the filtered RTE for an emitting-absorbing nonscattering medium can be written as:

$$\frac{\mathrm{d}\overline{I}_\nu}{\mathrm{d}s} = \overline{\kappa_\nu I_{b\nu}} - \overline{\kappa_\nu I_\nu}, \tag{5.41}$$

where the overline denotes a filtered quantity as seen in Section 2.2.2. Similarly, the filtered radiative source term is given as

$$\overline{S}_\mathrm{r} = -\overline{\nabla \cdot \mathbf{q}_\mathrm{r}} = -\int_0^\infty 4\pi\overline{\kappa_\nu I_{b\nu}}\mathrm{d}\nu + \int_0^\infty \int_{4\pi} \overline{\kappa_\nu I_\nu}\mathrm{d}\Omega\mathrm{d}\nu \ . \tag{5.42}$$

Unfortunately, the filtered radiation intensity and heat fluxes computed with the filtered values of temperature and species concentration may be different from those calculated with the entire values,

$$\overline{\kappa_\nu(T,X_{\text{species}})I_{b\nu}(T)} \neq \kappa_\nu(\overline{T},\overline{X}_{\text{species}})I_{b\nu}(\overline{T}) \ ,$$
$$\overline{\kappa_\nu(T,X_{\text{species}})I_\nu} \neq \kappa_\nu(\overline{T},\overline{X}_{\text{species}})I_\nu \ .$$

This behavior occurs due the highly nonlinear coupling between fluctuations of radiative intensity, temperature and species concentration, as it can been in Eqs. (5.43) and Eqs. (5.44)

As done in Section 2.2.2 an arbitrary variable φ can be split into a filtered $\overline{\varphi}$ (resolved) and a subgrid φ^{sgs} (unresolved) scale. If the same idea is applied for each term of Eq. (5.42), it leads to

$$\begin{aligned}\overline{S}_{\text{r,emission}} &= \int_0^\infty 4\pi\overline{\kappa_\nu I_{b\nu}}\mathrm{d}\nu \\ &= \int_0^\infty 4\pi\left(\overline{\overline{\kappa}_\nu\overline{I}_{b\nu}} + \overline{\overline{\kappa}_\nu I_{b\nu}^{\text{sgs}}} + \overline{\kappa_\nu^{\text{sgs}}\overline{I}_{b\nu}} + \overline{\kappa_\nu^{\text{sgs}}I_{b\nu}^{\text{sgs}}}\right)\mathrm{d}\nu \ ,\end{aligned} \tag{5.43}$$

and

$$\begin{aligned}\overline{S}_{\text{r,absorption}} &= \int_0^\infty\int_{4\pi}\overline{\kappa_\nu I_\nu}\mathrm{d}\Omega\mathrm{d}\nu \\ &= \int_0^\infty\int_{4\pi}\left(\overline{\overline{\kappa}_\nu\overline{I}_\nu} + \overline{\overline{\kappa}_\nu I_\nu^{\text{sgs}}} + \overline{\kappa_\nu^{\text{sgs}}\overline{I}_\nu} + \overline{\kappa_\nu^{\text{sgs}}I_\nu^{\text{sgs}}}\right)\mathrm{d}\Omega\mathrm{d}\nu \ .\end{aligned} \tag{5.44}$$

The first term of Eq. (5.43) corresponds to the correlation between resolved-scale in κ_ν and resolved-scale in $I_{b\nu}$. The second term is the correlation between the resolved-scale in κ_ν and the subgrid-scales in $I_{b\nu}$. The third term presents the correlation between the subgrid-scales in κ_ν and the resolved scale in $I_{b\nu}$. The last term, $\overline{\kappa_\nu^{\text{sgs}}I_{b\nu}^{\text{sgs}}}$, corresponds to the correlation between subgrid-scale quantities of κ_ν and $I_{b\nu}$. Similar interpretation can be given for the filtered absorption term shown in Eq. (5.44).

The terms for calculating the radiative source term can be obtained by approximated solutions or by employing PDF methods. The emission term depends only on local quantities (T, X_{species}) while the absorption term has a nonlocal character. It is dependent on the radiative intensity, which depends on the properties of the whole domain. Therefore, this term is much more complex to approximate.

The filtered absorption term can be approximated by using the *Optically Thin Fluctuation Assumption* (OTFA), which is valid when the mean free path for radiation is much larger than the turbulence length scale l_t. The mean free path for radiation is defined as the average distance a photon travels before interacting with a molecule [95]. As discussed in Kabashnikov and Myasnikova [66], in this case the local radiative intensity should be weakly correlated with the local absorption coefficient. This approximation assumes that the individual eddies are homogeneous, optically thin and statistically independent [31]. According to Modest and Haworth [96], the suitability of this approximation depends on the eddy size distribution and the absorption coefficient of the participating medium. In

the work of Coelho [31], this approach was employed for Sandia flame D in a RANS context and its validity was demonstrated for the studied problem. Furthermore, as discussed by Modest and Haworth [96] and in Gupta [50], since radiation is a large-scale phenomenon, this assumption is expected to be even better in the LES context. With the OTFA, the subgrid-scale fluctuations are neglected and the filtered absorption term can be rewritten as

$$\overline{S}_{\mathrm{r,absorption}} = \int_0^\infty \int_{4\pi} \overline{\kappa_\nu I_\nu} \mathrm{d}\Omega \mathrm{d}\nu \approx \int_0^\infty \int_{4\pi} \overline{\kappa}_\nu \overline{I}_\nu \mathrm{d}\Omega \mathrm{d}\nu \ . \tag{5.45}$$

The emission term is a function of local quantities $(T, X_{\mathrm{species}})$ and the filtered emission term depends on the

- temperature self-correlation $\overline{T^4}$, necessary to calculate the filtered blackbody radiative intensity,
$$\overline{I}_{b\nu} = \frac{\sigma \overline{T^4}}{\pi} \ , \tag{5.46}$$
and its subgrid quantity $I_{b\nu}^{\mathrm{sgs}}$;
- absorption coefficient self-correlation $\overline{\kappa}_\nu$ and its corresponding subgrid-scale $\kappa_\nu^{\mathrm{sgs}}$, which depend on the temperature and species concentrations.

As an example for the approximations found in the literature for calculating the emission term, the work of Snegirev [127] can be cited. In the context of RANS, the author developed an expression to approximate the emission term based on the expansion of the instantaneous values in Taylor series and keeping the terms up to the second order.

In this work the filtered emission term is calculated by using four different ways:

- method 0, in which the mean values are used:
$$\overline{S}_{\mathrm{r,emission}} = \int_0^\infty 4\pi \overline{\kappa_\nu I_{b\nu}} \mathrm{d}\nu \approx \int_0^\infty 4\pi \langle \kappa_\nu \rangle \langle I_{b\nu} \rangle \mathrm{d}\nu \ , \tag{5.47}$$
where $\langle \kappa_\nu \rangle = \kappa_\nu(\langle T \rangle, \langle X_{\mathrm{species}} \rangle)$, $\langle I_{b\nu} \rangle \approx I_{b\nu}(\langle T \rangle^4)$ and $\langle\rangle$ expresses a time averaging.
- method 1, in which the instantaneous filtered values are used and the subgrid-scales are neglected:
$$\overline{S}_{\mathrm{r,emission}} = \int_0^\infty 4\pi \overline{\kappa_\nu I_{b\nu}} \mathrm{d}\nu \approx \int_0^\infty 4\pi \overline{\kappa}_\nu \overline{I}_{b\nu} \mathrm{d}\nu \ , \tag{5.48}$$
where $\overline{\kappa}_\nu = \kappa_\nu(\overline{T}, \overline{X}_{\mathrm{species}})$ and $\overline{I}_{b\nu} \approx I_{b\nu}(\overline{T}^4)$.
- method 2, in which the filtered values are used and the subgrid-scales are partially considered. $\overline{S}_{\mathrm{r,emission}}$ is computed as in method 1, with Eq. (5.48), but taking into account the temperature fluctuations, $\overline{I}_{b\nu} = I_{b\nu}(\overline{T^4})$.
- method 3, in which the filtered values are used and the subgrid-scales are also taken into account.

As already mentioned, the ESF and FGM methods are used in this work. In this context the temperature and species concentrations are obtained from the FGM table based on the controlling variables of each stochastic field of the ESF method. Furthermore, the corresponding filtered temperature and species concentrations are calculated with Eq. (3.30). For computing $\overline{T^4}$ in method 2 and the $\overline{\kappa_\nu I_{b\nu}}$ in method 3, the same procedure is used, leading to

$$\overline{T^4} = \frac{1}{N} \sum_{n=1}^{N} \xi_{T^4}^n \ , \tag{5.49}$$

$$\overline{\kappa_\nu I_{b\nu}} = \frac{1}{N} \sum_{n=1}^{N} \xi_{\kappa_\nu I_{b\nu}}^n \ , \tag{5.50}$$

where $\xi_{T^4}^n$ denotes the fields of T^4 obtained with the temperature fields from the FGM table for each considered stochastic field, similarly $\xi_{\kappa_\nu I_{b\nu}}^n$ are the fields of $\kappa_\nu I_{b\nu}$ obtained with the values from the FGM table for each considered stochastic field.

It is worth to point out that with the WSGG methods employed here, the absorption coefficient is linearly dependent on the temperature and species concentrations. Therefore $\overline{\kappa}_\nu = \kappa_\nu(\overline{T},\overline{X}_{\text{species}})$ is valid.

For treating the absorption term the OTFA is assumed and this way, all the necessary variables to calculate this term are known. Thus, it can be directly calculated with the resolved-scale quantities.

5.8 Summary

This chapter presented the fundamentals of thermal radiation and numerical methods used to deal with this mode of energy transfer. In the first sections, basic concepts were explained and the radiative transfer equation was showed. Following these introductory sections, the spectral treatment of radiation were addressed. Then, the numerical methods for discretizing the RTE were described, where the FVM was applied and an overall solution procedure for the coupled simulations was outlined. In the last section, the focus was given to TRI, where the filtered radiative source term and approximations used to compute this term were presented.

Chapter 6

Verification of the Radiation Solver

The first steps towards building or extending a CFD code is verifying the implementations. For this aim in this chapter the radiation solver is verified for 2D and 3D cases in which the analytical solutions are known or the results are compared to the ones found in the literature. The absorption coefficient is assumed to be constant in these test. In the following section, tests with non uniform absorption coefficients are considered, where the implemented WSGG models are verified by applying two benchmark tests.

6.1 Verification of the Solver for the Radiative Transfer Equation

In order to verify the solver for computing the *Radiative Transfer Equation* (RTE) seven simple tests are considered in this section. In the first three tests a 2D box and a cubical enclosure are investigated. For these cases, Cartesian uniform grids with a single block are used. For the fourth and fifth cases a hexahedral enclosure and a 3D annular section are computed, herein nonorthogonal grids with a single block are employed. Then, a L-shaped enclosure is studied. The grid for this case is Cartesian uniform but it consists of 2 blocks. Finally, in the last case a cylindrical enclosure is investigated in which a nonorthogonal grid consisting of 5 blocks is employed.

For the verification pure absorbing emitting, pure isotropically scattering as well as absorbing emitting isotropically scattering media are tested. This way the routine implemented for solving the RTE with all its terms is verified. Moreover, all these verification tests were performed for the three solver algorithm: sweeping, 'small matrix' and 'big matrix'. The difference in the results between the sweeping and 'small matrix' algorithm was on the order of 10^{-15}, whereas the difference among these solvers and the 'big matrix' was $\leq 10^{-6}$, depending on the case. This is in accordance with the tolerance used in the iteration process for the sweeping and 'small matrix' algorithm, as presented in Eq. (5.39). Because of these small differences obtained among the implemented solver algorithms and to avoid confusion, only the results for the 'big matrix' are shown in the following sections.

Regarding the solver 'small matrix' and the sweeping algorithm, a performance study in order to point out the best linear solver when dealing with complex industrial size geometries and block structured grids in a parallel computation was carried out by Miranda et

al. [94, 92]. In these works, a combustion chamber experimentally studied by Habermehl et al. [52] with a fixed temperature field was investigated. A structured grid consisting of 313 blocks with around 1 million points was employed. The results showed that the best performance was obtained with the solvers sweeping algorithm and *Cyclic Reduction* (CR) [147] with *Symmetric Successive Overrelaxation* (SSOR) preconditioner [138].

6.1.1 2D Enclosure with a Pure Absorbing-Emitting Medium

This first test was presented by Raithby and Chui [113] and consists of a pure absorbing-emitting medium with temperature T_g in a 2D box-shaped enclosure with ($L_x = L_y = L$), where the walls are black and kept constant at 0 K.

The analytical solution for this case, with constant absorption coefficient, is given by Selcuk [123]

$$I(\mathbf{r},\mathbf{s}) = \kappa \int_0^s I_b(\mathbf{r} - \nu\mathbf{s}) e^{-\kappa\nu} \mathrm{d}\nu, \tag{6.1}$$

where s is the distance in the propagation direction from the wall.

However, the implemented solver is only able to deal with 3D geometries. For this reason, a geometry with $L_x = L_y = L$ and $L_z = 25L$, as shown in Fig. 6.1, is employed. In this 3D geometry the walls are located in the planes xz and yz. Besides that, the Neumann boundary condition is applied for the planes xy. This modification on the setup of the test is done in a way that the additional dimension does not affect the results. The meshes used are uniform and consist of 20 x 20 x 100 and 50 x 50 x 1000 volumes, referred to as coarse and fine grid, respectively. Such quantities of control volume are used in the third direction because no periodic boundary condition is available in the code and in order to represent a infinite long dimension in this direction, a relative high number of control volumes is employed. For the angular discretization $n = 4$ is used, corresponding to 24 directions. Moreover, a constant absorption coefficient, $\kappa L = 10$, is considered.

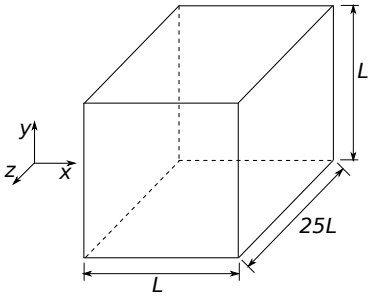

Figure 6.1: Geometry for the 2D box-shaped cases.

For each considered direction, Eq. (6.1) is numerically integrated and the obtained radiative intensity is used to calculate the local heat flux. The heat flux on the wall for the analytical and numerical solutions for the two grids are plotted in Fig. 6.2. As expected, by increasing the number of mesh points, the numerical results better follow the analytical solution.

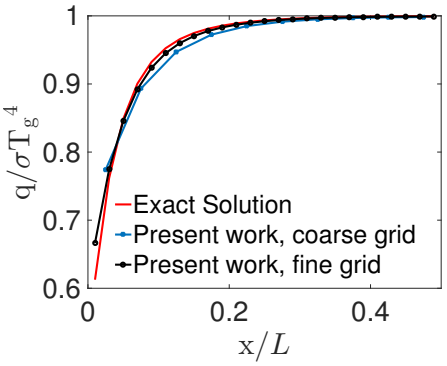

Figure 6.2: Nondimensional heat transfer on the wall for a pure absorbing and emitting medium.

6.1.2 2D Enclosure with a Pure Scattering Medium

A second test is performed for the verification of the routine for solving the scattering term. In this problem, also presented by Raithby and Chui [113], the medium scatters but does not absorb or emit ($\kappa = 0$). For this case the 3D geometry given in Fig. 6.1 is again used with the same boundary conditions as in the first test case. However, in this case the bottom wall is kept at a hot temperature T_g and the medium is maintained cold. Besides that, a constant scattering coefficient is admitted $\sigma_s L = 1$.

For this case no analytical solution is available and the results obtained here are compared with the ones found in Raithby and Chui [113]. In their investigation the authors also used the FVM for solving the RTE but an implicit solution scheme was employed to solve the linear system equations obtained by discretizing the RTE. They employed a uniform grid of 31 x 31 points and an angular discretization for 4 x 24. In this work a grid consisting of 30 x 30 x 300 volumes is used and an angular discretization of $n = 10$ is applied, corresponding to 120 directions, as for the reference solution.

The heat transfer leaving the hot wall plotted against the reference solution is presented in Fig. 6.3. A good agreement can be seen between the two plotted solutions.

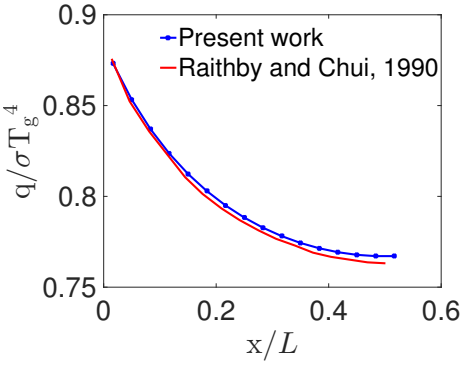

Figure 6.3: Nondimensional heat transfer on the bottom wall for a pure scattering medium.

6.1.3 Cubical Enclosure

A cubical enclosure with side length L and black walls is simulated. This problem deals with a purely absorbing emitting medium and was studied by Kim et al. [72]. The walls are kept cold and the medium is set with the following temperature distribution:

$$T(X,Y,Z) = T_o(1-r^2)(1-p^2) \tag{6.2}$$
$$r = \sqrt{2}[(Y/L_o - 1/2)^2 + (Z/L_o - 1/2)^2]^{1/2}$$
$$p = 2X/L_o - 1,$$

where T_o corresponds to the reference temperature and L_o to the characteristic length.

As for the first test, the different directions of propagation are not coupled and the analytical solution of the RTE for each direction can be found by numerically integrating Eq. (6.1). The wall radiative heat flux along the centerline on the south boundary face ($Y = 0$, $Z = 0.5L$) is calculated according to Eq. (5.13). Analytical and numerical solutions are computed by employing $n = 8$ (80 directions) and compared against each other.

As an example, the results utilizing the grid 50 x 50 x 50 and the nondimensional absorption coefficient $\kappa^* = 10$ ($\kappa^* = \kappa L$) are plotted in Fig. 6.4.

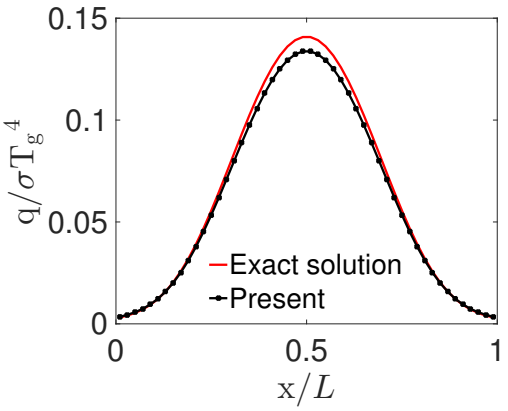

Figure 6.4: Nondimensional heat transfer on the centerline of the bottom wall ($Y = 0$, $Z = 0.5L$) for the grid 50 x 50 x 50 and the nondimensional absorption coefficient $\kappa^* = 10$.

The average error is calculated as

$$\text{Error} = \frac{1}{N}\sum_r \frac{|q^n_{w,r} - q^a_{w,r}|}{q^a_{w,r}}, \tag{6.3}$$

where N is the total number of grid points, $q^n_{w,r}$ is the numerical solution and $q^a_{w,r}$ is the analytical solution for the corresponding location r. Tests are carried out for three different grids and three different absorption coefficients. The errors found for these tests are shown in Table (6.1).

Table 6.1: Error (%) for the cubical enclosure for three different grids and three different absorption coefficients ($\kappa^* = \kappa L$).

Grid size	$\kappa^* = 0.1$	$\kappa^* = 1.0$	$\kappa^* = 10.0$
25^3	3.11	4.96	7.03
50^3	0.72	1.94	4.27
100^3	0.52	0.52	2.54

It can be observed that by increasing the number of grid points, the obtained error decreases. Furthermore, the results with the optically thick limit of $\kappa^* = 10$ are less accurate. The same behavior was reported by Kim and Huh [72].

6.1.4 Hexahedral Enclosure

The hexahedral enclosure simulated by Baek et al. [13] is computed here. The geometry for this case is shown in Fig. 6.5. The enclosure has $L_z = 1$ m and is filled with an absorbing-emitting medium with temperature $T_g = 100\,\mathrm{K}$. The walls are cold and black. The analytical solution is given by numerically integrating Eq. (6.1). The mesh utilized is uniform and consists of 13 x 13 x 13 points. Moreover, three different absorption coefficients ($\kappa = 10\,\mathrm{m}^{-1}$, $\kappa = 1\,\mathrm{m}^{-1}$ and $\kappa = 0.1\,\mathrm{m}^{-1}$) are tested.

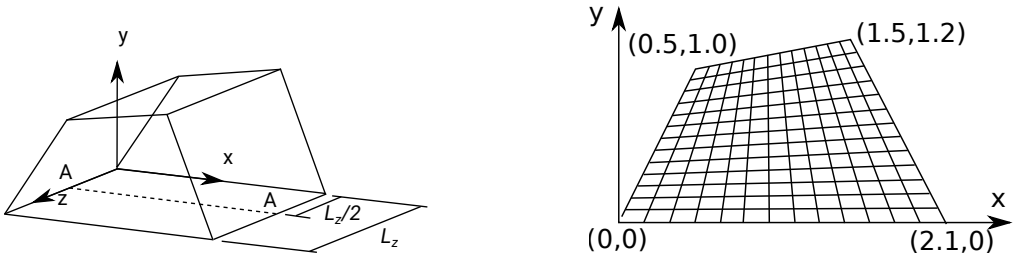

(a) (b)

Figure 6.5: (a) Geometry and (b) spatial grid of the plane xy for the hexahedral enclosure (Baek et al. [13]).

The heat flux on the wall along line A-A is plotted in Fig. 6.6. It can be seen that, also for this nonorthogonal grid, the numerical results agree well with the analytical ones.

6.1.5 3D Annular Sector

An annular section as described in Baek et al. [13] and shown in Fig. 6.7 is investigated in this work. The inner radius is 0.5 m and the outer radius is 1 m. Moreover, the angle μ is 60° and the sector has a length of 1 m.

The walls of this enclosure are black and cold, except for the inner wall, which is kept at a higher temperature ($T_{in} = 100\,\mathrm{K}$). The gas inside the enclosure is considered as an

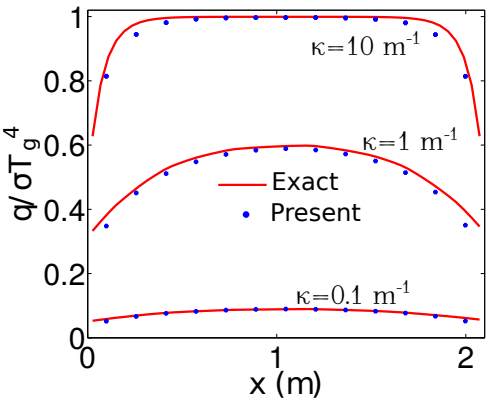

Figure 6.6: Radiative heat flux for the hexahedral enclosure on the wall along the line A-A for three different absorption coefficients.

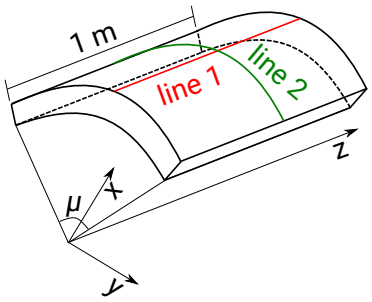

Figure 6.7: Geometry of the annular sector.

absorbing isotropically scattering medium with $\sigma_s = 0.5\,\mathrm{m}^{-1}$, $\kappa = 0.5\,\mathrm{m}^{-1}$ and is kept cold ($T = 0\,\mathrm{K}$) .

Baek et al. [13] studied this problem using the FVM with an angular discretization of 8 x 24 (192 directions) and a spatial mesh of 21 x 21 x 11 points. In the present work it is applied $n = 12$ (168 directions) and the same grid as in Baek et al. [13]. The radial heat flux on the outer wall for $\mu = 30°$ (line 1) and for z = 0.5 m (line 2) as well as the reference data of Baek et al. [13] are shown in Fig. 6.8. Again, for this case the numerical results are in good agreement with the reference.

6.1.6 L-shaped Enclosure

In this test a L-shaped enclosure, shown in Fig. 6.9, is studied. It is filled with an absorbing emitting medium with a temperature of 1000 K. The walls are black and kept at 500 K. This test was presented by Joseph et al. [64]. In their test an unstructured grid of 17192 cells was used and the DOM method S_4 was employed. In the present work a uniform grid consisting of two blocks and 6413 volumes is used and an angular discretization of $n = 4$ is applied.

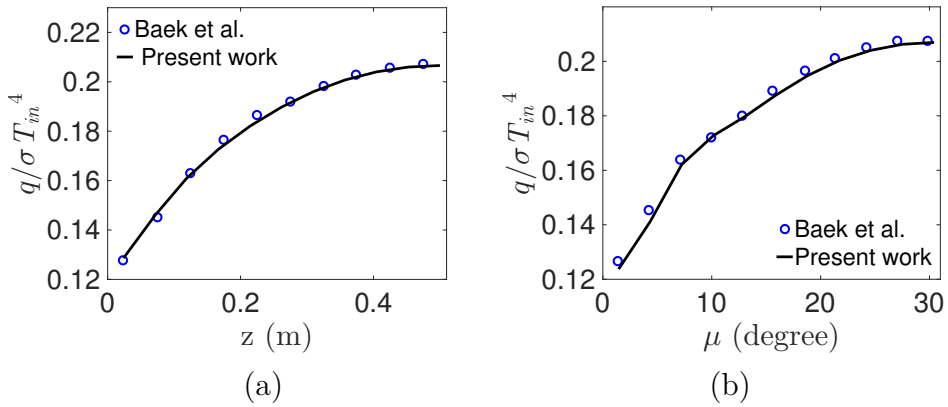

Figure 6.8: Radial heat flux on the outer wall along (a) $\mu = 30^o$ (line 1) and (b) z = 0.5 m (line 2) for the annular sector.

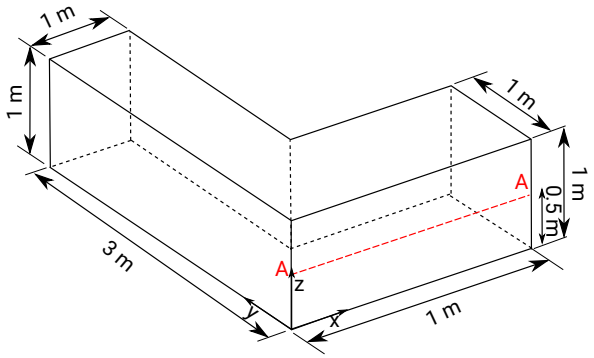

Figure 6.9: L-shaped geometry enclosure.

Four different absorption coefficients are simulated and the heat flux at the line A-A are calculated. The present results together with those found by Joseph et al. [64] are shown in Fig. 6.10. As it has been seen for the previous cases, a good agreement with the reference data is achieved for all adopted absorption coefficients.

6.1.7 Cylindrical Enclosure

In order to verify the implemented solver in a more complex configuration, a cylindrical enclosure, as described in Joseph et al. [65], containing a pure absorbing-emitting gray medium is investigated. The cylinder has a radius of 0.5 m and a length of 3 m. The gray medium inside the enclosure has a temperature of 1200 K while the walls are black and kept at 300 K.

Joseph et al. [65] used an unstructured grid with 210000 tetrahedrals to studied this problem. They calculated the radiative source term S_r and compared the results obtained with two methods: ray tracing with 320000 rays and DOM S_8.

In this work the employed grid has 64000 volumes, consists of 5 blocks and is uniform along the cylinder axis. A radial section of the grid is shown in Fig. 6.11.

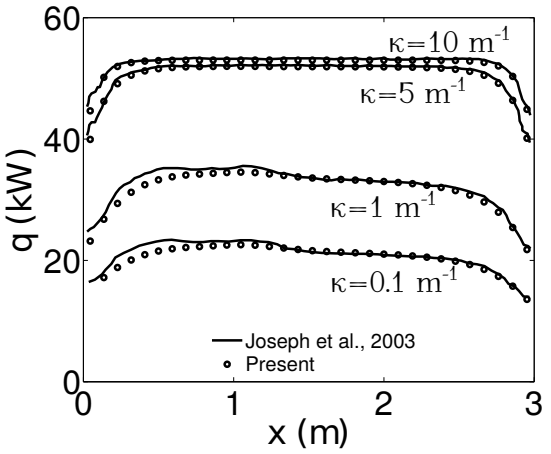

Figure 6.10: Radiative heat flux for the L-shaped enclosure along the A-A line for four different absorption coefficient.

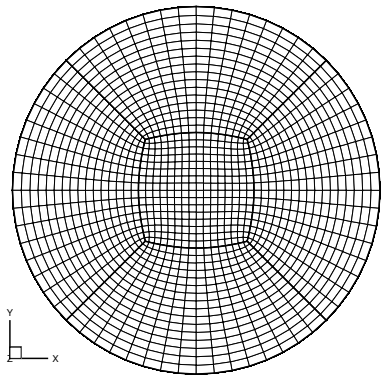

Figure 6.11: Radial section of the grid used for the cylindrical enclosure.

This problem is computed with $n = 8$ and three different absorption coefficients ($\kappa = 0.1\,\mathrm{m}^{-1}$, $\kappa = 1\,\mathrm{m}^{-1}$ and $\kappa = 10\,\mathrm{m}^{-1}$) are tested. The radiative heat source term S_r along the central axis of the cylinder is calculated and plotted in Fig. 6.12. Additionally, the results of Joseph et al. [65] are shown in this plot. It can be noted that also for the cylindrical enclosure the present results are in good agreement with the reference.

6.1.8 Verification of the implemented WSGG Models

As described in Section 5.4 for treating the spectral behavior of the radiatiave intensity the WSGG model is used in this work. Within this model four methods were implemented: gray and nongray models of Johannsson et al. [61], nongray model of Dorigon [41] and nongray model of Bordbar et al. [16]. In the next sections two cases are presented for verifying these implementations. First, a flow with uniform species concentrations are considered, whereas in the second test a flow with heterogeneous species concentration field is assumed.

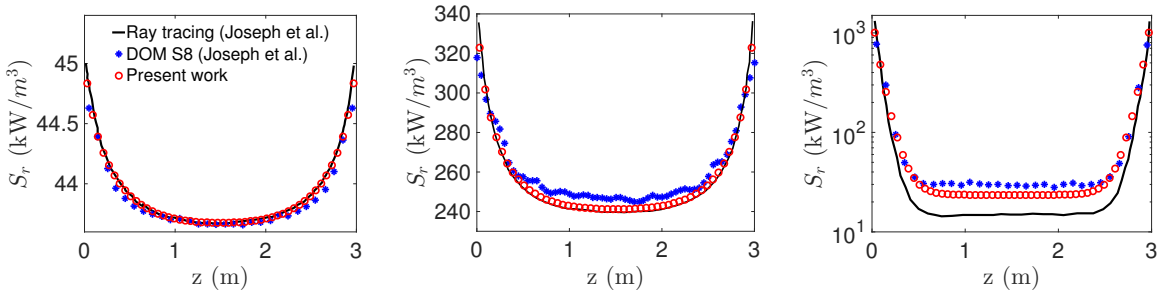

Figure 6.12: Radiative source term along the central axis of the cylinder for (a) $\kappa = 0.1\,\mathrm{m}^{-1}$, (b) $\kappa = 1\,\mathrm{m}^{-1}$ and (c) $\kappa = 10\,\mathrm{m}^{-1}$.

6.1.8.1 Rectangular Box

This case corresponds to the problem studied by Lui [88] and Porter et al. [112]. It consists of a box of dimensions $2\,\mathrm{m} \times 2\,\mathrm{m} \times 4\,\mathrm{m}$ with black walls kept at 300 K. The temperature distribution inside the enclosure is prescribed by Porter et al. [112] as

$$T = (T_c - T_e) f(r) + T_e, \tag{6.4}$$

where T_c corresponds to the temperature in the centerline of the enclosure and T_e to the temperature at the end ($z = 4\,\mathrm{m}$). Moreover, r is the distance to the enclosure centerline and f is a function given by

$$f(r) = 1 - 3r^2 + 2r^3. \tag{6.5}$$

The end temperature T_e is set to 400 K while the temperature in the centerline T_c varies throughout the enclosure following the functions:

$$\begin{aligned} T_c(z) &= 3733.33\, z + 400 \quad \text{for} \quad z \leq 0.375\ , \\ T_c(z) &= -275.86\, z + 1903.45 \quad \text{for} \quad z > 0.375\ . \end{aligned}$$

The temperature field for the plane $y = 1\,\mathrm{m}$ can be seen in Fig. 6.13. The applied mesh in this problem has 17 x 17 x 24 volumes and is uniform in the x and y directions and nonuniform in the z direction according to Lui [88]. In the z direction the points for building the grid are (in meter): 0.04, 0.115, 0.190, 0.265, 0.325, 0.375, 0.425, 0.500, 0.600, 0.725, 0.875, 1.025, 1.200, 1.400, 1.600, 1.800, 2.00, 2.250, 2.550, 2.850, 3.125, 3.375, 3.625 and 3.875.

As in Porter et al. [112] two cases with two different concentrations are studied: air combustion (10 vol.% CO_2, 20 vol.% H_2O) and oxyfuel combustion (85 vol.% CO_2, 10 vol.% H_2O). The radiative source term along line 1 (center line) and the wall heat flow along lines 2 and 3, see Fig. 6.13, are calculated and compared with the benchmark data of Lui [88] (air combustion) and of Porter et al. [112] (oxyfuel combustion). Both benchmark data were obtained using the ray tracing method with T_7 quadrature and the *Statistical Narrow-Band* (SNB) model. In the present work $n = 4$ (24 directions) is

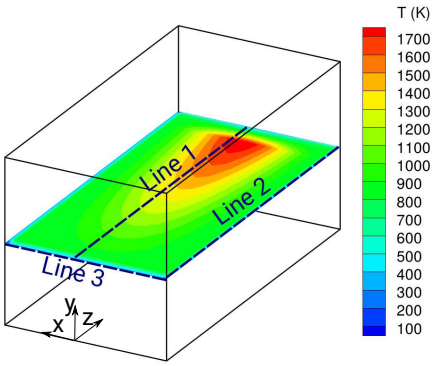

Figure 6.13: Temperature distribution for the rectangular box.

applied.

The comparison for the air combustion case is shown in the top line of Fig. 6.14, which includes the results for the gray and nongray models of Johansson et al. [61], the nongray model of Dorigan et al. [41] and the benchmark data. As expected, the nongray models present a better agreement with the benchmark data. Similar results can be seen for oxyfuel combustion, which are shown in the bottom line of Fig. 6.14. Here, the results using the gray and nongray models of Johansson et al. [61] and the nongray model of Bordbar et al.[16] together with the benchmark data are presented. For the air combustion case, the results obtained with the model of Dorigan et al. [41] are the closest to the benchmark solution, while for the oxyfuel combustion case, the closest results are obtained for the nongray model of Johansson et al. [61].

The difference between the results obtained here and the benchmark data are similar to that found in Porter et al. [112] and in Zhang et al. [146]. Therefore, it can be considered that the implemented WSGG models are successfully verified for this homogeneous species concentrations case.

6.1.8.2 Cylindrical Combustion Chamber

This last case corresponds to a cylindrical combustion chamber studied by Centeno et al. [20]. It has a radius of 0.25 m and a length of 1.7 m. Details about the geometry are presented in Fig. 6.15. Following the authors, the cylinder walls are black and kept at a temperature of 393.15 K

The temperature distribution inside the chamber is given by

$$\begin{aligned} T(z,r) &= c_1 + c_2 r + c_3 z + c_4 r^2 + c_5 rz + c_6 z^2 + c_7 r^3 + c_8 r^2 z + c_9 r z^2 \\ &+ c_{10} z^3 + c_{11} r^4 + c_{12} r^3 z + c_{13} r^2 z^2 + c_{14} r z^3 + c_{15} z^4 + c_{16} r^5 \\ &+ c_{17} r^4 z + c_{18} r^3 z^2 + c_{19} r^2 z^3 + c_{20} r z^4 + c_{21} z^5 \ , \end{aligned} \tag{6.6}$$

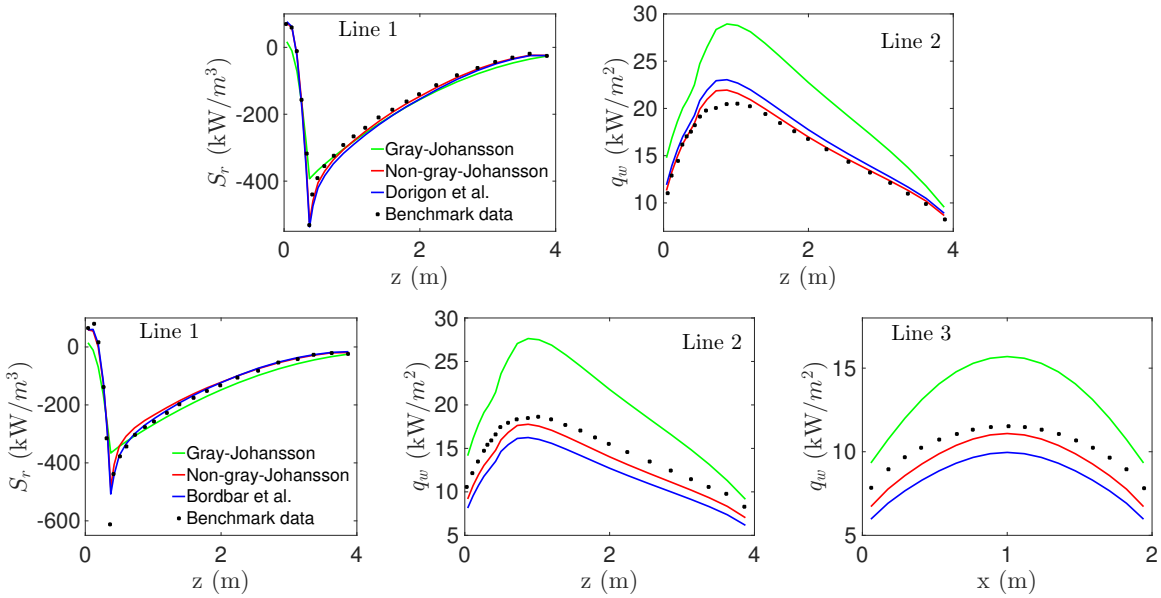

Figure 6.14: Radiative source term along line 1 and wall heat flow along lines 2 and 3 (see Fig. 6.13). Top: air combustion and bottom: oxyfuel combustion. No benchmark data is available for line 3 in the air combustion case.

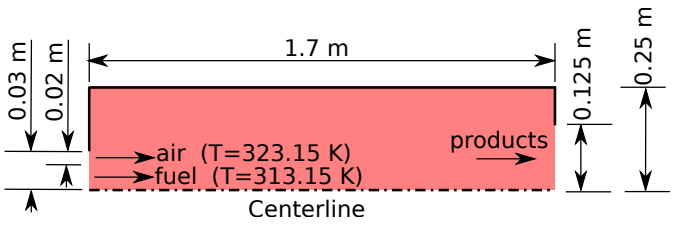

Figure 6.15: Geometry for the cylindrical combustion chamber test.

where the coefficients are presented in Table 6.2. This distribution is valid for the whole chamber and yields the temperature in K, besides that, r and z should be given in meter. As shown in Fig. 6.16(a), the flow is cold in the region close to the entrance of the chamber and the temperature increases towards the chamber outlet.

The H_2O and CO_2 molar distributions are given by the following equations:

$$X_{\mathrm{H_2O}} = a_w \cosh\left[\frac{\pi(r-b_w)}{c_w}\right] \sin\left[\frac{\pi(z-d_w)}{f_w}\right] + g_w \ , \tag{6.7}$$

$$X_{\mathrm{CO_2}} = a_c \cosh\left[\frac{\pi(r-b_c)}{c_c}\right] \sin\left[\frac{\pi(z-d_c)}{f_c}\right] + g_c \ , \tag{6.8}$$

where the coefficients are given in Table 6.2 and, as for the temperature distribution, r and z should be given in meter. The distributions for these two variables are presented in Figs. 6.16(b) and (c). As it can be seen, both concentrations are low in the core of the flow field close to the chamber entrance and increases in the direction of the exit of the chamber.

Table 6.2: Coefficients for the temperature, Eq. (6.6), and chemical species distributions, Eqs. (6.7) and (6.8), as given in Centeno et al. [20] .

c_1 $301.9 \cdot 10^0$	c_2 $-1.032 \cdot 10^4$	c_3 $12887 \cdot 10^0$	c_4 $4.467 \cdot 10^5$	c_5 $22157 \cdot 10^0$	c_6 $-50957 \cdot 10^0$
c_7 $-4.409 \cdot 10^6$	c_8 $-7.247 \cdot 10^4$	c_9 $2.442 \cdot 10^4$	c_{10} $6286 \cdot 10^0$	c_{11} $1.724 \cdot 10^7$	c_{12} $6.402 \cdot 10^5$
c_{13} $-5.288 \cdot 10^4$	c_{14} $-2.765 \cdot 10^4$	c_{15} $-2011 \cdot 10^0$	c_{16} $-2.404 \cdot 10^7$	c_{17} $-1.493 \cdot 10^6$	c_{18} $5.978 \cdot 10^4$
c_{19} $2.257 \cdot 10^4$	c_{20} $7156 \cdot 10^0$	c_{21} $-4.257 \cdot 10^0$	a_w $3.6337 \cdot 10^{-2}$	b_w $2.3154 \cdot 10^{-1}$	c_w $2.8847 \cdot 10^{-1}$
d_w $1.5974 \cdot 10^0$	f_w $2.7637 \cdot 10^0$	q_w $2.0665 \cdot 10^{-1}$	a_c $1.743 \cdot 10^{-2}$	b_c $2.4736 \cdot 10^{-1}$	c_c $3.0427 \cdot 10^{-1}$
d_c $1.5762 \cdot 10^0$	f_c $2.6320 \cdot 10^0$	q_c $2.6858 \cdot 10^{-2}$			

In order to compare the present results with the ones obtained by Centeno et al. [20], profiles of the radiative heat source term along the chamber centerline and along the radial direction at the axial positions $z = 1\,\text{m}$ and $z = 1.5\,\text{m}$ are plotted in Fig. 6.17(a), (b) and (c).

The reference solution was obtained by using DOM S_6 and the nongray WSGG model of Dorigon et al. [41]. Besides that, a 2D axissymmetric grid was used consisting of 50 and 90 cells in the radial and axial directions. In this work a 3D grid consisting of 5 blocks and 172800 volumes is applied, similar to the one shown in Fig. 6.11. Furthermore, in this work the same WSGG model used in Centeno et al. [20] is applied and for the angular discretization $n = 4$ (24 directions) is employed.

Together with the reference solution, two different results obtained in this work are shown in Fig. 6.17. The one referred to as 'Present work 1' uses the wall temperature boundary condition as proposed in Centeno et al. [20], namely $T_w = 393.15\,\text{K}$. 'Present work 2' refers to a case where the wall temperature is set with the value obtained by the polynomial function given in Eq. (6.6) for the corresponding wall position. The profiles for 'Present work 2' are very close to the reference solution. Therefore, it can concluded that the implemented WSGG model based on Dorigon et al. [41] is also verified for this heterogeneous species concentrations case.

6.2 Summary

Various studies were performed in this chapter towards the construction of a radiation solver to be coupled in FASTEST. These studies were shown in the first sections of this chapter, where several tests were described, from simple 2D to relatively 3D complex geometries. Moreover, the models implemented for treating the spectral dependency of

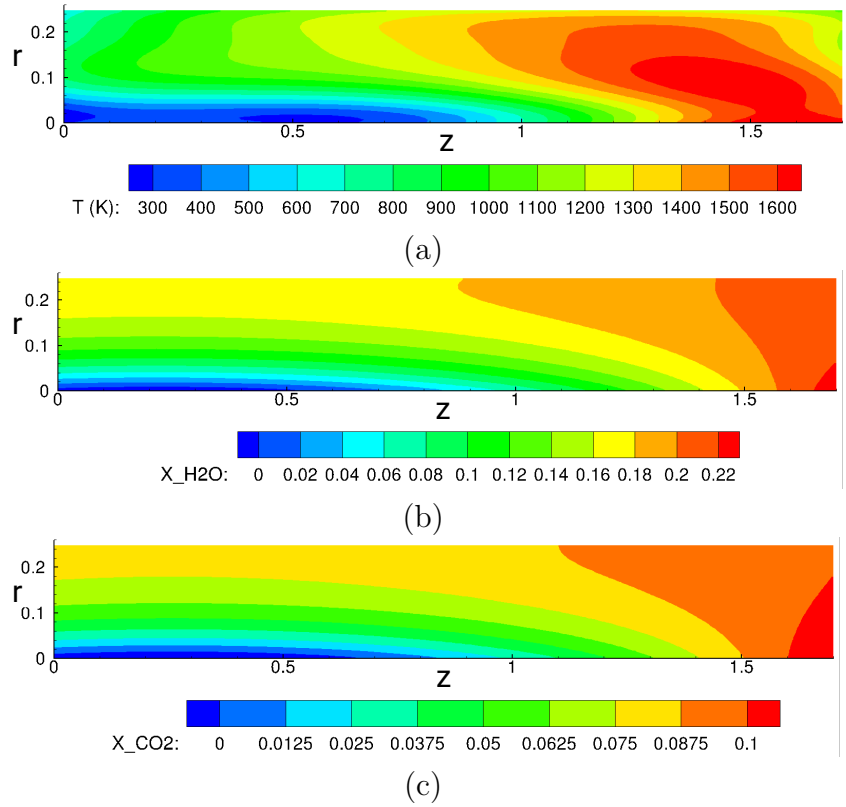

Figure 6.16: (a) Temperature field (b) H_2O and (c) CO_2 mole fraction distributions for the cylindrical combustion chamber case.

the radiative intensity were verified first for a uniform species concentration field, then for a more realistic species concentration distribution. Since all tests presented a good agreement with the reference data, it can be concluded that the implementations are successfully verified.

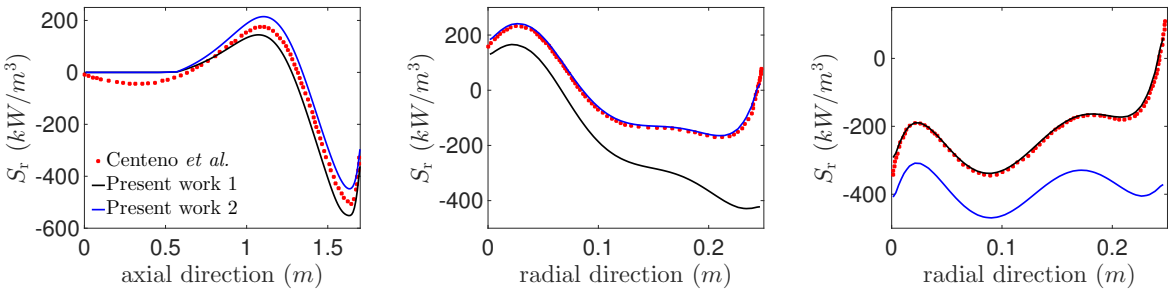

Figure 6.17: Radiative source term for the cylindrical combustion chamber, (a) axial profile at chamber centerline, (b) radial profile at axial position $z = 1\,\mathrm{m}$ and (c) radial profile at axial position $z = 1.5\,\mathrm{m}$.

Chapter 7

Preliminary Investigation: Validation of the Used Models

As a prestep towards performing the investigations with radiative heat transfer in Chapter 8, analyses without the presence of thermal radiation should be carried out. Satisfactory predictions of CO_2, H_2O concentrations and of temperature distribution are a required in order to obtain accurate results with the radiation solver. Therefore, the main objective of this chapter is to validate FASTEST with the Eulerian stochastic field method excluding thermal radiation.

As already mentioned in the introduction, two relevant flame configurations are studied in this work: the Sandia flame D [4, 5] and the bluff-body stabilized nonpremixed flame [1]. The first section of this chapter is dedicated to describe the flame D case, the numerical setup and to present the numerical and experimental results. Similarly, the bluff-body configuration and results are presented in the second section.

7.1 Sandia Flame D

Sandia flame D [4] is a piloted turbulent jet flame of methane burning in air which is part of the *International Workshop on Measurement and Computation of Turbulent Nonpremixed Flames* (TNF) series. This flame is very well documented and has been widely numerically investigated. Scalar data was obtained by employing Raman/Rayleigh with *Laser Induced Fluorescence* (LIF) [14] at Sandia National Laboratories while the velocity fields were measured with *Laser-Doppler Anemometry* (LDA) [122] at TU Darmstadt. The experimental data is available in Barlow and Frank [5]. Besides that, details about experimental methods and measurement uncertainties can be found in Barlow and Frank [14].

7.1.1 Description of the Configuration

The main jet, with a diameter of 7.2 mm (wall thickness = 0.25 mm), consists of a mixture of 25 % methane and 75 % air by volume. It is surrounded by a pilot with an inner diameter of 7.7 mm and an outer diameter of 18.4 mm (wall thickness = 0.35 mm). The

pilot is composed of a burnt methane-air mixture with an equivalence ratio of 0.77 and is surrounded by co-flowing air. A two-dimensional cross-section of the inlet configuration is shown in Fig. 7.1.

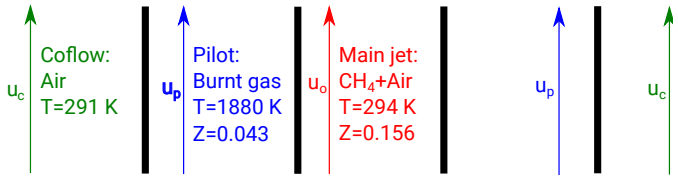

Figure 7.1: Schematic diagram of the inlet configuration for the simulations of the flame D.

At the inlet, the bulk velocity of the main jet is $u_o = 49.6\,\mathrm{m/s}$. It has a temperature of 294 K and a mixture fraction of $Z_o = 0.156$. The pilot is characterized by a bulk velocity of $u_p = 11.4\,\mathrm{m/s}$, a temperature of 1880 K and a mixture fraction of $Z_o = 0.043$. Furthermore, the velocity and temperature of the coflow are $u_c = 0.9\,\mathrm{m/s}$ and $T_c = 291\,\mathrm{K}$.

The corresponding Reynolds number of this flame is $Re = 22400$ based on the nozzle diameter. Moreover, the flame starts burning directly at the inlet between the main jet and the pilot. The burnt gas in the pilot is oxidizer-rich and plays the role of stabilizing the flame. Furthermore, according to Barlow and Frank [5], this flame has burning characteristics of a diffusion flame because the mixing rates are sufficiently high.

The available experimental data covers velocity [122], temperature and species mass fraction, including O_2, H_2O, CH_4, N_2, H_2, CO, OH, CO_2 and NO [4, 5, 14, 15]. It consists of radial profiles at different axial positions, as shown in Fig. 7.2, where at $x/D = 0.14$ only results for the velocity fields are available

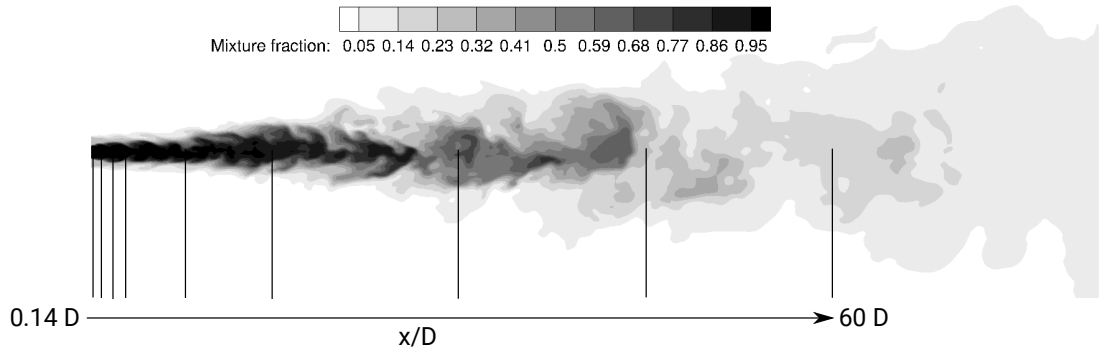

Figure 7.2: Axial positions of the experimental measured lines for the flame D.

7.1.2 Numerical Setup

Two 3D block-structured grids were used, which are referred to as coarse grid and fine grid. The coarse grid consists of 21 blocks and approximately 1.5 million control volumes, see Fig. 7.3. The fine grid includes 437 blocks and about 3.3 million control volumes, which is presented in Fig. 7.4. The size of the control volumes of the coarse grid increases from 0.3 mm in the main jet to approximately 2 mm near to the outlet, whereas the size of the

control volumes of the fine grid varies from 0.17 mm in the main jet to about 2 mm in the vicinity of the outlet. Schematics of the rotationally symmetric computational domains for both grids are shown in Fig. 7.5, where the dimensions are scaled with the diameter of the inner nozzle D. A further difference between the grids concerns an additional $13D$ tube in the upstream region of the main nozzle for the fine grid. This is included to allow the turbulent profiles to develop in the tube. Further, the fine grid is in accordance with the work of Aschmoneit [9] and Jesch [59].

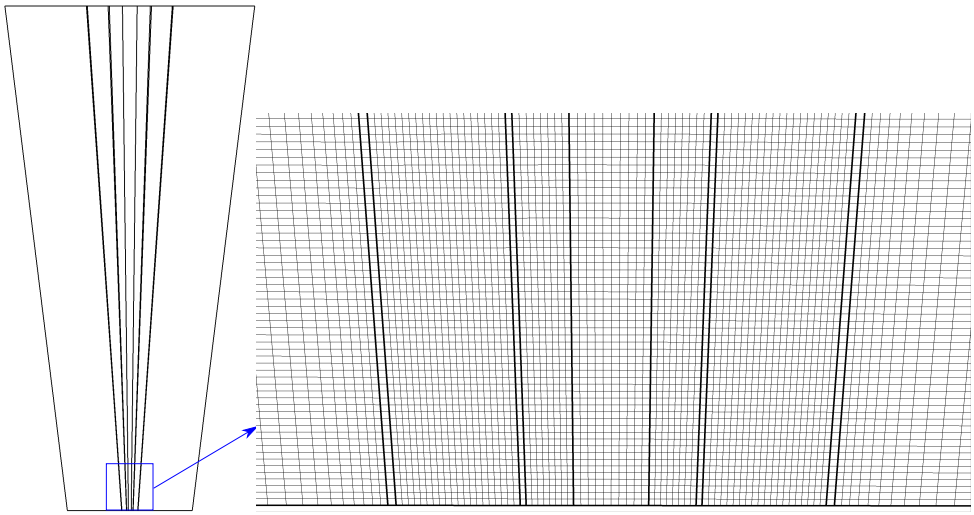

Figure 7.3: Cross section of the coarse grid for the flame D simulations.

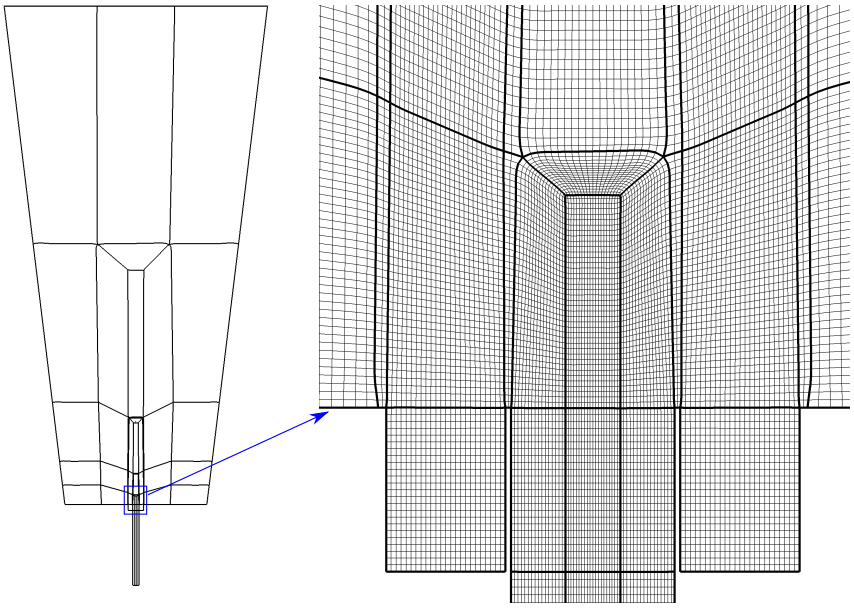

Figure 7.4: Cross section of the fine grid for the flame D simulations.

Because of the two different domains, two different inlet conditions are applied for the main jet and pilot:

- Coarse grid: The inlet axial component of the velocity for the main jet and the pilot is set by interpolating the experimental measured profiles obtained at the

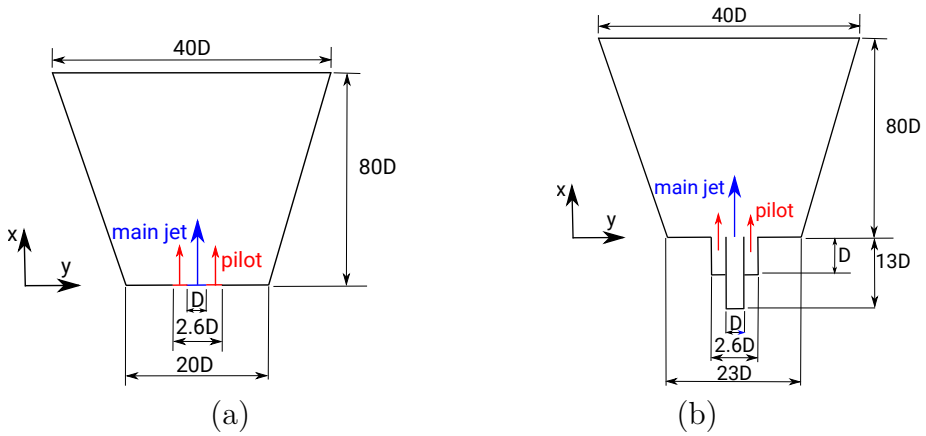

Figure 7.5: Dimensions of the computational domain for the (a) coarse and (b) fine grid.

axial position $x/D = 0.14$ onto the grid at inlet position, whereas the inlet radial component is zero.

- Fine grid: The inlet velocity for the inner nozzle and the pilot is set to obtain a flow field at $x/D = 0.14$ corresponding to the experimental measurements at this position. Therefore, after a parameter study, the axial component of bulk velocities are set to $u_o = 51.9\,\mathrm{m/s}$ and $u_p = 13.0\,\mathrm{m/s}$ for the main jet and pilot, respectively.

For both grids, artificially turbulent fluctuations generated by using the method described by Klein et al. [73] were added to the velocities of the inner nozzle to create a turbulent flow. Surrounding the pilot tube, the coflow velocity is set to $u_c = 0.9\,\mathrm{m/s}$. These inlet conditions results in the velocity profiles shown in Fig. 7.6 for the axial position $x/D = 0.14$. Furthermore, symmetry conditions are applied for the lateral boundaries and a convective condition, following Eq. (4.35) with $U_c = 8\,\mathrm{m/s}$ is employed for the outlet.

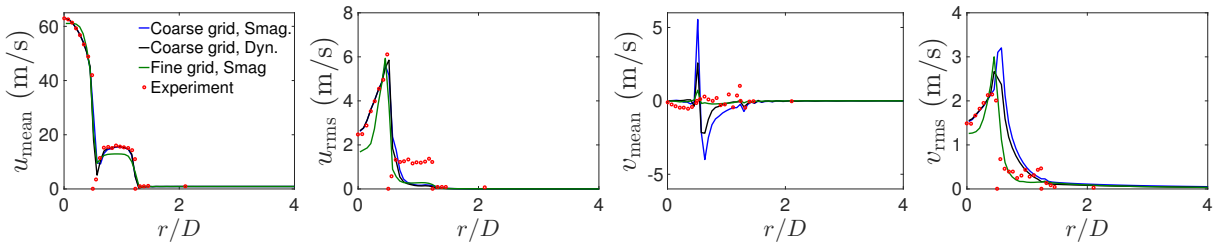

Figure 7.6: Profiles of the mean velocity fields and variance at the axial position $x/D = 0.14$ for the flame D.

For the simulations, 16 Eulerian stochastic fields were used for the joint PDF. As already specified, the mixture consists of 25 % methane and 75 % air, which corresponds to a mixture fraction of $Z = 1$ in the postprocessing, while a mixture with $Z = 0$ refers to pure air. The FGM table used for the simulations was computed with flamelet solutions obtained with the GRI3.0 mechanism [126] and consists of 1001 data points in the mixture fraction, 101 in the progress variable, and 186 in the enthalpy directions. Finally, the mean values were obtained by averaging the instantaneous data in a sampling frequency

of $6.667 \cdot 10^4\,\mathrm{s}^{-1}$ over a period of 0.21 s, corresponding to two flow-through times.

7.1.3 Results

Results for the axial and radial velocity components are shown in Figs. 7.7 and 7.8, where the mean values and their variances are presented for different axial positions. Herein, the numerical results obtained utilizing the fine grid and the coarse grid as well as experimental measurements are plotted. For the coarse grid, two simulations were performed: one by using the Smagorinsky and other with the Germano model. For the fine grid, only the Smagorinsky model is used. In general, the profiles are in good agreement with the experimental results for all simulations.

For $x/D \leq 15$, the results obtained with the fine grid are matching the experimental measurements the best. For higher axial positions, the measurements show a sightly faster decay and spread of the jet compared to the numerical results obtained with this grid. Similar behavior was reported by Aschmoneit [9] and Jesch [59]. Since the rms values for this case are sightly smaller than the measurements at the inlet, as it can be seen in Fig. 7.6, the authors attributed this discrepancy to the fact that the $13D$-long main nozzle is not long enough for the velocity profile to fully develop.

By comparing the results obtained with the coarse grid with the experimental ones, a small deviation can be seen in the axial velocity profile at $x/D = 15$ (Fig. 7.7) and in the radial velocity profiles at $x/D = 15$ and $x/D = 30$ (Fig. 7.8). This discrepancy can be attributed to an insufficient numerical resolution for the jet mixing layers, specially in the region close to the inlet. This is in accordance with Fig. 7.6, where the strong oscillation of the radial velocity component does not correspond to the measurement.

Also the differences in the rms values of the axial velocity profile at the inlet for the pilot region which can be seen for all grids in Fig. 7.6 should be considered as a potential cause for the difference seen in the profiles depicted in Figs. 7.7 and 7.8. As discussed in Jesch [59], setting the boundary conditions properly for the pilot is not straightforward since the pilot is not a simple coflow jet. It consists of a premixed flame ejected through a large number of small holes, which can not be easily numerically reproduced.

The temperature field, shown in Fig. 7.9, is also reasonably well predicted in all simulations. For these profiles, the results obtained with the fine grid are in better agreement with the experimental ones. A relatively small discrepancy is observed for axial positions $x/D = 7.5$, $x/D = 15$ and $x/D = 30$, where the numerical mean temperature is slightly higher than in the measurements. Further, the temperature profiles obtained with the fine grid show an underprediction of jet decay and spread while the results obtained with the the coarse grid show a slightly faster decay and spread of the jet than the measurements.

Fig. 7.10 depicts profiles of the computed CO_2 mass fraction. In line with the above presented fields, a good agreement is demonstrated for both grids, with main discrepancies observed close to the flame tip.

The comparison between the two subgrid stress closure models, Smagorinsky and Germano, is performed because of findings reported in Clayton and Jones [29]. In this work,

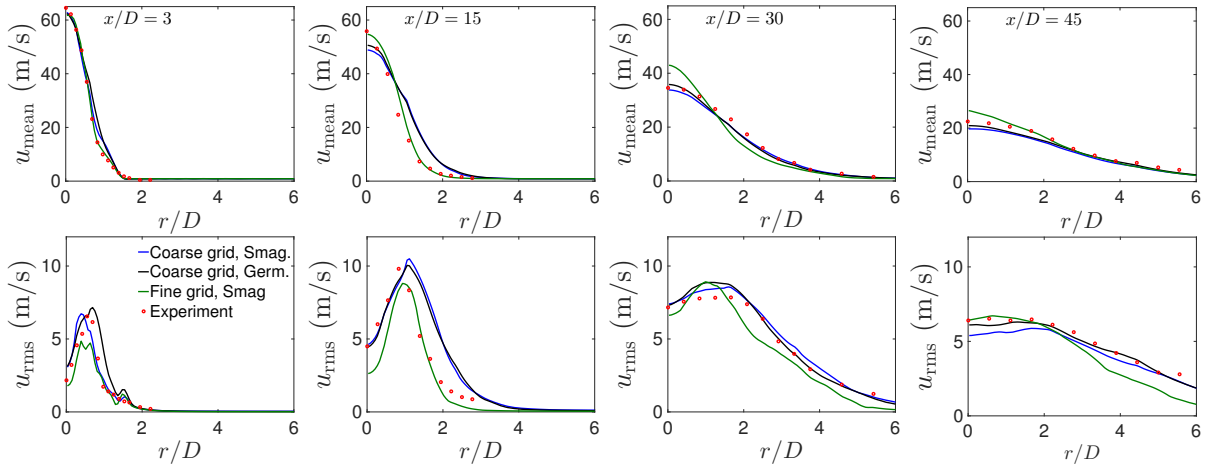

Figure 7.7: Profiles of the mean axial velocity component and its variance at different axial positions for the flame D.

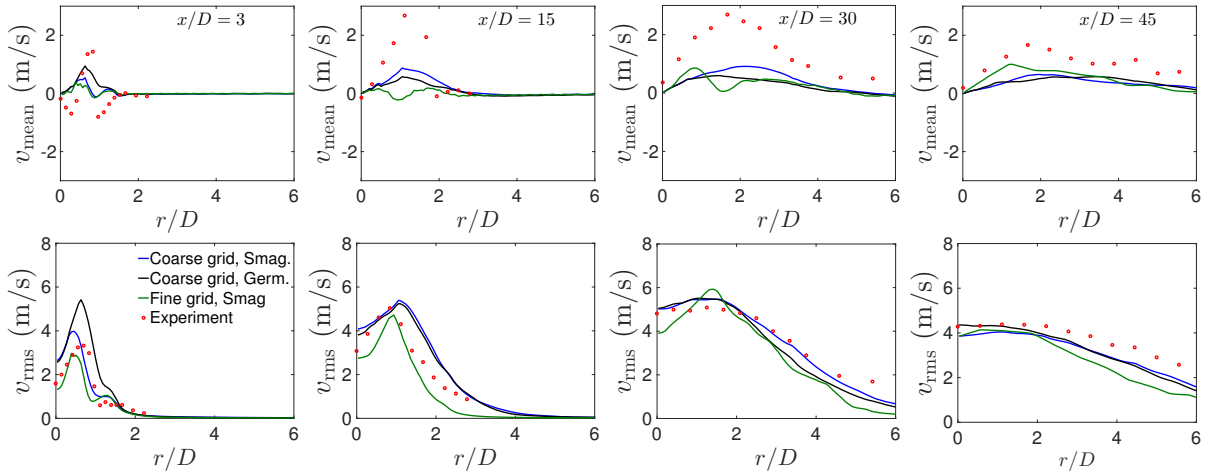

Figure 7.8: Profiles of the mean radial velocity component and its variance at different axial positions for the flame D.

the authors showed that the choice of the subgrid model was extremely influential on the final results for simulating the flame D and reported that the results were more accurately reproduced by applying the Germano model. In the present analysis, the results obtained with the Germano model are indeed in slightly better agreement with the measurements. However, the difference between these two subgrid models is small, as it can be noted in Figs. 7.7-7.10. Because of the similarity of the results obtained with the coarse grid using Smagorinsky and Germano models and to avoid confusion, only the simulations results with the former are considered in the following discussion.

A good agreement between numerical and experimental results is also obtained for the mixture fraction shown in Fig. 7.11(a). Herein, the mean and rms values of the mixture fraction along the centerline are presented. Although small discrepancies are observed, both presented quantities are reproduced reasonably accurately. Additionally, in Fig. 7.11(b) the subgrid-scale contributions are plotted. This result is in agreement with the one obtained by Mustata et al. [99]. As it can be seen in this figure, the subgrid-scale

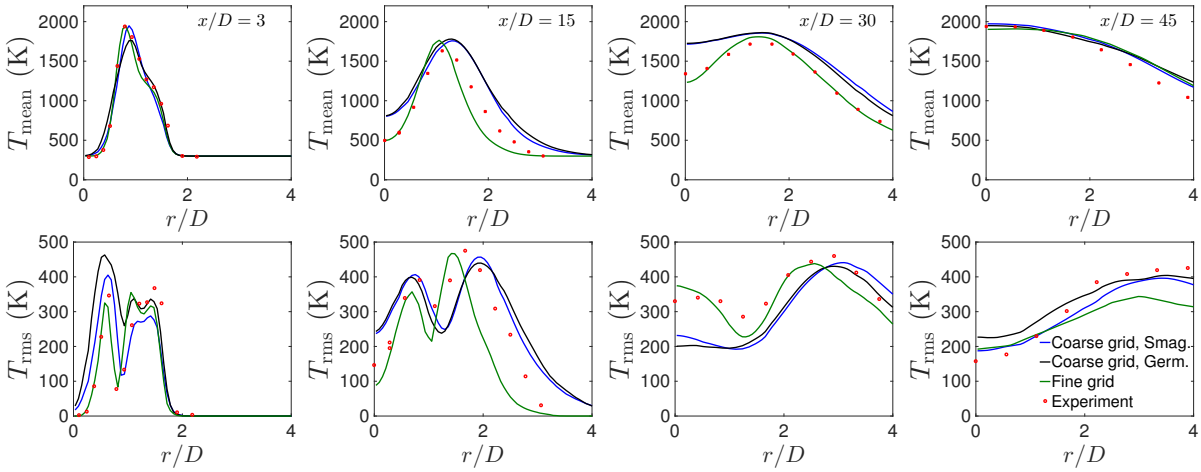

Figure 7.9: Radial profiles for Temperature T at different axial positions for the flame D.

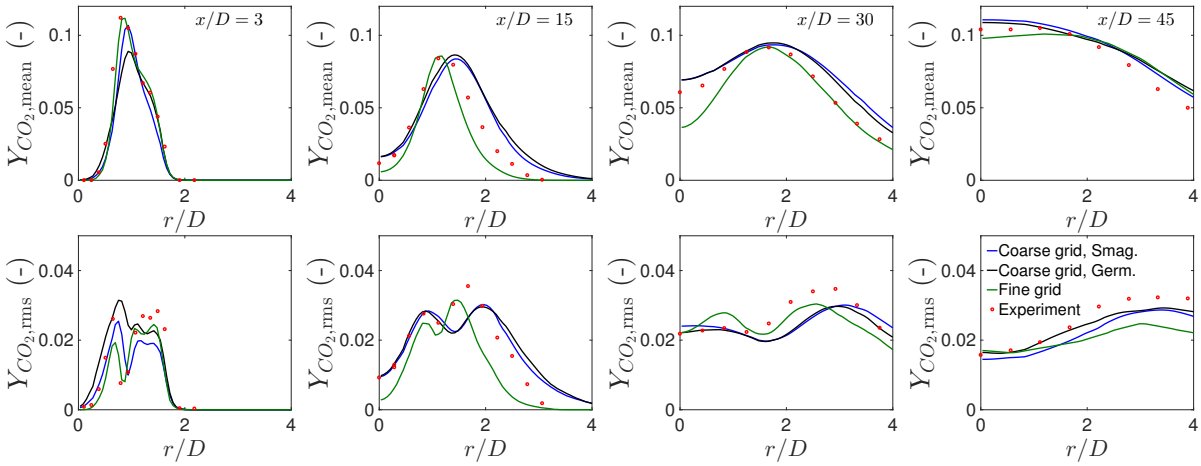

Figure 7.10: Radial profiles for CO_2 mass fraction Y_{CO_2} at different axial positions for the flame D.

contributions are low compared to the rms values. As discussed in Mustata et al. [99], this indicates the major part of the turbulent mixture fraction fluctuation is resolved by the LES.

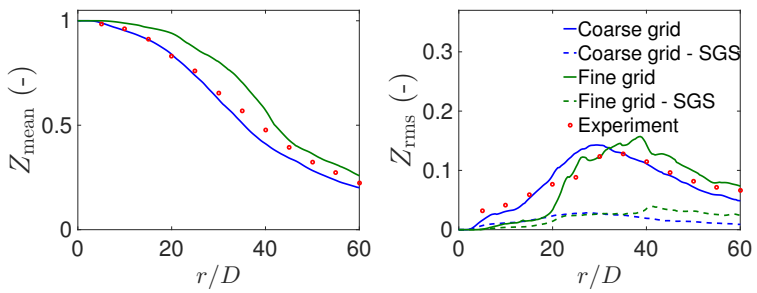

Figure 7.11: Mean and rms values of the mixture fraction Z along the centerline for the flame D.

For the coarse grid, an additional qualitative verification of the calculated mixture fraction subgrid-scales was performed using the ESF method. Therefore, the obtained subgrid-scale variance Z^2_{sgs} is compared to the one obtained with the model proposed by Branley and Jones [17]. This model uses the gradients of the mixture fraction to approximate the subgrid-scale variance as

$$Z^2_{\text{sgs}} \approx C_\Phi \Delta^2 \left(\frac{\partial \widetilde{Z}}{\partial x_i} \frac{\partial \widetilde{Z}}{\partial x_i} \right) , \tag{7.1}$$

with a constant C_Φ within the interval $0.1 \leq C_\Phi \leq 0.2$. As in Jesch [59], in this work this constant is set to $C_\Phi = 0.15$. The results for both fields are presented in Fig. 7.12. On the left side of the figure the subgrid-scale variance obtained with the present ESF model is depicted and the right side shows the field yielded by employing Eq. (7.1). As expected, the values are in the same order of magnitude.

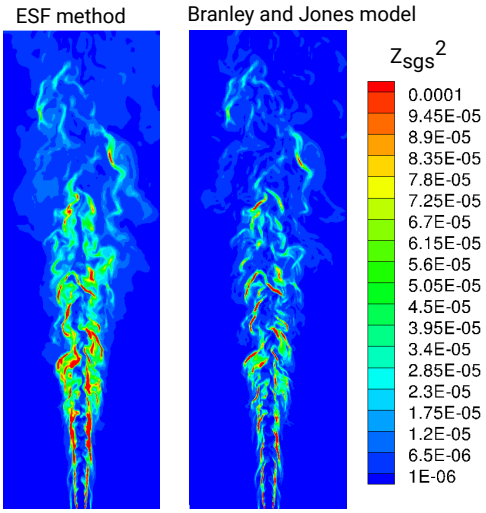

Figure 7.12: Contours of the subgrid-scale variance Z^2_{sgs} by using the ESF method (on the left) and using the model proposed by Branley and Jones (on the right) for the simulation of the flame D using the coarse grid and Smagorinsky model.

The last analysis in this section corresponds to a comparison between the experimental and numerical flame lengths. The mean temperature field together with the line of the stoichiometric value for the mixture fraction of $Z_{\text{st}} \approx 0.055$ for the coarse grid case are depicted in Fig. 7.13. By considering this stoichiometric value, a flame length of $45.8D$ is estimated for the numerical results while the measured valued is $48D$. The same procedure can be applied for the case using the fine grid, resulting in a flame length of about $51D$. These slightly underestimated and overestimated results for the coarse and fine grid occur due to the overprediction and underprediction of jet decay and spread for these simulations, as seen in the mean axial velocity profiles shown in Fig. 7.7.

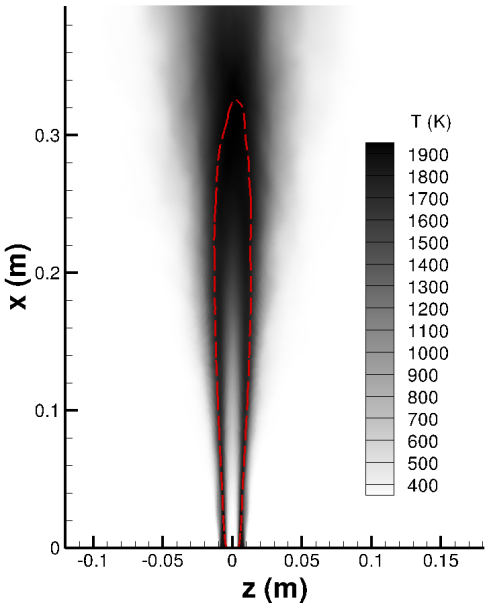

Figure 7.13: Contours of the mean temperature. The red dashed line shows the stoichiometric value for the mixture fraction of $Z_{\mathrm{st}} \approx 0.055$ for the simulation of the flame D using the coarse grid and Smagorinsky model.

7.1.4 Summary

As a prestep for the investigations with thermal radiation, the Sandia flame D was computed in this section without radiation effects and the results were compared with experimental data. Two different grids were employed, one with about 3.3 million control volumes, referred to as fine grid, and second one with approximately 1.5 million control volumes, referred to as coarse grid. For both grids the numerical and reference results were in acceptable accordance. When analyzing the results obtained with the two grids, both presented similar discrepancies compared to the measurements. For this reason, it could not be determined which grid delivered the best results, which in turn suggests that the $13D$-long main nozzle part of the fine grid may not be necessary.

For the simulation using the coarse grid, the subgrid models of Smagorinsky and Germano were applied. The difference between them was small and the results obtained with the Germano model were slightly closer to the measurements.

The subgrid-scale contributions for the mixture fraction were low compared with the rms values, which imply that the major part of the turbulent mixture fraction fluctuation was captured by the LES. In addition, the obtained subgrid-scale variance for this field was compared to the one obtained using the model proposed by Branley and Jones [17] and the value were in the same order of magnitude.

As it can be seen in Fig. 7.6, the rms values of the axial velocity profile at the inlet for the pilot region did not correspond to the experimental values. Therefore, in order to improve the results, the artificially generated turbulent fluctuations added in the inlet velocity of the main jet should be extended to the pilot region, independently of the grid.

In conclusion, the flame D configuration was used as a first validation case for FASTEST. The same numerical setup will be applied for the investigations with radiative heat transfer in Chapter 8.

7.2 Bluff-Body Stabilized Nonpremixed Flame

In addition to the Sandia flame D, the bluff-body configuration is studied in this work, which represents a problem of higher industrial relevance. It consists of a turbulent nonpremixed flame stabilized on an axisymmetric bluff-body burner, referred to as HM1e configuration, which is also part of the TNF series. Furthermore, it is also a very well documented and widely studied flame. The data of the experimental results are available in [1]. The measurements were taken of two different test rings (HM1e and HM1). For HM1e, in which $u_c = 35\,\mathrm{m/s}$ and $u_j = 108\,\mathrm{m/s}$, only velocity data is available. Moreover, only scalar data exist for the configuration HM1, in which the inlet velocities were slightly higher ($u_c = 40\,\mathrm{m/s}$ and $u_j = 118\,\mathrm{m/s}$). This difference in the inlet velocities for the two rings can be explained by the impossibility of generating a constant velocity within the used wind tunnel. Raman/Rayleigh scattering combined with LIF were used to obtain the scalar measurements, while velocity fields were obtained using LDA and *Particle Image Velocimetry* (PIV). According to Kempf et al. [69] and Kuan and Lindstedt [75], both measured flames are at 50 % of the respectively blowoff velocity and present similar flow and scalar characteristics.

7.2.1 Description of the Configuration

The schematic of the burner is given in Fig. 7.14. The cylindrical bluff-body with diameter $D = 50\,\mathrm{mm}$, which is surrounded by a coaxial coflow, is placed inside a square wind tunnel with an edge length of $D = 150\,\mathrm{mm}$. The coflow consists of pure air at atmospheric pressure and temperature $T = 300\,\mathrm{K}$ and plays the role of oxidizer and shield, by protecting the flame from the surrounding laboratory air. The fuel, which corresponds to a mixture of 50 % methane and 50 % hydrogen by volume, is injected through a cylindrical hole with a diameter of $d_j = 3.6\,\mathrm{mm}$. The fuel has the same temperature and pressure as the coflow.

At the inlet, the coflow velocity is $u_c = 35\,\mathrm{m/s}$ while the fuel velocity is $u_j = 108\,\mathrm{m/s}$, corresponding to a Reynolds number of 15800. Furthermore, the flame is stabilized in this configuration due to the recirculation of hot burnt gases, close to the bluff-body top surface, which preheats the incoming fuel.

The available experimental data covers velocity, temperature and species mass fraction, including O_2, H_2O, N_2, H_2, CO, OH, CO_2 and NO. It consists of radial profiles at different axial positions, as shown in Fig. 7.15.

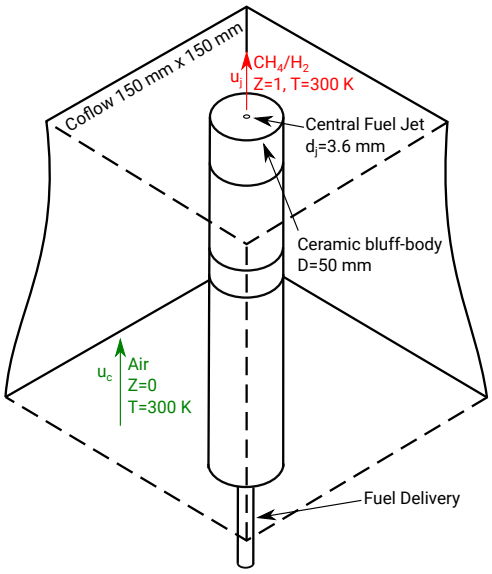

Figure 7.14: Schematic configuration of the bluff-body burner. Figure adapted from [1].

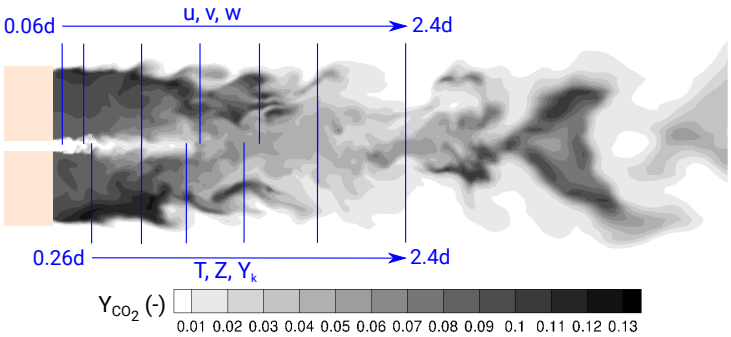

Figure 7.15: Axial positions of the experimental measured profiles for the bluff-body.

7.2.2 Numerical Setup

The numerical setup for this case, including the grid, is similar to those used by Ketelheun [71] and Jesch [59], where this configuration were studied by using the code FASTEST with FGM and PDF methods for accounting the TCI. A 3D block-structured grid consisting of 56 blocks and approximately 1.7 million control volumes is used for the simulations. The size of the control volumes of the grid increases from 0.1 mm in the fuel jet to approximately 2 mm close to the outlet. A cross-section of the grid is shown in Fig. 7.16, where the dimensions are scaled with the diameter of the bluff-body D. The domain has a length of $6.2D$, a width of $3D$ and a bluff-body with height D inserted centrical in the domain.

The boundary conditions corresponding to HM1e case are applied at the inlets. Additionally, as for the flame D, artificial turbulent fluctuations generated by using the method developed by Klein et al. [73] were imposed in the coflow inlet. According to Kempf [68] and Jesch [59], the effects of turbulence should be considered in this inlet since the flow around the edge of the bluff-body is influenced by the boundary layer of the bluff-body.

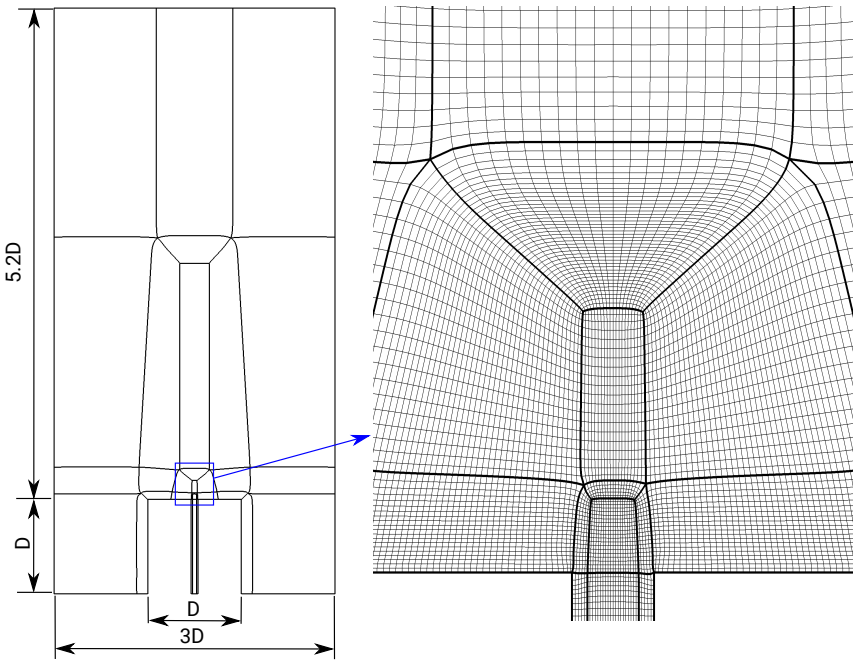

Figure 7.16: Cross section of the grid for the bluff-body case with the dimensions of the computational domain.

The averaged temperature of $T = 953.15\,\mathrm{K}$ was measured in the top plane of the bluff-body. For the simulation, this boundary is set as an isothermal wall by applying Dirichlet condition. Besides that, no-slip condition is enforced to the bluff-body surface and the convective condition following Eq. (4.35) with $U_c = 37\,\mathrm{m/s}$ is used for the outflow.

Unlike the previous case, the fuel for this configurations is a mixture of methane and hydrogen. Therefore, a different FGM table is used for this case which is however featuring the same characteristics as flame D, namely 1001 data points in the mixture fraction, 101 in the progress variable, and 186 in the enthalpy direction. Besides that, the Germano model is used as subgrid model. Finally, the mean values were obtained by averaging the instantaneous data in a sampling frequency of $6.25 \cdot 10^5\,\mathrm{s}^{-1}$ over a period of $0.016\,\mathrm{s}$, corresponding to two flow-through times.

7.2.3 Results

In this section the numerical results are compared with the measurements. As explained above, the velocity fields obtained in test ring HM1e are used for comparison while the scalar properties (mixture fraction, temperature and species mass fraction) are compared to the data resulted from test ring HM1.

Figs. 7.17 and 7.18 show the numerical and experimental radial profiles for the mean axial and radial velocity components. Differences can be noted in the results, specially for the mean axial velocity at axial position $x/D = 1.4$ where the profile is slightly underpredicted in the centerline area. Although the profiles for the region close to the bluff-body are in excellent agreement with the measurements, the jet decay and spread

are slightly overpredicted. Such behavior was also reported in Jesch [59], Olbricht [101] and Kempf et al. [69]. This is also confirmed by analyzing the radial velocity profiles of Fig. 7.18 at higher axial positions, where the absolute radial velocity is underestimated.

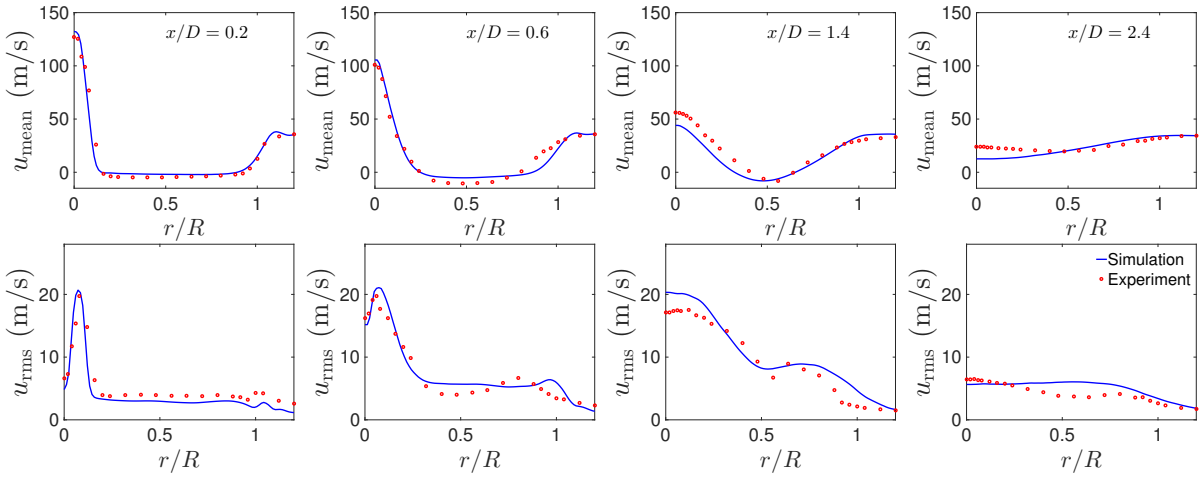

Figure 7.17: Profiles of the mean axial velocity component and its variance at different axial positions for the bluff-body flame.

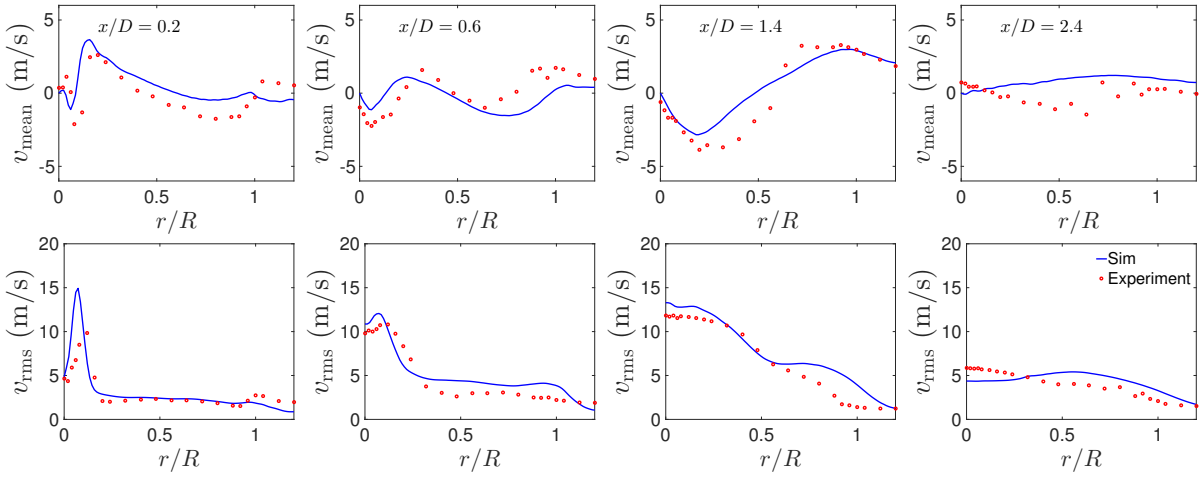

Figure 7.18: Profiles of the mean radial velocity component and its variance at different axial positions for the bluff-body flame.

The same behavior can be observed for the mixture fraction profiles, depicted in Fig. 7.19. For axial position $x/D = 1.3$ the jet mixture is already slightly diluted, and this effect are for axial position $x/D = 2.4$ even stronger, indicating a too short jet. In Fig. 7.19, in addition to the mean and rms values of the mixture fraction, the mean subgrid-scale variance profiles are presented. As for the flame D case, subgrid-scale contributions are low compared with the rms values.

As it can be seen in Fig. 7.20, significant discrepancies appear for the temperature profiles already at axial position $x/D = 0.9$ which confirms, once again, that the jet is too short. This deviations were already expected from the inaccuracies in the mixture-fraction field. In line with the temperature field, the CO_2 mass fraction profiles shown in Fig. 7.21 also

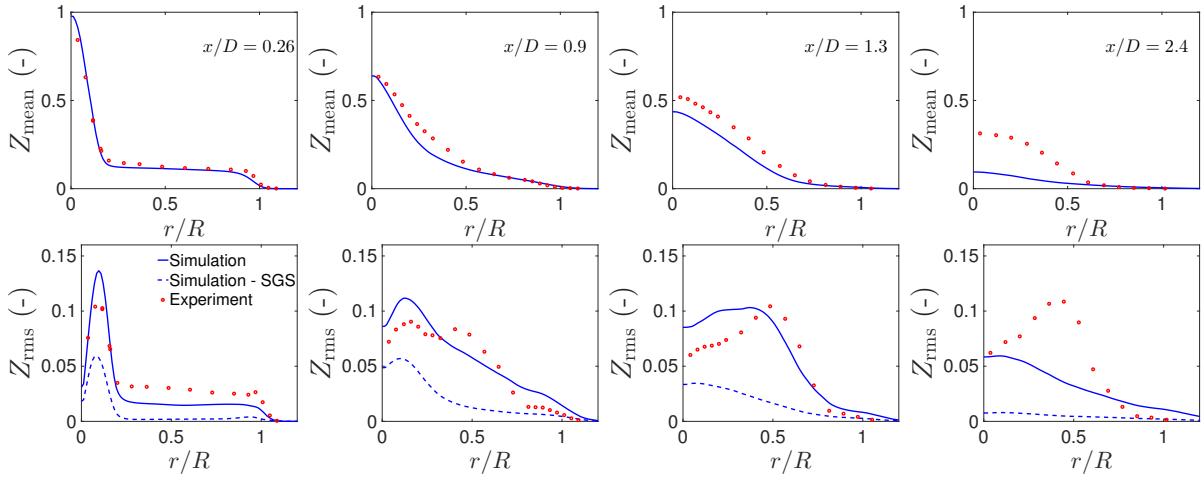

Figure 7.19: Radial profiles for the mixture fraction at different axial positions for the bluff-body flame.

present an significant difference compared to the experimental results. As reported in Jesch [59] and Ketelhen [71], the observed overprediction for this field partly comes from the limitations of the applied reduced chemical scheme and the tabulations.

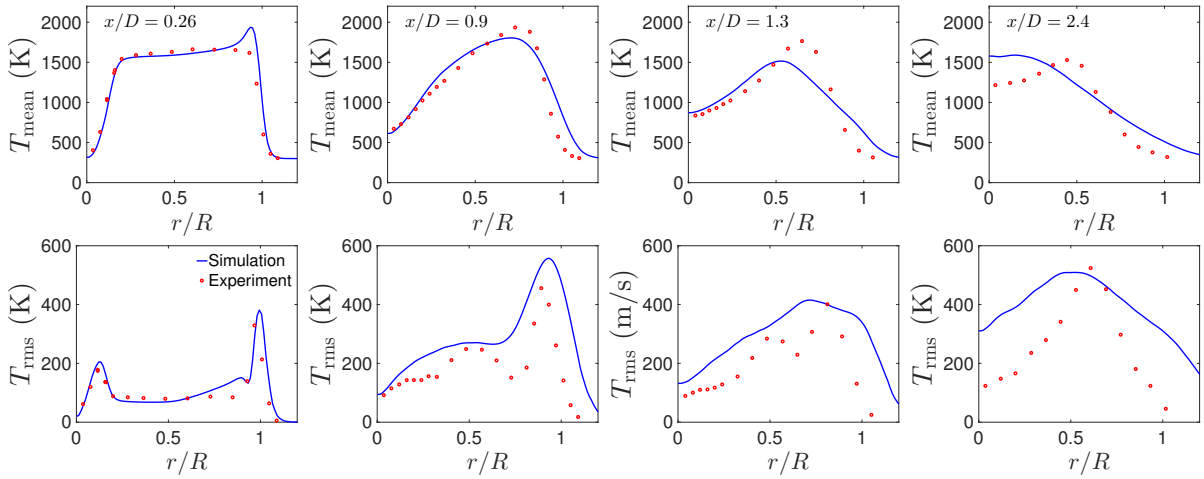

Figure 7.20: Radial profiles for the Temperature T at different axial positions for the bluff-body flame.

As for the previous configuration, the mixture fraction subgrid-scale variance obtained with the ESF method is verified against the model developed by Branley and Jones [17], in which the variance is calculated following Eq. (7.1) with $C_\Phi = 0.15$. As depicted in Fig. 7.22, the variance fields for both methods are in the same order of magnitude.

7.2.4 Summary

The bluff-body diffusion flame was computed in this section without considering radiation effects and the numerical results were compared with the measurements. The numerical

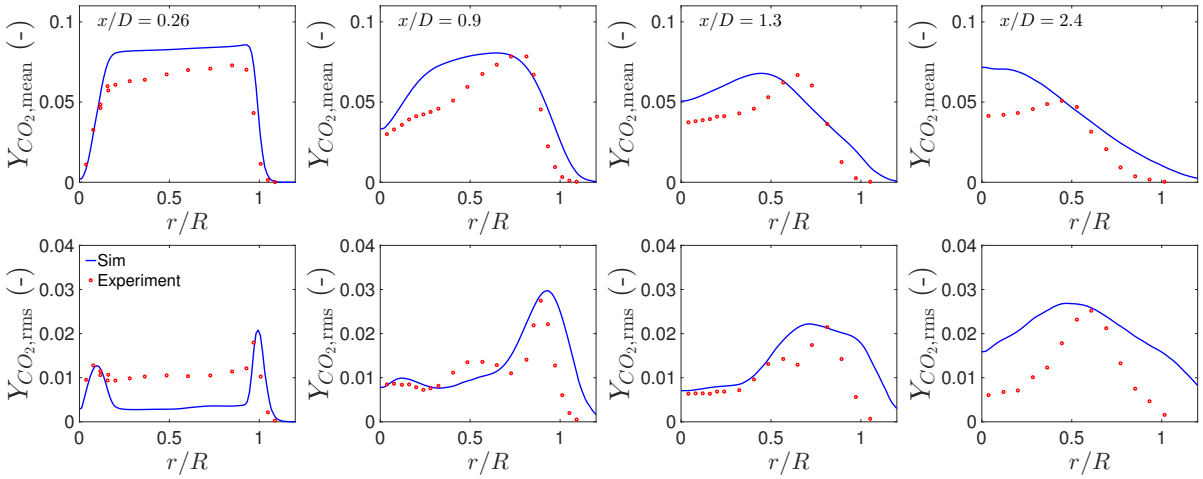

Figure 7.21: Radial profiles for CO_2 mass fraction Y_{CO_2} at different axial positions for the bluff-body flame.

setup and grid for this case are in agreement with the simulation presented in Jesch [59]. The radial profiles for velocity, mixture fraction, temperature and CO_2 mass fraction were plotted together with the experimental results. Some difference appeared in the centerline region, specially for higher axial positions but, by taking into consideration the complex flow field studied, the numerical results are in general encouraging. Moreover, similar discrepancy in the results was reported in Jesch [59], Olbricht [101], Ketelheun [71] and Kempf et al. [69].

As for the flame D, when compared with the rms values, the subgrid-scale contributions for the mixture fraction were also small. Moreover, the subgrid-scale variance obtained with ESF method was compared with the variance calculated using the model proposed by Branley and Jones [17]. The fields were in concordance, indicating a reliable computation with the ESF.

Finally, it can be concluded that FASTEST also delivers satisfactory results for this bluff-body flame configuration. The simulations with radiative heat transfer will be performed by applying the same numerical setup used in this section.

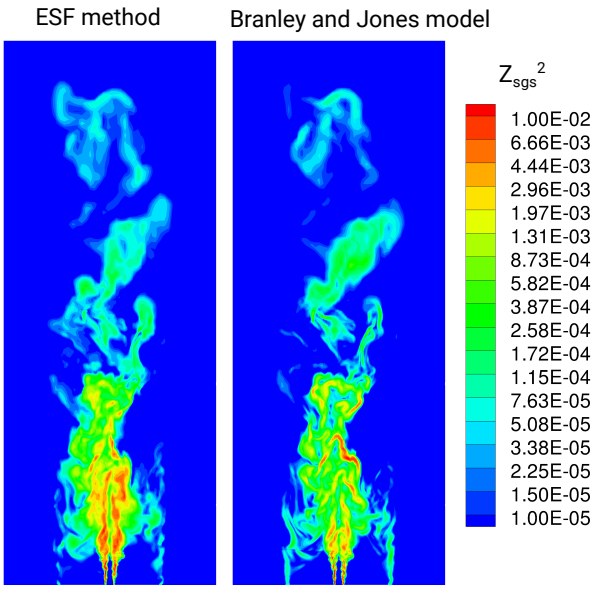

Figure 7.22: Contours of the subgrid-scale variance Z^2_{sgs} by using the ESF method (on the left) and with the model proposed by Branley and Jones (on the right) for the bluff-body configuration.

Chapter 8

Results

In this chapter a study about the *Turbulence-Radiation Interactions* (TRI) in the context of LES is presented. As seen in Section 5.7, in order to compute the filtered radiative source term in the LES framework, the contribution of the resolved scales can be explicitly calculated, whereas the terms involving the subgrid-scales are unclosed and need to be approximated. The importance of the subgrid-scales for the prediction of two relevant turbulent flame configurations is discussed in this chapter. For this aim, the implemented radiation solver is applied for investigating the Sandia flame D [4, 5] and the bluff-body stabilized nonpremixed flame [1].

The Sandia flame D is a small nonluminous flame and the radiative heat transfer occurs on this configuration mainly due to emission and absorption by the gases involved. Besides that, it is known that small flames only lose small quantities of energy through thermal radiation [96]. For this reason, in order to have more pronounced radiation effects, studies about the artificially scaled flame D are commonly found in the literature [86],[141],[50],[51],[103]. Therefore, the four times scaled flame D is additionally investigated in this work. In addition, this idea of artificially scaling the configuration for enhancing the radiation effects is applied for the bluff-body flame.

As described in Section 5.7, four different methods are used for approximating the emission radiative source term $\overline{S}_{\mathrm{r,emission}}$. The first method, called method 0, corresponds to the computation of this term for RANS simulations. The second approximation, method 1, computes $\overline{S}_{\mathrm{r,emission}}$ by employing the instantaneous filtered values, without considering the subgrid values. For the method 2, the subgrid contribution is partially considered. Finally, in the method 3 the subgrid-scale contributions are completely taken into account. Table 8.1 summarizes all these different approximations. Furthermore, as explained in Section 5.7, the absorption radiative source term is approximated with the *Optically Thin Fluctuation Assumption* (OTFA).

For the simulations of both flame configurations, the nongray WSGG model of Dorigon et al. [41] is applied and $n = 8$ is used for the angular discretization, which corresponds to 80 directions.

Table 8.1: Methods used for approximating the filtered emission radiative source term.

Reference name	Emission radiative source term
method 0	$\int_0^\infty 4\pi\kappa_\nu(\langle T\rangle,\langle X_{\text{species}}\rangle)I_{b\nu}(\langle T\rangle^4)\mathrm{d}\nu$
method 1	$\int_0^\infty 4\pi\kappa_\nu(\overline{T},\overline{X}_{\text{species}})I_{b\nu}(\overline{T}^4)\mathrm{d}\nu$
method 2	$\int_0^\infty 4\pi\kappa_\nu(\overline{T},\overline{X}_{\text{species}})I_{b\nu}(\overline{T^4})\mathrm{d}\nu$
method 3	$\int_0^\infty 4\pi\overline{\kappa_\nu(T,X_{\text{species}})I_{b\nu}(T^4)}\mathrm{d}\nu$

8.1 Sandia Flame D

A description of the flame D and its numerical setup used in this work were already discussed in Section 7.1, where this case was computed without radiation effects. In the present chapter these effects are taken into account and the relevance of the TRI is quantified for this flame and for the artificially scaled flame D.

The flame optical thickness is an important parameter for radiative heat transfer. It is defined as

$$\tau_f = \kappa L \ , \tag{8.1}$$

where κ is the absorption coefficient and L corresponds to the flame length. The larger is the flame optical thickness, the stronger are the radiation effects. Therefore, based on the Sandia flame D, an artificially scaled flame is derived by quadrupling the domain and in order to keep the same Reynolds number, the velocities at the inlet are divided by four. The more pronounced radiation effects in the scaled flame can be clearly seen in Fig. 8.1, where the mean temperature profile along the axial jet center line for the flame D and scaled flame, computed by considering and ignoring thermal radiation, are plotted. The continuous lines correspond to the flame D simulations, while the dashed lines represent the results for the scaled flame. The profiles obtained for the simulation of the flame D by considering and ignoring radiative heat transfer are very similar, with a maximum difference at the peak of approximately 50 K. On the other hand, for the scaled flame, the difference between the profiles obtained by considering and ignoring thermal radiation is more evident (about 300 K). In addition, it is worth to remember that the same chemical mechanism is applied for the scaled flame, which corresponds to an increase in the Damköhler number by a factor of 16.

The simulations are carried out for coupled and noncoupled analyses. In the first case, the radiation effects alter the enthalpy and in the latter case, fields of the simulation

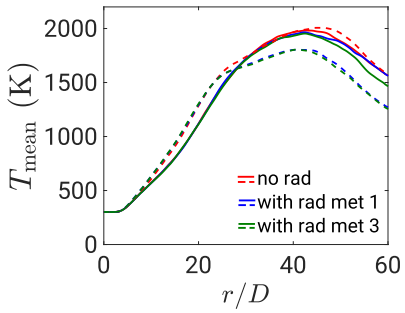

Figure 8.1: Temperature profiles along the jet axial center line for the flame D (continuous lines) and scaled flame (dashed lines).

without radiation are used for calculating the radiative source term. Furthermore, all the results shown in this chapter are obtained with the coarse grid by using the Smagorinsky model. As seen in Section 7.1, the results obtained by using this model are very similar to those obtained with the Germano model, for this reason only one of them is shown here. The frozen analyses were also performed with the fine grid and the results can be found in Miranda et al. [93]. The same grid and CFL number are used for both simulations. Besides that, the radiation source term is updated at a frequency of $f_{rad} = 6.667 \cdot 10^4\,\mathrm{s}^{-1}$.

The grid size for the coarse grid along the axial positions $x/D = 30$ and $x/D = 45$ was analyzed by employing the Kolmogorov length scale as a reference. As in Coelho [34], this parameter was estimated based on experimental data for flame D from Schneider [122], Barlow [4] and Zheng et al [148]. The ratio of the grid size in those positions to the Kolmogorov length does not exceed the value of 12, except in the region far from the flame edge, where the radiative source term is very small.

8.1.1 Noncoupled Simulations

Fig. 8.2 shows the mean CO_2 and H_2O mole fraction distributions, temperature field and radiative heat source term for the flame D. In high temperature regions, which also have an abundance of radiating gas species, the radiative source term (Fig. 8.2 (d)) is negative, which indicates heat losses in these regions. On the other hand, regions where the temperature, CO_2 and H_2O species concentrations are low have a positive radiative source term.

For the case of the scaled flame, profiles of the radiative source term at three different axial positions for the frozen analyses are presented in Fig. 8.3. As it can be seen, the profiles for the method 0 differ significantly from the remaining methods. This result evidences the importance of the TRI effects for RANS and this is in agreement with investigations done in [86], [103] and [141]. By comparing the profiles plotted for methods 1, 2 and 3, no significant difference can be seen among them.

The contribution of emission and absorption to the total radiative heat source term for methods 1 and 3 can be seen in Fig. 8.4. Again, no visible difference can be observed between these two methods even by analyzing the contributions separately. As expected,

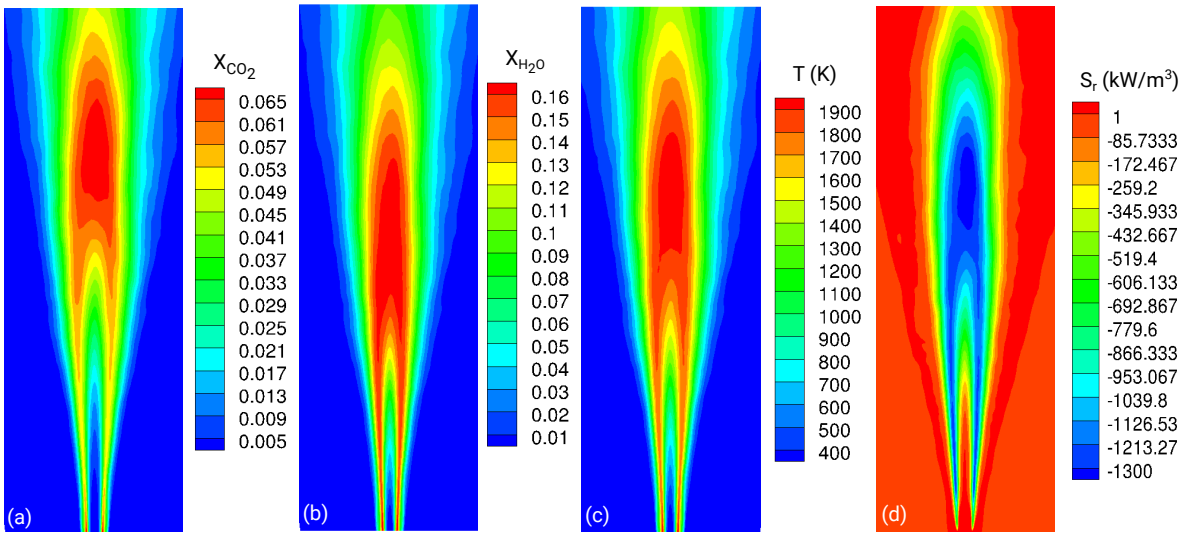

Figure 8.2: Mean distributions of (a) CO_2 mole fraction, (b) H_2O mole fraction, (c) temperature and (d) radiative heat source term for the flame D calculated with the frozen fields.

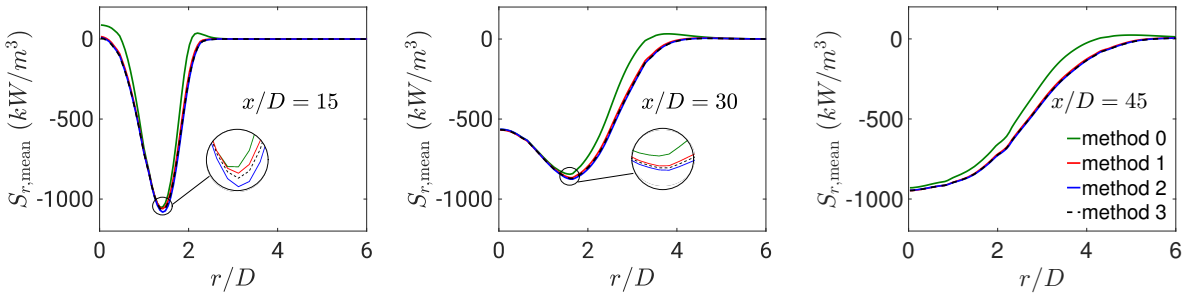

Figure 8.3: Mean radiative heat source profiles for the scaled flame D with different TRI treatments calculated with the frozen fields.

the corresponding results for Sandia flame D, which are shown in Appendix A, also do not present significant difference among the different methods.

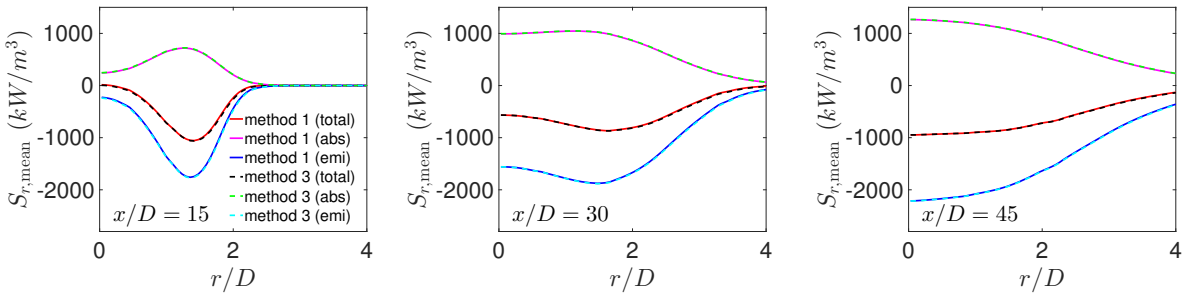

Figure 8.4: Mean radiative heat source profiles for the scaled flame D showing the absorption and emission contributions calculated with the frozen fields.

The mean emission term for methods 1 and 3 for the scaled flame is plotted in Fig. 8.5 (a). As it can be seen, the profiles for both methods overlap for the three different axial

positions. In order to quantify the difference between these two methods, the relevance of the emission term on TRI is calculated as

$$R_{kI_b} = \frac{\langle \sum_i^{\mathcal{I}} \overline{\kappa}_i a_i(\overline{T}) I_b(\overline{T}) \rangle}{\langle \sum_i^{\mathcal{I}} \overline{\kappa_i a_i I_b} \rangle} , \tag{8.2}$$

where $\langle\rangle$ expresses a time averaging. Fig. 8.5 (b) shows this term for the three different axial positions. For significant values of the emission term in Fig. 8.5(a), R_{kI_b} is close to unity for all plotted axial positions. Only for small values of the emission term, the relative discrepancy of method 1 and 3 increases. If one restricted the analysis to values, where the emission term is higher than 1% of its maximum, R_{kI_b} reaches values about 0.85, 0.91 and 0.97 for axial positions $x/D = 15$, $x/D = 30$ and $x/D = 45$. Moreover, it is also worth to point out that R_{kI_b} is less than or equal to one for any radial position. This indicates that, although the difference is small, the emission term calculated omitting the subgrid-scales is underestimated.

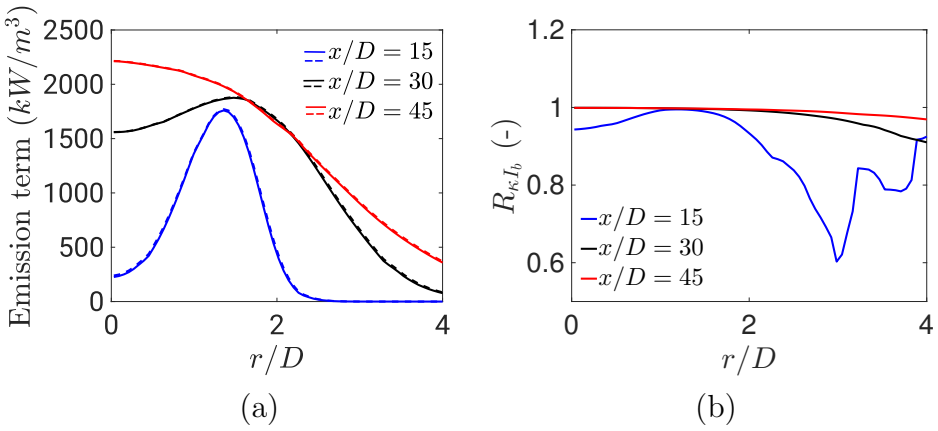

Figure 8.5: (a) Mean emission radiative term calculated with the frozen fields of the scaled flame D for methods 1 (dashed lines) and 3 (continuous lines). (b) Quantification of the emission term on TRI by employing Eq. (8.2).

A similar analysis is done for the blackbody radiative intensity. Fig. 8.6(a) shows the mean blackbody radiative intensity for the scaled flame. As for the emission term, the difference between the method 1 and 3 is small. Additionally, the relevance of the radiative intensity self-correlation is quantified as follows

$$R_{I_b} = \frac{\langle I_b(\overline{T}) \rangle}{\langle \overline{I}_b \rangle} , \tag{8.3}$$

and plotted in 8.6(b). As for the previous analysis, the values of R_{I_b} are close to one for significant values of blackbody radiative intensity and slightly decrease for small values of this quantity. If one considered only values, where the blackbody intensity is higher than 1% of its maximum, R_{I_b} reaches values about 0.84, 0.90 and 0.95 for axial positions $x/D = 15$, $x/D = 30$ and $x/D = 45$.

The results for the fine grid reported in Miranda et al. [93], demonstrate the same behavior as for the coarse grid shown above, i. e., the difference among the methods 1,2 and 3 is

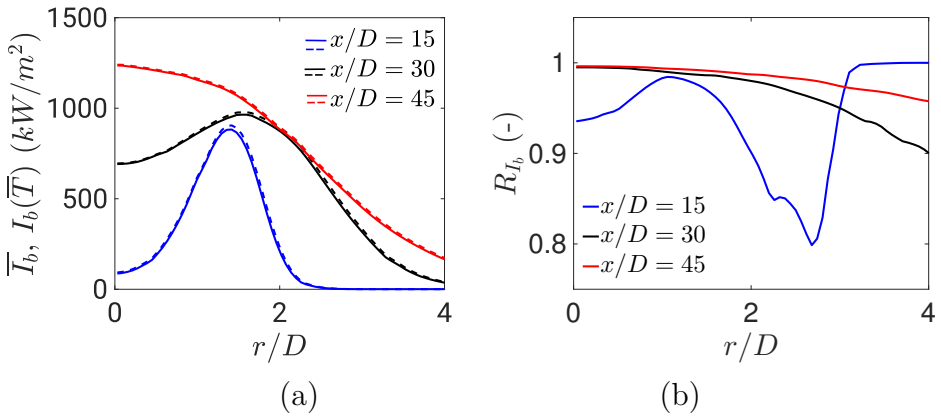

Figure 8.6: (a) Mean blackbody intensity calculated with the frozen fields of the scaled flame D for methods 1 (dashed lines) and 3 (continuous lines). (b) Quantification of the blackbody intensity self-correlation by employing Eq. (8.3).

not significant.

In order to investigate the eventual effect of the employed angular discretization for computing the radiation source term, an additional test is performed employing $n = 6$ (48 directions) for the flame D and the results are compared with the ones obtained for $n = 8$ (80 directions). The profiles of radiative source term for the frozen fields with these two different angular discretizations are shown in Fig. 8.7. For each of the employed method, a small difference can be seen between the profiles obtained for the simulations with $n = 6$ and $n = 8$. Additionally, by comparing the profiles obtained with methods 1 and 3 for each angular discretization, no difference can be visualized. This indicates that (1) the angular discretization does not have any influence on the TRI analyses and (2) the results for the simulation with $n = 8$ still do not have completely angular grid independence. However, a simulation with a finer angular grid was not performed because of computational costs.

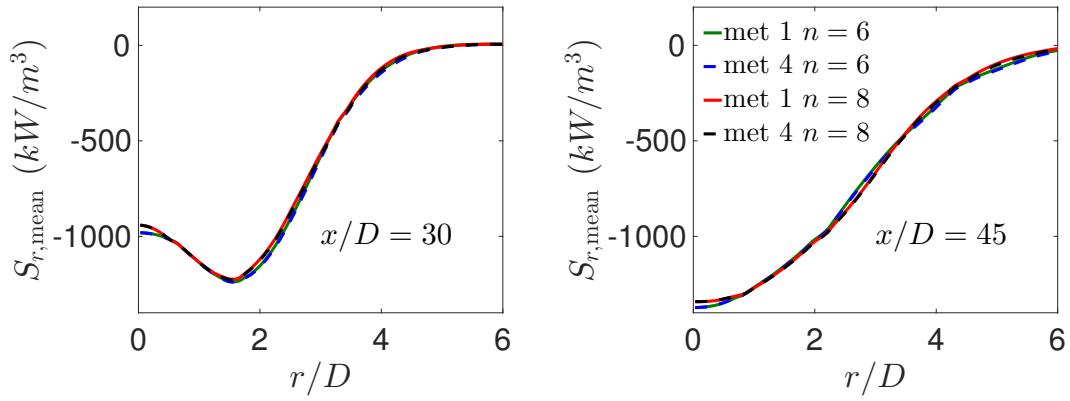

Figure 8.7: Mean radiative heat source profiles calculated with the frozen fields of the flame D for two different angular discretizations.

8.1.2 Coupled Simulations

For the coupled simulations, the difference between methods 1 and 3 is slightly larger than those of the frozen fields analyses, as it can be seen in Fig. 8.8(a), where the mean emission term is presented for three different axial positions for the scaled flame. This difference is also quantified by using Eq. (8.2) and the result is shown in Fig. 8.8(b). As for the frozen field analyses, R_{kI_b} is close to unity for significant values of the emission term. Also for the coupled case, the corresponding results for the flame D are similar to those found for the scaled flame. The supplementary results for this case can be also found in Appendix A.

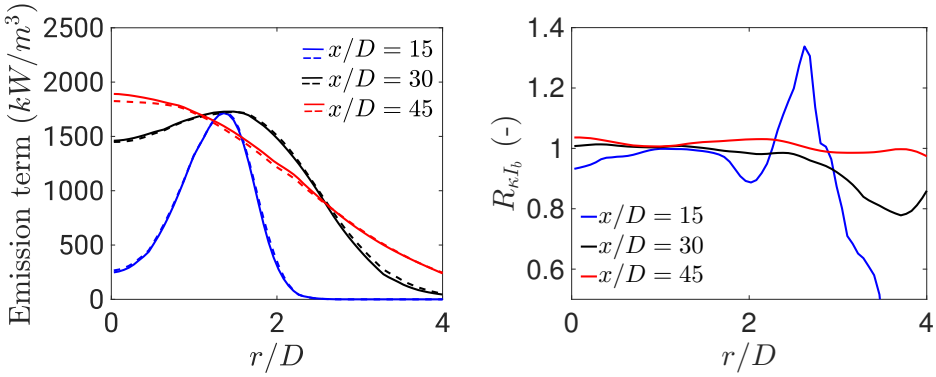

Figure 8.8: (a) Mean emission term for the coupled simulation of the scaled flame for methods 1 (dashed lines) and 3 (continuous lines). (b) Quantification of the emission term on TRI by employing Eq. (8.2).

The importance of considering thermal radiation in the computations for the scaled case is demonstrated in Fig. 8.9, where the mean temperature profiles calculated considering and ignoring thermal radiation are plotted. Additionally, the absolute difference among the employed methods is shown in the bottom row of Fig. 8.9. The difference in the profiles when considering and ignoring radiation is significant, whereas the difference between method 1 and 3 is relatively small. As already discussed for the frozen field calculations, the results for the coupled case also indicate the subgrid values are not significant for calculating the radiative source term in the LES framework. Such behavior suggests that the subgrid-scale contributions of species concentrations and the temperature fields are relatively small compared to their variances, because the radiative source term is dependent on both properties, as already seen above.

8.1.3 Summary

The Sandia flame D and the artificially scaled flame were investigated in this section by taking into consideration the radiation effects. Specially the importance of the subgrid-scales for computing the radiative source term was analyzed. Coupled and noncoupled simulations were performed. The OTFA assumption was applied to approximate the absorption TRI while the emission TRI was explicitly computed by using the ESF method.

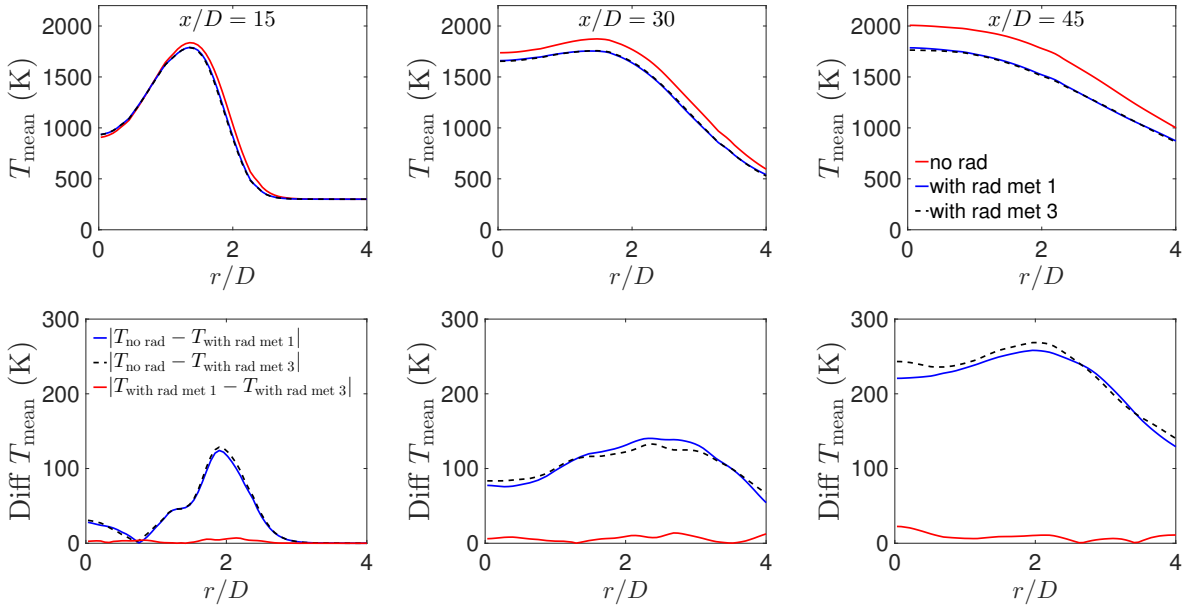

Figure 8.9: Top: mean temperature profiles for the coupled simulation of the scaled flame. Bottom: absolute difference among the employed methods.

The emission radiative heat source term was calculated by considering and ignoring the subgrid-scale contributions and the difference between the results was not significant. This indicates that the subgrid-scale contributions are not important in the context of LES for the analyzed case. These results are in agreement with the analysis for the flame D reported in Coelho [34], which used a stochastic model to generate the turbulent scalar fluctuations. However, as pointed out by Consalvi et al. [38], the influence of the subgrid-scales depends on the filter size. In their work, a ethylene-air lab-scale turbulent jet flame was analyzed and the subgrid-scale contributions were investigated for for filter sizes of l_t, $l_t/2$ and $l_t/6$, where l_t corresponds to the integral length scale. They found out that the influence of this contribution is clearly lower in the latter case than in the others.

Regarding the difference between the results obtained by either considering or ignoring the subgrid-scales for computing the radiative source term, the present results differ from the ones found in Gupta et al. [51]. In their work, the scaled flame D was investigated using a filter size that is about $l_t/2$ over a significant part of the domain. In contrast with the results presented here, the difference in the mean emission term profiles obtained by considering and omitting the subgrid-scales was significant in their work. The difference in the results is likely to be due to the larger filter size employed by Gupta et al. [51]. The method employed in [51] for approximating the emission TRI and the method used for describing the spectral behavior of the absorption coefficient are different to those used here. However, only a difference in the methodology is not sufficient to explain the discrepancy in the results.

Additionally, the radiative source term was computed by applying the mean fields of temperature and species concentrations, which is equivalent to compute this term in the context of RANS. As expected, the results obtained for this case showed a considered

discrepancy to the results computed by employing the instantaneous values, which implies the subgrid-scale contributions are relevant for RANS simulation.

8.2 Bluff-Body Stabilized Nonpremixed Flame

The configuration of this case, including the description of the numerical setup and the grid is given in Section 7.2, where this flame was studied without considering radiative heat transfer. The bluff-body surface is isothermal at 953.15 K and is considered to be gray with an emissivity of $\varepsilon_w = 0.8$.

The relevance of the subgrid-scales of TRI is investigated in this section for the bluff-body flame and for its corresponding artificially scaled flame. As done in previous section for the Sandia flame D, the scaled configuration is obtained by quadrupling the domain while the inlet velocities are divided by four to maintain the same Reynolds number as in the nonscaled case. Furthermore, only the methods 1 and 3 are considered in this section. Besides that, the analyses are done in the noncoupled manner, i. e., the data obtained in the simulation by omitting thermal radiation is used for the investigations. The radiative source term is computed in frequency of $f_{rad} = 1.25 \cdot 10^5\,\mathrm{s}^{-1}$.

The size of the employed grid was analyzed in terms of the Kolmogorov length scale (l_d), which was computed as

$$l_d = \left(\frac{\upsilon}{\epsilon}\right)^{1/4}, \tag{8.4}$$

where ϵ corresponds to the dissipation's rate. This property was estimated following Pope [111] as $\epsilon = (C_s\Delta)^2\langle S_{ij}^3\rangle$. The ratio of the grid size to the Kolmogorov length for the analyzed axial positions $x/D = 1.0$, $x/D = 1.4$ and $x/D = 1.8$ does not exceed the value of 8.

Fig. 8.10 shows the mean distribution of CO_2 and H_2O mole fraction, temperature and radiative heat source term for the bluff-body flame. The effects of the wall boundary can be clearly seen in the radiative source term field. In the region close to the surface of the bluff-body, the radiative source term is positive, which indicates gain of heat in this area. On the other hand, in flow region where the temperature, CO_2 and H_2O concentrations are high, radiative heat losses take place.

The profiles of the mean radiative source term for the scaled case are depicted in Fig. 8.11. A small difference can be noted between the profiles obtained with methods 1 e 3, where the maximum is about 3.5% for all profiles.

The mean emission term for the scaled configuration is plotted in Fig. 8.12 (a). A small discrepancy can be seen between the methods in the mean emission term profiles. Additionally, the difference between these methods is quantified by employing Eq. (8.2) and the results are presented in Fig. 8.12 (b). As it can be seen, the largest differences between the methods are found in the region where the emission term is very small. If one considered only values in which the emission term is higher than 1% of its maximum, R_{kI_b} reaches values about 0.83, 0.87 and 1.2 for axial positions $x/D = 1.0$, $x/D = 1.4$

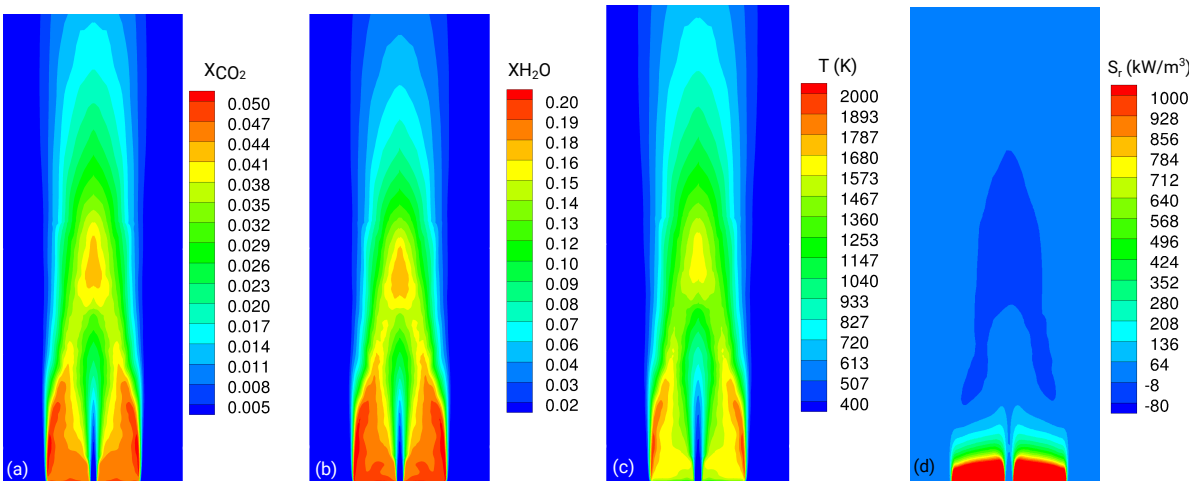

Figure 8.10: Mean distributions of (a) CO_2 mole fraction, (b) H_2O mole fraction, (c) temperature and (d) radiative heat source term for the bluff-body flame calculated with the frozen fields.

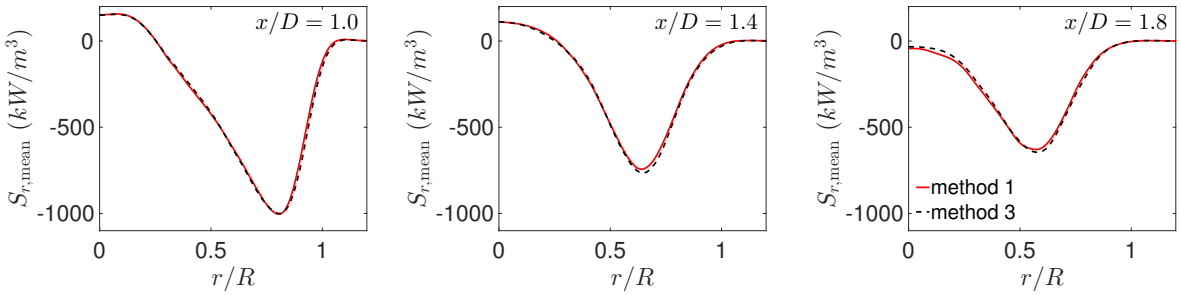

Figure 8.11: Mean radiative heat source profiles for the scaled bluff-body flame with two different TRI treatments calculated with the frozen fields.

and $x/D = 1.8$.

The mean blackbody intensity for the scaled case and its quantification calculated with Eq. (8.3) are shown in Fig. 8.13 (a) and (b), respectively. The largest differences between methods 1 and 3, are again located in regions where the blackbody intensity is small. By restricting the analysis to values in which the blackbody intensity is at least higher than 1% of the maximum in each axial position, R_{I_b} reaches values about 0.80, 0.86 and 1.12 for axial positions $x/D = 1.0$, $x/D = 1.4$ and $x/D = 1.8$.

The corresponding results for the nonscaled case are in agreement with those obtained for the scaled configuration and can be found in Appendix A.

8.2.1 Summary

The bluff-body flame and its corresponding scaled flame were studied in this section by considering radiative heat transfer. The importance of the subgrid-scale contributions for calculating the radiative heat source term was investigated. The analyses were performed

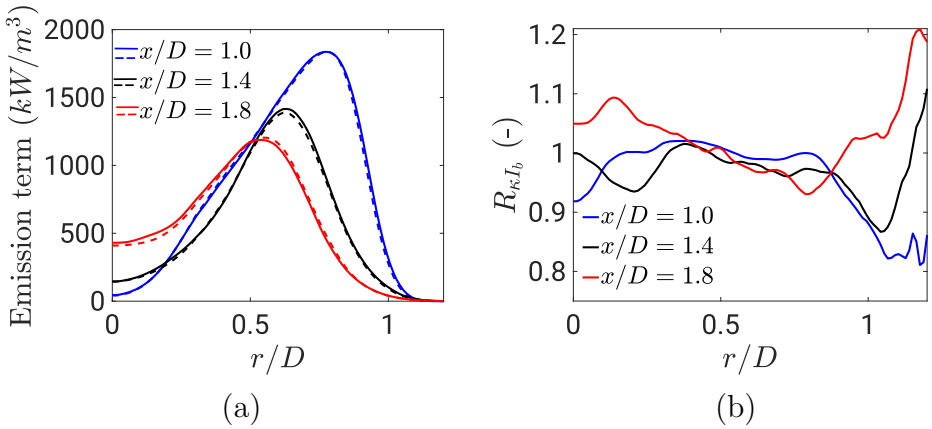

Figure 8.12: (a) Mean emission radiative term calculated with the frozen fields of the scaled bluff-body flame for methods 1 (dashed lines) and 3 (continuous lines). (b) Quantification of the emission term on TRI by employing Eq. (8.2).

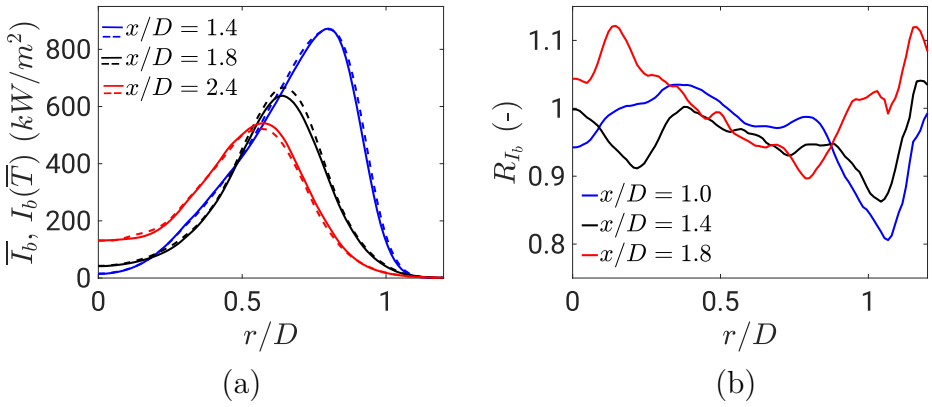

Figure 8.13: (a) Mean blackbody intensity calculated with the frozen fields of the scaled bluff-body flame for methods 1 (dashed lines) and 3 (continuous lines). (b) Quantification of the blackbody intensity self-correlation by employing Eq. (8.3).

based on the data obtained from the simulation omitting radiative heat transfer. As for the Sandia flame D, the OTFA assumption was applied for the absorption TRI whereas the emission radiative source term was explicitly calculated with the ESF method by considering and ignoring the subgrid-scale contributions.

For this case also a relative small difference could be found between the results obtained by considering or omitting the subgrid-scale contributions and this difference only reaches values higher than 10% in the regions where the radiative source term is, in absolute, very small. As already discussed for the flame D configuration, the influence of the subgrid-scale contributions is dependent on the grid size used. For this reason even if the results for this case also indicate contributions are not significant for computing the radiative source term in LES framework, this statement may not be applied for all LES studies.

Chapter 9

Summary and Outlook

This thesis dealt with the simulation of turbulent flames by taking into account thermal radiation effects. The focus of this work was the development and application of a radiation solver for computing turbulent reacting flows. In this study, the role of the *Turbulence-Radiation Interactions* (TRI) in the LES context was analyzed for two important and widely investigated configurations: the Sandia flame D and the bluff-body stabilized nonpremixed flame.

The Favre-filtered flow equations were used in this work, which included conservation of mass, momentum, species concentrations and enthalpy. In addition, the low Mach number assumption was applied. The LES models of Smagorinsky and Germano were used for modeling the turbulent viscosity. Moreover, the *Flamelet Generated Manifold* (FGM) approach was employed for the combustion modeling together with the transported joint scalar *Probability Density Function* (PDF) to account for the *Turbulence-Chemistry Interactions* (TCI). Moreover, the Monte Carlo formulation based on *Eulerian Stochastic Field* (ESF) was used to represent the subgrid PDF.

The radiation solver was implemented by considering the complete *Radiative Transfer Equation* (RTE), consisting of the emission, the absorption and the scattering terms. The finite volume method, which is a variation of the *Discrete Ordinates Method* (DOM), was applied to discretize this equation. For accounting the spectral behavior of the combustion gases involved, the *Weighted Sum of Gray Gases* (WSGG) method was used.

Successful verification studies have been conducted to check the implementations. Herein, simple 2D to relatively complex 3D cases were computed and the results were compared with analytical solutions or with results from the literature. The different implemented WSGG models were also verified against benchmark tests which consisted of (1) a box with uniform species concentration field and a given temperature distribution and (2) a cylindrical enclosure with a more realistic heterogeneous species concentration and temperature distribution.

As a prestep towards carrying out the application studies with radiative heat transfer, the employed code was validated. Since satisfactory predictions of species concentrations and temperature field are indispensable for obtaining accurate results with the radiation solver, analyses without radiation were performed as a preliminary investigation. Thus, the Sandia flame D and bluff-body flame were simulated and a acceptable agreement between the numerical and experimental results was observed thereby validating the code.

In order to take into account thermal radiation in simulations of combustion systems in the LES context, the filtered radiative source term should be computed. The contribution of the resolved scales can be explicitly calculated, whereas the terms involving the subgrid-scale contributions are unclosed and require approximations. The *Optically Thin Fluctuation Assumption* (OTFA) was applied for approximating the filtered absorption term and the ESF method was employed for representing the emission TRI. Then, the importance of considering the subgrid-scale contributions were analyzed. For this aim, simulations were performed by considering and neglecting these contributions.

The Sandia flame D, the bluff-body flame and their corresponding artificially four times scaled flames were the configurations studied in this work for analyzing the TRI. The scaled flames were additionally investigated because, they are expected to have stronger radiation effects.

For all cases, the difference between the radiative source term computed by accounting or neglecting the subgrid-scale contributions was not significant, which indicates that considering these terms is not important in context of LES for the studied cases. These results are not in agreement with the findings reported in Gupta et al. [51], who investigated the significance of the subgrid-scale contribution to compute the emission radiative source term for the scaled flame D. The difference in the results is probably due to the larger filter size employed by Gupta et al. [51]. As discussed in Consalvi et al. [38], the importance of the subgrid-scales is dependent on the LES filter size. Thus, if a wider filter is used the influence of the subgrid-scale contributions may the larger.

By comparing the profiles for the mean filtered temperature for the scaled Sandia flame D case, no significant difference ($\leq 1.5\%$) could be found between the different methods used to calculate the radiative emission. Furthermore, for this case, the radiative source term was computed with the mean fields of temperature and species concentrations. This procedure corresponds to computing the radiative source term in the RANS framework. As expected, the results for this case presented an significant difference to the remaining procedures, which demonstrate that the fluctuations are relevant for RANS.

Regarding the investigations with the bluff-body flame, performing coupled simulations is recommended for future investigations. In addition, for the Sandia flame D case, the validation of the OTFA was already extensively checked in literature. For further investigations, it is recommended to verify the validity of this approximation for the bluff-body flame as well.

Another interesting improvement of the implemented radiation code would be applying a second order spatial discretization scheme instead of the step scheme used. Since the spatial discretization of the remaining code is done with a second order scheme, it is desirable to have a complete second order code, which would enhance the accuracy and reliability of the results.

Furthermore, as the Eulerian stochastic fields is used in this work to approximate the emission TRI, the eventual effect of the number of stochastic fields employed in the ESF method should be investigated.

An additional suggestion is the extension of the code to account soot particles. As combustion systems often presents soot particles, it is interesting to have a procedure that is able to deal with formation and oxidation of soot. The interaction between TRI and soot exists and is already known in the literature, thus, investigations with the presence of soot could have an influence for the analyses of the importance of the subgrid-scale contributions in the LES framework.

Appendix A

Supplemental results

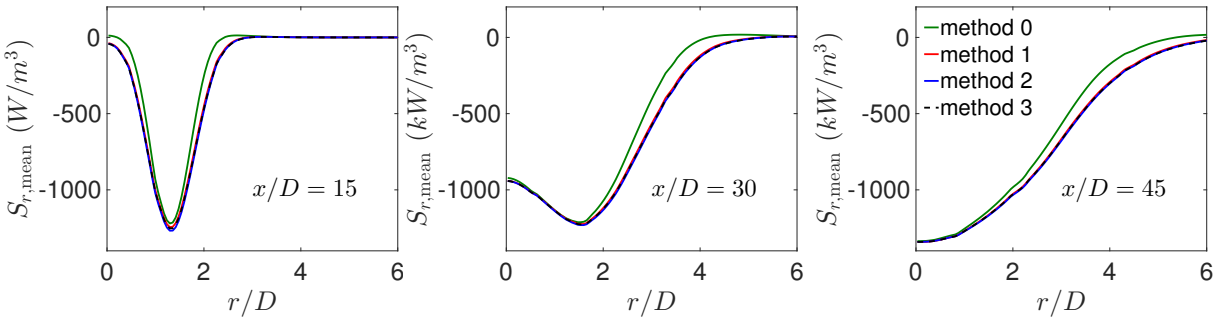

Figure A.1: Mean radiative heat source profiles for the flame D with different TRI treatments calculated with the frozen fields.

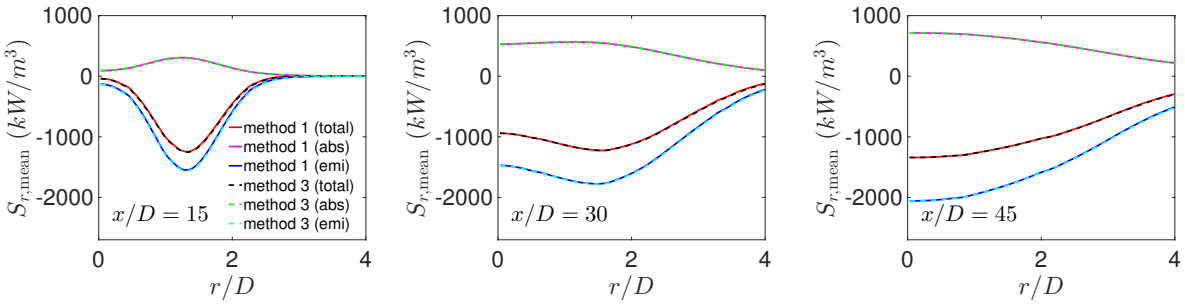

Figure A.2: Mean radiative heat source profiles for the flame D showing the absorption and emission contributions calculated with the frozen fields.

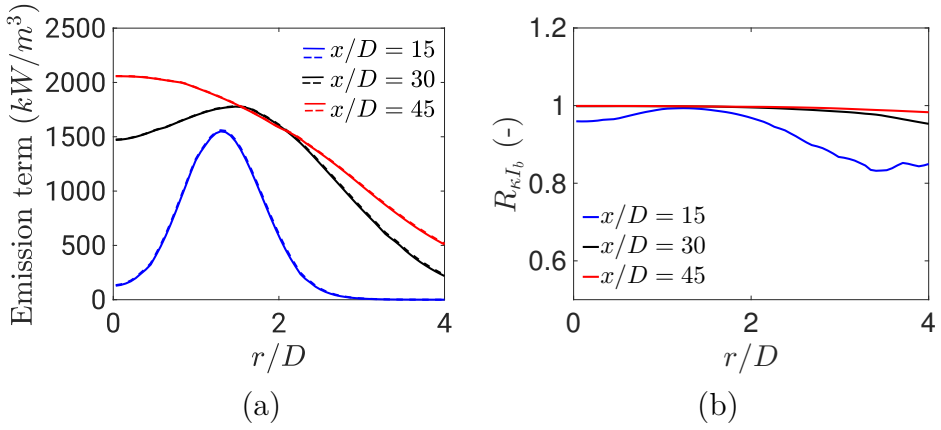

Figure A.3: Mean emission term calculated with the frozen fields of the flame D for methods 1 (dashed lines) and 3 (continuous lines). (b) Quantification of the emission term on TRI by employing Eq. (8.2) .

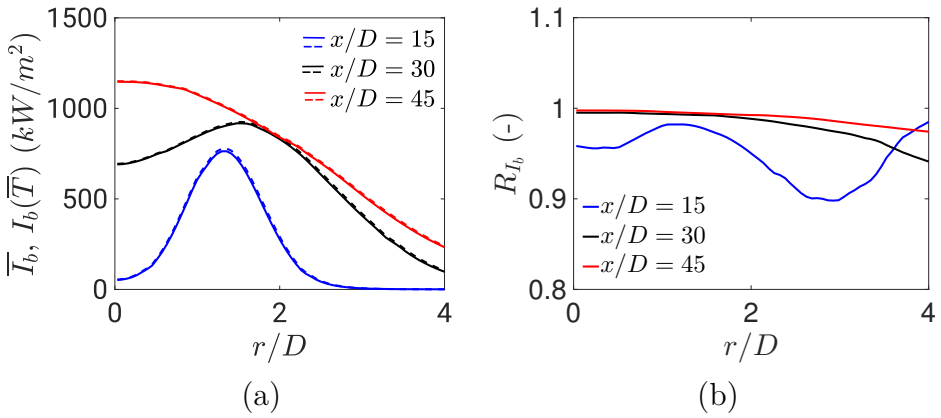

Figure A.4: Mean blackbody intensity calculated with the frozen fields of the flame D for methods 1 (dashed lines) and 3 (continuous lines). (b) Quantification of the blackbody intensity self-correlation by employing Eq. (8.3).

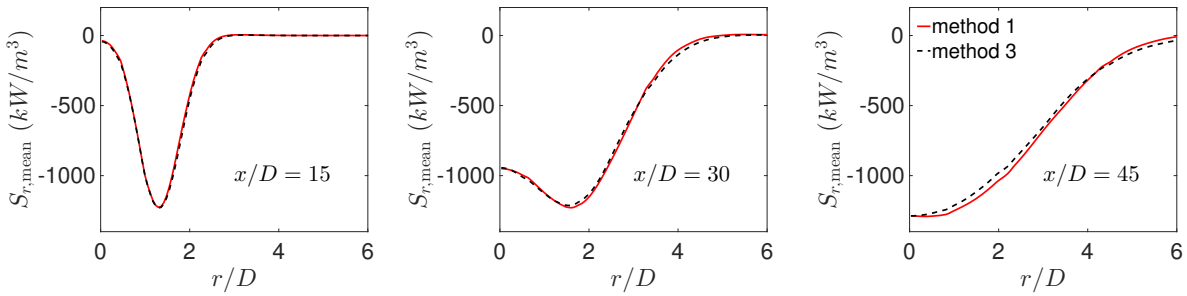

Figure A.5: Mean radiative heat source profiles for the coupled simulation of the flame D with different TRI treatments.

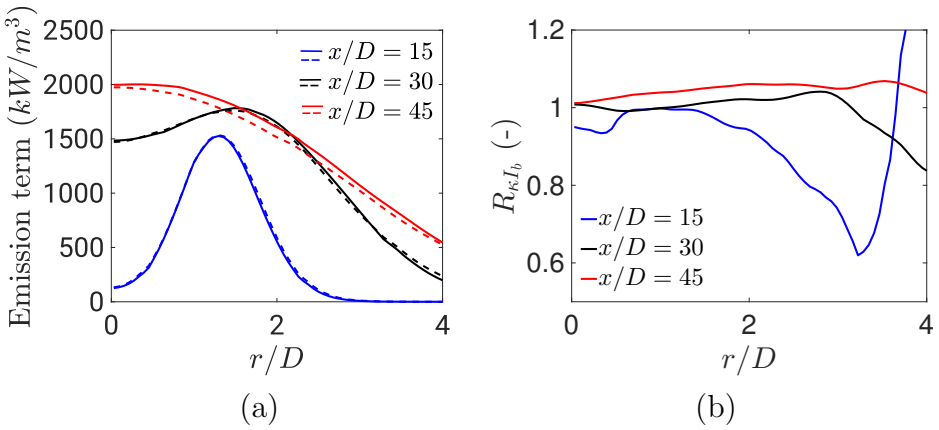

Figure A.6: Mean emission term for the coupled simulation of the flame D for methods 1 (dashed lines) and 3 (continuous lines). (b) Quantification of the emission term on TRI by employing Eq. (8.2).

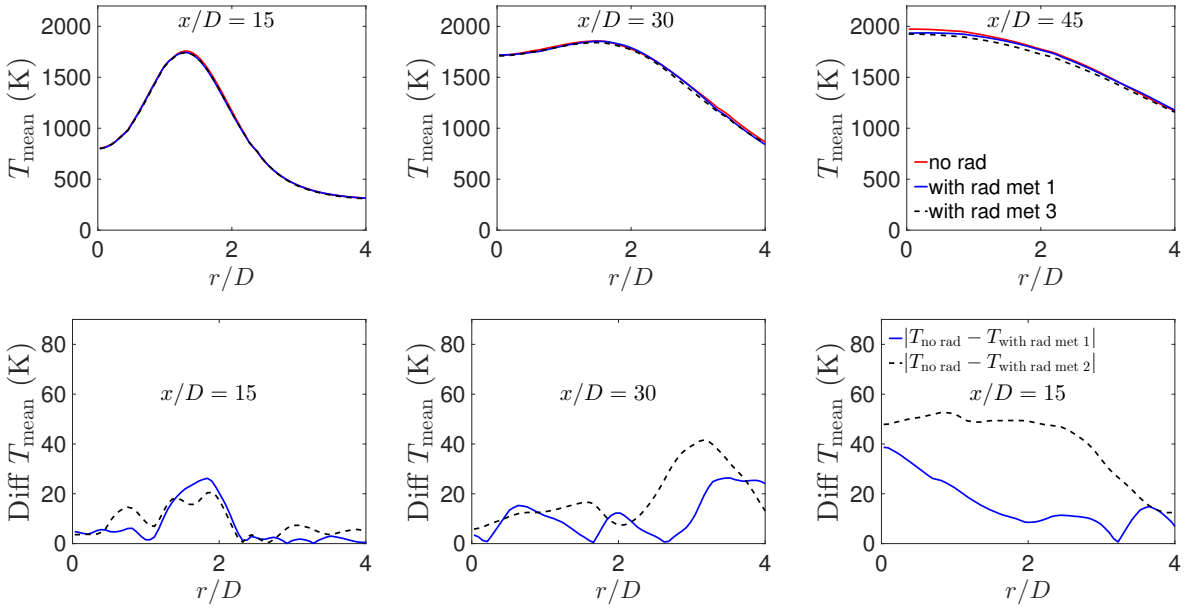

Figure A.7: Top: mean temperature profiles for the coupled simulation of the flame D. Bottom: difference among the employed methods.

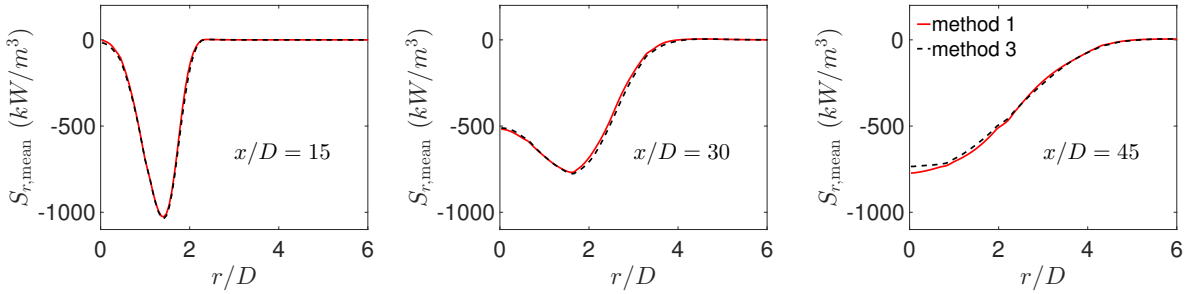

Figure A.8: Mean radiative heat source profiles for the coupled simulation of the scaled flame D with different TRI treatments.

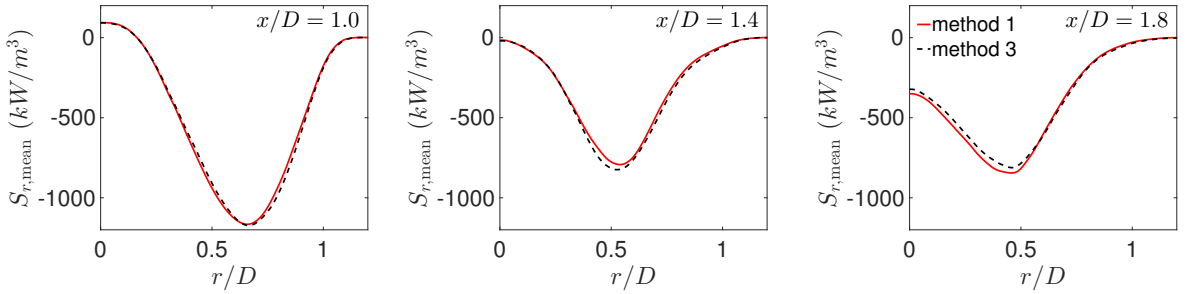

Figure A.9: Mean radiative heat source profiles for the bluff-body flame with two different TRI treatments calculated with the frozen fields.

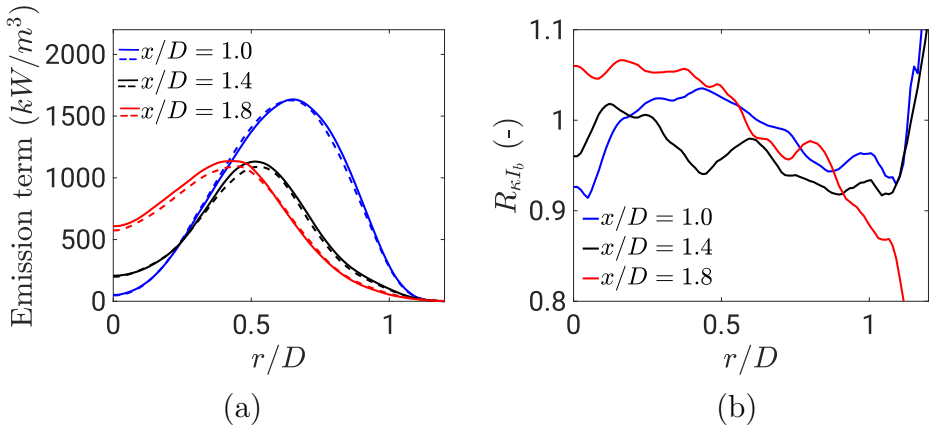

Figure A.10: Mean emission radiative term calculated with the frozen fields of the bluff-body flame for methods 1 (dashed lines) and 3 (continuous lines). (b) Quantification of the emission term on TRI by employing Eq. (8.2).

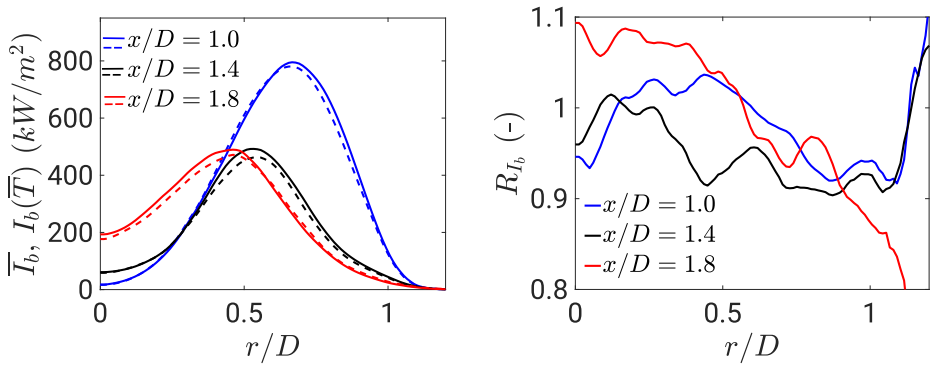

Figure A.11: Mean blackbody intensity calculated with the frozen fields of the bluff-body flame for methods 1 (dashed lines) and 3 (continuous lines). (b) Quantification of the blackbody intensity self-correlation by employing Eq. (8.3).

Bibliography

[1] Bluff-body flows and flames. http://web.aeromech.usyd.edu.au/thermofluids/bluff.php. Accessed on February 8th 2018.

[2] BP Statistical review of world energy June 2017. https://www.bp.com/content/dam/bp/en/corporate/pdf/energy-economics/statistical-review-2017/bp-statistical-review-of-world-energy-2017-full-report.pdf. Accessed on April 5th 2018.

[3] Chem1D - A one-dimensional laminar flame code. www.combustion.tue.nl/chem1d. Accessed: June 6th 2017.

[4] International workshop on measurement and computation of turbulent nonpremixed flames. http://www.sandia.gov/TNF/abstract.html. Accessed on December 11th 2015.

[5] Piloted CH_4/air flames C, D, E, and F - release 2.1. http://www.sandia.gov/TNF/DataArch/FlameD/SandiaPilotDoc21.pdf. Accessed on December 11th 2015.

[6] ANSYS Inc. *ANSYS ICEM CFD 13.0* (2010).

[7] SSI project - Lis: Library of Iterative Solvers for Linear Systems. http://www.ssisc.org/lis/, 2016. Accessed on January 5th 2016.

[8] Andersson, K., Johansson, R., and Johnsson, F. Thermal radiation in oxy-fuel flames. *International Journal of Greenhouse Gas Control 55* (2011), 558–565.

[9] Aschmoneit, K. *Numerische Beschreibung technischer Verbrennungssysteme.* Ph.D thesis, Darmstadt, 2013.

[10] Avdic, A. *Development and Application of Numerical Methods for the Simulation of Advanced Combustion Processes Within Complex Devices.* Ph.D thesis, Darmstadt, 2014.

[11] Avdic, A., Kuenne, G., di Mare, F., and Janicka, J. LES combustion modeling using eulerian stochastic flied method coupled with tabulated chemistry. *Combustion and Flame 175* (2017), 201–219.

[12] Avdic, A., Kuenne, G., and Janicka, J. Flow physics of a bluff-body swirl stabilized flamed and their prediction by means of a joint eulerian stochastic field and tabulated chemistry approach. *Flow Turbulence Combustion 97* (2016), 1185–1210.

[13] Baek, S., Kim, M. Y., and Kim, J. S. Nonorthogonal finite-volume solutions of radiative heat transfer in a three-dimensional enclosure. *Numerical Heat Transfer 34*, 4 (1998), 419–437.

[14] Barlow, R., and Frank, J. H. Effects of turbulence on species mass fraction in methane/air jet flames. *Symposium International on Combustion 21* (1998), 1087–1095.

[15] Barlow, R., Frank, J. H., Karpertis, A. N., and Chen, J. Y. Piloted methane/air jet flames: transport effects and aspects of scalar structure. *Combustion and Flame 143* (2005), 443–449.

[16] Bordbar, M., Wecel, G., and Hyppänen, T. A line by line based weighted sum of gray gases model for inhomogeneous CO_2-H_2O mixture in oxy-fired combustion. *Combustion and Flame 161* (2014), 2435–2445.

[17] Branley, N., and Jones, W. P. Large eddy simulation of a turbulent non-premixed flame. *Combustion and Flame 127* (2001), 1914–1934.

[18] Butler, T., and O'Rourke, P. A numerical method for two-dimensional unsteady reacting flows. *Symposium International on Combustion 16* (1977), 1503–1515.

[19] Centeno, F. R. *Modelagem da Radiacão Térmica em Chamas Turbulentas da Combustão de Metano em Ar*. Ph.D thesis, Porto Alegre, 2014.

[20] Centeno, F. R., Brittes, R., Franca, F. H. R., and Ezekoye, O. A. Evaluation of gas radiation heat transfer in a 2d axissymmetric geometry using the line-by-line integration and WSGG models. *Journal of Quantitative Spectroscopy & Radiative Transfer 156* (2015), 1–11.

[21] Chai, J., Lee, H. S., and Patankar, S. V. Ray effect and false scattering in the discrete ordinates method. *Numerical Heat Transfer, Part B: Fundamentals 24*, 4 (1993), 373–389.

[22] Chai, J., and Moder, J. P. Spatial-multiblock procedure for radiation heat transfer. *Numerical Heat Transfer, Part B: Fundamentals: An International Journal of Computation and Methodology 31* (1997), 277–293.

[23] Chai, J. C., Hsu, P., and Lam, Y. C. Three-dimensional transient radiative transfer modeling using finite-volume method. *Journal of Quantitative Spectroscopy & Radiative transfer 86* (2004), 299–313.

[24] Chai, J. C., Lee, H., and Patankar, S. V. Finite volume radiative heat transfer. *Journal of Thermophysics and Heat Transfer 8*, 3 (1993), 419–425.

[25] Chai, J. C., Parthasarathy, G., Lee, H., and Patankar, S. V. Finite volume radiative heat transfer procedure for irregular geometries. *Journal of Thermophysics and Heat Transfer 9*, 5 (1995), 410–415.

[26] Chen, L., Yong, S. Z., and Ghoniem, A. F. Oxy-fuel combustion of pulverized coal: Characterization, fundamentals, stabilization and CFD modeling. *Progress in Energy and Combustion Science* (2012), 156–214.

[27] Chorin, A. J. Numerical solution of the Navier-Stokes equations. *Mathematics of Computation 22* (1968), 745–762.

[28] Chui, E. H., and Raithby, G. D. Computation of radiant heat transfer on a nonorthogonal mesh using the finite-volume method. *Numerical Heat Transfer, Part B: Fundamentals 23* (1993), 269–288.

[29] Clayton, D. J., and Jones, W. P. Large eddy simulation of a methane-air diffusion flame. *Flow Turbulence Combustion 81* (2008), 497–521.

[30] Clements, A., Black, S., Szuhanszki, J., Stechly, K., Pranzitelli, A., Nimmo, W., and Pourkashanian, M. LES and RANS of air and oxy-coal combustion in a pilot-scale facility: Predictions of radiative heat transfer. *Fuel 151* (2015), 146–155.

[31] Coelho, P. J. Detailed numerical simulation of radiative transfer in nonluminous turbulent jet diffusion flame. *Combustion and Flame 136* (2004), 481–492.

[32] Coelho, P. J. A comparison of spatial discretization schemes for differential solution methods of the radiative transfer equation. *Journal of Quantitative Spectroscopy & Radiative Transfer 109* (2007), 189–200.

[33] Coelho, P. J. Numerical simulation of the interaction between turbulence and radiation in reactive flows. *Progress in Energy and Combustion Science 33* (2007), 311–383.

[34] Coelho, P. J. Approximate solutions of the filtered radiative transfer equation in large eddy simulations of turbulent reactive flows. *Combustion and Flame 156* (2009), 1099–1110.

[35] Coelho, P. J. Advances in the discrete ordinates and finite volume methods for the solution of the radiative heat transfer problems in participating media. *Journal of Quantitative Spectroscopy & Radiative Transfer 145* (2014), 121–146.

[36] Coelho, P. J., and Goncalves, J. Parallelization of the finite volume method for radiation heat transfer. *International Journal of Numerical Methods for Heat and Fluid 9* (1999), 388–404.

[37] Colin, O., Ducros, F., Veynante, D., and Poinsot, T. A thickened flame model for large eddy simulations of turbulent premixed combustion. *Physics of Fluids 12* (2000), 1843–1863.

[38] Consalvi, J. L., Nmira, F., and Kong, W. On the modeling of the filtered radiative transfer equation in large eddy simulations of lab-scale sooting turbulent diffusion flames. *Journal of Quantitative Spectroscopy & Radiative Transfer* (2018), In Press.

[39] Courant, R., Friedrichs, K., and Lewy, H. Über die partiellen differenzengleichungen der mathematischen physik. *Mathematische Annalen 100* (1928), 32–74.

[40] Denison, M. K., and Webb, B. W. A spectral line based weighted-sum-of-gray-gases model for arbitrary RTE solvers. *Journal of Heat transfer 115*, 4 (1993), 1004–1012.

[41] Dorigon, L. J., Duciak, G., Brittes, R., Cassol, F., Galarca, M., and Franca, F. H. R. Wsgg correlations based on HITEMP 2010 for computation of thermal radiation in non-isothermal, non-homogeneous H_2O/CO_2 mixtures. *International Journal of Heat and Mass Transfer 63* (2013), 863–873.

[42] Dos Santos, R. G., Ducruix, S., Gicquel, O., and Veynate, D. A study of three-dimensional LES of turbulent combustion with radiative heat transfer. *Journal of the Brazilian Society of Mechanical Sciences and Engineering* (2015), 1–16.

[43] El-Mahallawy, F., and Habik, S. E. *Fundamentals and Technology of Combustion.* Elsevier, 2002.

[44] Favre, A. Statistical equations of turbulent gases. *Problems of Hydrodynamics and Continuum Mechanics* (1969), 231–266.

[45] Ferziger, J. H., and Peric, M. *Computational Methods for Fluid Dynamics, 3rd ed.* Springer, 2002.

[46] Forman, W., and Williams, F. *Combustion Theory*, second edition ed. Addision-Wesley, Redwood City, USA, 1985.

[47] Gao, F., and O'Brien, E. A large eddy simulation scheme for turbulent reacting flows. *Physics of Fluids 5* (1993), 1282–1284.

[48] Germano, M. Turbulent fluctuations coupled with the radiation field. *2nd AIAA/I-ASME Thermophysics and Heat Transfer Conference* (1978).

[49] Germano, M., Piomelli, U., Moin, P., and Cabot, W. H. A dynamic subgrid-scale eddy viscosity model. *Physics of Fluids 3*, 7 (1991), 1760–1765.

[50] Gupta, A. *Large-Eddy Simulation of Turbulent Flames with Radiation Heat Transfer.* Ph.D thesis, The Pennsylvania State University, 2011.

[51] Gupta, A., Haworth, D. C., and Modest, M. F. Turbulence-radiation interactions in large-eddy simulations of luminous and nonluminous non premixed flames. *Proceedings of the Combustion Institute 34* (2013), 1281–1288.

[52] Habermehl, M., Hess, J., Massmeyer, A., Zabrodiec, D., and and. R. Kneer, O. H. Comparison of flame stability under air and oxy-fuel conditions for an aerodynamically stabilized pulverized coal swirl flame. *Journal of Energy Resources Technology 138* (2016), 1–8.

[53] Hahn, F. *Zur Vorhersage technischer Verbrennungssysteme im Hinblick auf fluessige Brennstoffe.* PhD thesis, TU Darmstadt, 2008.

[54] Haworth, D. C., and Pope, S. B. *Transported Probability Density Function Methods for Reynolds-Averaged and Large-Eddy Simulations.* Turbulent Combustion Modeling, 2000.

[55] Haworth, D. C., and Pope, S. B. *Transported Probability Density Function Methods for Reynolds-Averaged and Large-Eddy Simulations.* Turbulent Combustion Modeling, 2000.

[56] Hirschfelder, J., Curtiss, C., and Bird, R. *Molecular Theory of Gases and Liquids*. Structure of matter series. John Wiley & Sons, New York, 1967.

[57] Hottel, H. C., and Sarafim, A. F. *Radiaive Transfer*. McGraw-Hill Book Company, New York, 1967.

[58] Howell, J. R., Siegel, R., and Mengüç, M. P. *Thermal Radiation Heat Transfer. 5th edition.* Taylor and Francis, 2011.

[59] Jesch, D. *Large Eddy Simulation of Turbulent Combustion: a Novel Multivariate Probability Density Function Approach*. Ph.D thesis, Darmstadt, 2016.

[60] Johansson, R., Andersson, K., Leckner, B., and Thunman, H. Models for gaseous radiative heat transfer applied to oxy-fuel conditions in boilers. *International Journal of Heat and Mass Transfer 53* (2010), 220–230.

[61] Johansson, R., Leckner, B., Andersson, K., and Johnsson, F. Account for variations in the H_2O to CO_2 molar ratio when modeling gaseous radiative heat transfer with the weighted-sum-of-grey-gases model. *Combustion and Flame 158* (2011), 893–901.

[62] Jones, W. P., and Navarro-Martinez, S. Large eddy simulation of auto-ignition with a subgrid probability density function. *Combustion and Flame 150* (2007), 170–187.

[63] Jones, W. P., and Navarro-Martinez, S. Numerical study of n-heptane auto-ignition using LES-PDF methods. *Flow, Turbulence and Combustion 83*, 3 (2009), 407–423.

[64] Joseph, D., Coelho, P. J., Cuenot, B., and El Hafi, M. Application of the discrete ordinates method to grey media in complex geometries using unstructured meshes. *Proceedings of Eurotherm73 on Computational Thermal Radiation in Participating Media* (2003).

[65] Joseph, D., Hafi, M. E., Fournier, R., and Cuenot, B. Comparison of three spatial differencing schemes in discrete ordinates method using three-dimensional unstructured meshes. *International Journal of Thermal Sciences 44* (2005), 1233–1242.

[66] Kabashnikov, V. P., and Myasnikova, G. I. Thermal radiation in turbulent flows—temperature and concentration fluctuations. *Heat Transfer-Soviet Research 17*, 6 (1985), 116–125.

[67] Keating, E. L. *Applied Combustion, 2nd ed.* Taylor & Francis Group, 2007.

[68] Kempf, A. *Large Eddy Simulation of Non Premixed Turbulent Flames*. Ph.D thesis, Darmstadt, 2004.

[69] Kempf, A., Lindstedt, R., and Janicka, J. Large-eddy simulation of a bluff-body stabilized non-premixed flame. *Combustion and Flame 144* (2006), 170–189.

[70] Kerstein, A., Ashurst, W., and Williams, F. Field equation for interface propagation in an unsteady homogeneous flow field. *Physical Review A 37* (1988), 2728–2731.

[71] Ketelheun, A. *Development of Tabulated Chemistry Methods for the Accurate Simulation of Turbulent Combustion Systems*. Ph.D thesis, Darmstadt, 2014.

[72] Kim, S. H., and Huh, K. Y. A new angular discretization scheme of the finite volume method for 3-D radiative heat transfer in absorbing, emitting and anisotropically scattering media. *International Journal of Heat and Mass Transfer 43* (2000), 1233–1242.

[73] Klein, M., Sadiki, A., and Janicka, J. A digital filter based generation of inflow data for spatially developing direct numerical or large eddy simulations. *Journal of Computational Physics 186* (2003), 652–665.

[74] Kloeden, P., and Platen, E. *Numerical Solution of Stochastic Differential Equations.* Springer, 1992.

[75] Kuan, T., and Lindstedt, R. Transported probability density function modeling of a bluff-body stabilized turbulent flame. *Proceedings of the Combustion Institute 30* (2005), 767–774.

[76] Kuehne, J., Ketelheun, A., and Janicka, J. Analysis of sub-grid PDF of a progress variable approach using a hybrid LES/TPDF method. *Proceedings of the Combustion Institute 33* (2011), 1411–1418.

[77] Kuenne, G., Euler, M., Ketelheun, A., Dreizler, A. A. A., and Janicka., J. A numerical study of the flame stabilization mechanism being determined by chemical reaction rates submitted to heat transfer processes. *Zeitschrift für Physikalische Chemie 229, Nr. 5* (2014), 643–662.

[78] Künne, G. *Large Eddy Simulation of Premixed Combustion Using Artificial Flame Thickening Coupled With Tabulated Chemistry.* Ph.D thesis, Darmstadt, 2012.

[79] Künne, G., Ketelheun, A., and Janicka, J. Assessment of isothermal and reacting LES when applied to a new premixed stratified burner. *in: Proceedings of the European Combustion Meeting* (2011), 1–6.

[80] Künne, G., Ketelheun, A., and Janicka, J. LES modeling of premixed combustion using a thickened flame approach coupled with FGM tabulated chemistry. *Combustion and Flame 158* (2011), 1750–1767.

[81] Künne, G., Seffrin, F., Fuest, F., Ketelheun, A., Geyer, D., Janicka, J., and Dreizler, A. Experimental and numerical analysis of a lean premixed stratified burner using 1D Raman/Rayleigh scattering and large eddy simulation. *Combustion and Flame 159* (2012), 2669–2689.

[82] Lehnhaeuser, T. *Eine effiziente numerische Methode zur Gestalsoptimierung von Stroemungsgebieten.* Ph.D thesis, Darmstadt, 2004.

[83] Lehnhäuser, T., and Schäfer, M. Improved linear interpolation practice for finite volume schemes on complex grids. *Journal for Numerical Methods in Fluids 38* (2002), 625–645.

[84] Leister, H. J. *Numerische simulation dreidimensionaler, zeitabhaenginger Stroemungen unter dem Einfluss von Auftriebs- und Traegheitskraeften.* Ph.D thesis, Erlangen, 1994.

[85] Lesieur, M. *Turbulence in Fluids, 4th ed.* Springer, 2008.

[86] Li, G., and Modest, M. F. Importance of turbulence-radiation interactions in turbulent diffusion jet flames. *Journal of Heat Transfer 125* (2003), 831–838.

[87] Lilly, D. K. A proposed modification of the Germano subgrid-scale closure method. *Physics of Fluids A: Fluid Dynamics 4*, 3 (1992), 633–635.

[88] Lui, F. Numerical solutions of three-dimensional non-grey gas radiative transfer using the statistical narrow-band model. *Transactions of the ASME 121* (1999), 201–203.

[89] Malkmus, W. Random Lorentz band model with exponential-tailed S-1 line-intensity distribution function. *Journal of the Optical Society of America 57*, 3 (1967), 323–329.

[90] Mazumder, S., and Modest, M. F. A probability density function approach to modeling turbulence-radiation interactions in nonluminous flames. *International Journal of Heat and Mass Transfer 42* (1999), 971–991.

[91] Mazumder, S., and Modest, M. F. Application of the full spectrum correlated-k distribution approach to modeling non-gray radiation in combustion gases. *Combustion and Flame 129*, 4 (2002), 416–438.

[92] Miranda, F., and Janicka, J. Solver evaluation for computations the radiative transfer equation using finite volume method and block strutured meshes. *RAD16 - 8th International Symposium in Radiative Transfer Poster Presentation* (2016).

[93] Miranda, F. C., Coelho, P. J., and Janicka, J. Study of turbulence-radiation interactions in large eddy simulations of Sandia flame D. *Eurotherm Seminar 110 - Computational Thermal Radiation in Participanting Media - VI* (April 11-13, 2018), Caiscais, Portugal.

[94] Miranda, F. C., di Mare, F., Sadiki, A., and Janicka, J. Performance analysis of different solvers for computing the radiative transfer equation in complex geometries using finite volume method and block structured grids. *Computational Thermal Sciences 9*, 3 (2017), 269–282.

[95] Modest, M. *Radiative Heat Transfer, 3rd ed.* Academic Press, 2013.

[96] Modest, M., and Haworth, D. *Radiative Heat Transfer in Turbulent Combustion Systems: Theory and Applications, 1st ed.* Springer Briefs in Applied Sciences and Technology, 2016.

[97] Modest, M. F. The weighted-sum-of-gray-gases model for arbitrary solution methods in radiative transfer. *Journal of Heat Transfer 113*, 3 (1991), 650–656.

[98] Murthy, J. Y., and Mathur, S. R. Finite volume method for radiative heat transfer using unstructured meshes. *Journal of Thermophysics and Heat Transfer 12*, 3 (1998), 313–321.

[99] Mustata, R., Valino, L., Jimenez, C., Jones, W. P., and Bondi, S. A probability density function Eulerian Monte Carlo field method for large eddy simulations: Application to a turbulent piloted methane/air diffusion flame (Sandia D). *Combustion and Flame 145* (2006), 88–104.

[100] Nishida, A. Experience in developing an open source scalable software infrastructure in japan. *In: Computational Science and Its Applications - ICCSA 2010* (2010).

[101] Olbricht, C. *Numerische Berechnung technischer Verbrennungssysteme*. PhD thesis, TU Darmstadt, 2008.

[102] O'Rourke, P., and Bracco, F. Two scaling transformations for the numerical computation of multidimensional unsteady laminar flames. *Journal of Computational Physics 33*, 2 (1979), 185 – 203.

[103] Pal, G., Gupta, A., Modest, M. F., and Haworth, D. C. Comparison of accuracy and computational expense of radiation models in simulation of non-premixed turbulent jet flames. *Combustion and Flame 162* (2015), 2487–2495.

[104] Peric, M. *Finite Volume Method for the Prediction of Three-Dimensional Fluid Flow in Complex Ducts*. Ph.D thesis, Imperial College London, 1985.

[105] Peters, N. *Turbulent Combustion*. Cambridge University Press, 1980.

[106] Peters, N. Laminar diffusion flamelets in non-premixed turbulent combustion. *Progress in Energy and Combustion Science 3* (1984), 319–339.

[107] Peters, N. Laminar flamelet concepts in turbulent combustion. *Twenty-First Symposium (International) on Combustion 21*, 1 (1986), 1231–1250.

[108] Pitsch, H. Large-eddy simulation of a turbulent combustion. *Annual Review of Fluid Mechanics 38* (2006), 453–482.

[109] Poinsot, T., and Veynante, D. *Theoretical and Numerical Combustion, 3rd ed*. 2005.

[110] Pope, S. B. A Monte Carlo method for the PDF equations of turbulent reacting flow. *Combustion Science and Technology 25* (1981), 159–174.

[111] Pope, S. B. *Turbulent Flows*. Cambridge University Press, 2000.

[112] Porter, R., Lui, F., Pourkashanian, M., Williams, A., and Smith, D. Evaluation of solution methods for radiative heat transfer in gaseous oxy-fuel combustion environments. *Journal of Quantitative Spectroscopy & Radiative Transfer 111* (2010), 2084–2094.

[113] Raithby, G. D., and Chui, E. H. A finite-volume method for predicting a radiant heat transfer in enclosures with participating media. *Journal of Heat Transfer 112* (1990), 415–423.

[114] Rhie, C. M., and Chow, W. L. Numerical study of the turbulent flow past an airfoil with trailing edge separation. *AIAA Journal 21* (1983), 1525–1532.

[115] Rhodes, R. A probability distribution function for turbulent flows. *Turbulent mixing in nonreactive and reactive flows, Plenum Press, Cambridge UK* (1975), 235–241.

[116] Richter, K., Friedrich, R., and Schmitt, L. Large eddy simulation of turbulent wall boundary layers with pressure gradient. *Symposium on Turbulent Shear Flows, 6th, Toulouse* (1987).

[117] Rothman, L. S., Gamache, R. R., Tipping, R. H., Rinsland, C. P., Smith, M. A. H., Benner, D. C., Devi, V. M., Flaud, J.-M., Camy-Peyret, C., Perrin, A., Goldman, A., Massie, S. T., Brown, L. R., and Toth, R. A. The HITRAN molecular database: Editions of 1991 and 1992. *Journal of Quantitative Spectroscopy & Radiative Transfer 48*, 5/6 (1992), 469–507.

[118] Rothman, L. S., Goldman, C. P. R. A., Massie, S. T., Edwards, D. P., Flaud, J.-M., Perrin, A., Camy-Peyret, C., Dana, V., Mandin, J.-Y., Schroeder, J., McCann, A., Gamache, R. R., Wattson, R. B., Yoshino, K., Chance, K. V., Jucks, K. W., Brown, L. R., Nemtchinov, V., and Varanasi, P. The HITRAN molecular spectroscopic database and HAWKS (HITRAN atmospheric workstation): 1996 edition. *Journal of Quantitative Spectroscopy & Radiative Transfer 60* (1998), 665–710.

[119] Rothman, L. S., Gordon, I. E., Barber, R. J., Dothe, H., Gamache, R. R., Goldman, A., Perevalov, V. I., and Tennysonb, S. A. T. J. HITEMP, the high-temperature molecular spectroscopic database. *Journal of Quantitative Spectroscopy and Radiative Transfer 111*, 15 (2010), 2139–2150.

[120] Rothman, L. S., Wattson, R. B., Gamache, R. R., Schroeder, J., and McCann, A. HITRAN, HAWKS and HITEMP high temperature database. *Proceedings of SPIE 2471* (1995), 105–111.

[121] Schlichting, H., Gersten, K., Krause, E., and Oertel, H. J. *Grenzschicht-Theorie*, 10. überarb. aufl. 2006 ed. Springer Science & Business Media, Berlin Heidelberg, 2006.

[122] Schneider, C., Dreizler, A., Janicka, J., and Hassel, E. Flow field measurements of stable and locally extinguishing hydrocarbon-fuelled jet flames. *Combustion and Flame 135* (2003), 185–190.

[123] Selcuk, N. Exact solutions for radiative heat transfer in box-shaped furnaces. *Transactions of the ASME 107* (1985), 648–655.

[124] Silva, C. V. *Simulacão Numérica da Combustão Turbulenta de gás Natural em Câmara Cilíndrica.* Ph.D thesis, Porto Alegre, 2005.

[125] Smagorinsky, J. General circulation experiments with the primitive equations, 1. the basic experiment, monthly weather review. 99–164.

[126] Smith, G. P., Golden, D. M., Frenklach, M., Moriarty, N. W., Eiteneer, B., Goldenberg, M., Bowman, C. T., Hanson, R. K., Song, S., Gardiner, Jr., W. C., Lissianski, V. V., and Qin, Z. GRI-Mech 3.0, 1999.

[127] Snegirev, A. Y. Statistical modeling of thermal radiation transfer in buoyant turbulent diffusion flames. *Combustion and Flame 136* (2004), 51–71.

[128] Solovjov, V. P., and BW, B. W. W. A local-spectrum correlated model for radiative transfer in non-uniform gas media. *Journal of Quantitative Spectroscopy and Radiative Transfer 73* (2002), 361–373.

[129] Song, T. H., and Viskanta, R. Interaction of radiation with turbulence: Application to a combustion system. *Journal of Thermophysics and Heat Transfer 1* (1987), 56–62.

[130] Sparrow, E. M., and Cess, R. D. *Radiation Heat Transfer. 5th edition.* Hemisphere, 1978.

[131] Stephan, P., Schaber, K., Stephan, K., and Mayinger, F. *Thermodynamik: Grundlagen und technische Anwendungen Band 1: Einstoffsysteme.* Springer-Verlag Berlin Heidelberg, 2013.

[132] Stone, H. L. Iterative solution of implicit approximations of multidimensional partial differential equations. *SIAM Journal of Numerical Analysis 5* (1968), 530–558.

[133] Talukdar, P., Steven, M., Issendorff, F. V., and Trimis, D. Finite volume method in 3-D curvilinear coordinates with multiblocking procedure for radiative transport problems. *International Journal of Heat and Mass Transfer 48* (2005), 4657–4666.

[134] Tashkun, S. A., Perevalov, V. I., Teffo, J.-L., Bykov, A. D., and Lavrentieva, N. N. The high-temperature carbon dioxide spectroscopic databank. *Journal of Quantitative Spectroscopy & Radiative Transfer 82*, 1–4 (2003), 165–196.

[135] Valino, L. A field Monte Carlo formulation for calculating the probability density function of a single scalar in a turbulent flow. *Flow, Turbulence and Combustion 60*, 2 (1998), 157–172.

[136] van Leer, B. Towards the ultimate conservation difference scheme. II. monotonicity and conservation combined in a second-order scheme. *Journal of Computational Physics 14* (1974), 361–370.

[137] van Oijen, J., and de Goey, L. Modelling of premixed laminar flames using FGM. *Combustion Science and Technology 161* (2000), 113–137.

[138] Varga, R. S., Niethammer, W., and Cai, D. Y. P-cyclic matrices and the symmetric successive overrelation method. *linear Algebra and its Applications 58* (1984), 425–439.

[139] Viskanta, R., and Menguc, M. P. Radiation heat transfer in combustion systems. *Progress in Energy and Combustion Science 13* (1987), 97–160.

[140] Wang, A., and Modest, M. F. Photon Monte Carlo simulation of radiative transfer in gaseous media represented by discrete particle fields. *Journal of Heat Transfer 128* (2006), 1041–1049.

[141] Wang, A., Modest, M. F., Haworth, D. C., and Wang, L. Monte Carlo simulation of radiative heat transfer and turbulence interactions in methane/air jet flames. *Journal of Quantitative Spectroscopy & Radiative Transfer 109* (2008), 269–279.

[142] White, F. M. *Fluid Mechanics, 4th ed.* McGraw-Hill, 1998.

[143] Williams, F. Recent advances in theoretical descriptions of turbulent diffusion flames. *Turbulent Mixing in Nonreactive and Reactive Flows, Plentum Press* (1975).

[144] Williamson, J. H. Low-storage runge-kutta schemes. *Journal of Computational Physics 35* (1980), 48–56.

[145] Wu, Y., Haworth, D. C., Modest, M. F., and Cuenot, B. Direct numerical simulation of turbulence/radiation interaction in premixed combustion systems. *Proceedings of the Combustion Institute 30* (2005), 639–64.

[146] Zhang, J., Ito, T., Ito, S., Riechelmann, D., and Fujimori, T. Numerical investigation of oxy-coal combustion in a large-scale furnace: Non-gray effect of gas and role of particle radiation. *Fuel 139* (2015), 97–93.

[147] Zhang, J., Kouatchou, J., and Othman, M. On cyclic reduction and finite difference schemes. *Journal of Computational and Applied Mathematics 145* (2002), 213–222.

[148] Zheng, Y., Barlow, R. S., and Gore, J. P. Spectral radiation properties of partially premixed turbulent flames. *Journal of Heat Transfer 125* (2003), 1065–1073.

[149] Zhou, G., Davidson, L., and Olsson, E. Transonic inviscid/turbulent airfoil flow simulation using a pressure based method with high order schemes. *Proceedings of Fourteenth International Conference on Numerical Methods in Fluid Dynamics, Springer, Berlin, Heidelberg* (1995), 372–378.